Photoinduced transfer processes in complex carrier systems for photodynamic therapy

DISSERTATION

zur Erlangung des akademischen Grades
doctor rerum naturalium
(Dr. rer. nat.)
im Fach Physik

eingereicht an der
Mathematisch-Naturwissenschaftliche Fakultät I
Humboldt-Universität zu Berlin

von

Dipl.-Phys. Martin Regehly
geboren am 02.04.1978 in Berlin

Präsident der Humboldt-Universität:
Prof. Dr. Christoph Markschies

Dekan der Mathematisch-Naturwissenschaftlichen Fakultät I:
Prof. Dr. Christian Limberg

Gutachter: 1. Professorin Beate Röder (HU-Berlin, Deutschland)

2. Professor Jürgen Raabe (HU-Berlin, Deutschland)

3. Professor Hiroshi Maeda (Sojo-Universität, Japan)

Datum der Promotion: 16. 07. 2008

Dedication

For my family and my fiancée, who offered me love and support throughout the course of this thesis.

Contents

Abbreviations

$^1O_2$	Singlet oxygen
$^3O_2$	Ground state molecular oxygen
CMC	Critical micelle concentration
DMF	Dimethylformamide
DPBF	1, 3-diphenylisobenzofuran
EPR	Enhanced penetration and retention
ET	Electron transfer
EtOH	Ethanol
FRET	Förster resonance energy transfer
Ge	Germanium
Hp	Hematoporphyrin
HPMA	N-hydroxy-propyl methacrylate
ISC	Intersystem crossing
MCS	Modular carrier system
MW	Molecular weight
NCS	Neocarzinostatin
NIR	Near infrared
O_2^-	Superoxide ion
OD	Optical density
PDT	Photodynamic therapy
PEG	Polyethylene glycol
PhCN	Benzonitrile
PIC	Photosensitizer immunoconjugate
PS	Photosensitizer
RB	Rose Bengal
ROS	Reactive oxygen species
S_1	First excited singlet state
SCE	Saturated calomel electrode
SMA	Styrene maleic acid
T_1	First excited triplet state
TAS	Transient absorption spectroscopy
TCSPC	Time-correlated single photon counting

TP	Two-photon
TPA	Two-photon absorption
ZnOEP	Zinc octaethylporphrin
ZnP	Zinc porphyrin
ZnPP	Zinc protoporphyrin
Φ_F	Fluorescence quantum yield
Φ_{ISC}	Intersystem crossing quantum yield
Φ_Δ	Singlet oxygen quantum yield
τ_F	Fluorescence lifetime
τ_T	Triplet state lifetime
τ_Δ	Singlet oxygen lifetime

1 Introduction

Cancer is one of the leading causes of death in western countries, and its incidence has been rising. [Fer07, Jem07] Established cancer treatments, such as cytostatic chemotherapy, radiation, and surgery are often inadequate for full recovery and they also have serious side effects.
Photodynamic therapy (PDT) is an alternative non-invasive modality to treat cancers of the head and neck, brain, lung, pancreas, intraperitoneal cavity, breast, prostate and skin. Today PDT is not only approved for tumor therapy, it is used to treat several other diseases like age-related macular degeneration, psoriasis and scleroderma as well. [Dol03, Hol03, Ber05]

PDT combines the use of photosensitizing dye molecules (photosensitizer), light and oxygen to selectively destroy abnormal tissue. The photosensitizer, after activation with light of appropriate wavelength, generates reactive oxygen species, mainly singlet oxygen. This cyctotoxic effector destroys the tissue only in the local environment of the photosensitizer leading to a defined destruction of the area where light has been applied. [Röd00a, Röd04]

In order to achieve effective treatments with low associated side effects, the photosensitizer should selectively accumulate in the tumor tissue following administration to the patient. Up to now, photosensitizers approved for clinical use display only a limited tumor specifity. [Vro99, Don04] For this reason molecular delivery systems utilizing different targeting strategies have been taken into consideration. [Mae02, Yok05, Dun06] Among them are liposomes [Jia98, Der04, Sch05], protein nanoparticles [Pol02, Taw06], dendrimers [Bat01, Nis03, Pau03], polymeric micelles [Zha03a, Rob06, Nos04] and photosensitizer-immunoconjugates employing antibodies as targeting units.[Car01, Sav03, Ran07b]

Most of these targeting systems cause selective accumulation in tumor cells. In contrast, the photodynamic activity of the photosensitizer-carrier complexes was significantly affected compared to the photosensitizer alone. [Ham03, Sav03, Ran05b] It has been found that after photoexcitation complex energy transfer mechanisms and nonradiative deactivation processes take place among photosensitizers attached to or incorporated in such carrier systems. [Erm05, Hac05, Hel05] These processes influence the potential of photosensitizer-carrier conjugates to generate cyctotoxic oxygen species. As a consequence, the macromolecules may be inefficient for the use in PDT.

The present work investigates three promising photosensitizer-carrier systems regarding to the photophysical processes after light excitation and their implications for the applicability of the complexes for PDT. It is expected that the carrier system itself and the molecular architecture of the conjugates have an important influence on the type and efficiency of intramolecular deactivation or transfer processes. Revealing the underlying structure-property relationships may improve the development of novel PDT agents.

Among the macromolecules studied, the focus is set on the examination of hexapyropheophorbide a-fullerene [C_{60}] molecular systems. These complexes are a fractional realization of a modular carrier system. [Patent00, Röd06a, Jux06, Ran07b] In second line, a poly (ethylene-glycol) based polymer carrier and a styrene-maleic acid block-copolymer targeting system are investigated.

The thesis at issue is structured in separate sections. Following the introduction to photodynamic therapy and macromolecular carrier systems in chapter 2, the aim of the work is specified in detail in chapter 3. Section 4 contains descriptions of the used experimental set-ups, equations for data analysis and the used materials. In order to provide a basis for the theoretical calculations performed in subsequent sections, relevant fundamentals of photoinduced transfer processes are given in chapter 5.
In chapter 6 to 8, results of steady state and time-resolved spectroscopic measurements on these conjugates in solution and *in vitro* are presented as well as theoretical calculations. This allowed studying the photoinduced transfer processes in these novel macromolecules and resolving the intramolecular interactions limiting the photodynamic activity of photosensitizer-carrier complexes. Finally, conclusions are given in chapter 0.

2 Photodynamic Therapy

2.1 Principle of Photodynamic Therapy

In photodynamic therapy, maglinant tissue is selectively destroyed by a combination of a photosensitizing drug (photosensitizer) and light in the presence of oxygen. The schematic course of photodynamic therapy is illustrated in Figure 1. After injection, the photosensitizer needs to be enriched selectively in the target tissue which typically takes between 3 and 96 hours. [Bon95] Following the accumulation period, the abnormal tissue is illuminated by light of appropriate wavelength through an optical fiber or specialized optical system. The photosensitizer (PS) absorbs the light and, in the presence of molecular oxygen (O_2), generates singlet oxygen ($^1O_2$). This type of reactive oxygen species (ROS) damages vital structures and functions of cells, resulting in direct tumor tissue destruction. Associated effects include damage of the tumor associated vasculature that blocks the oxygen supply to the tumor and infiltration of lymphocytes, leukocytes and macrophages into PDT treated tissue, indicating activation of the immune response. [Dol02,Gol04] The selectivity of PDT is based on directing of light into the target tissue and on the enrichment of the photosensitizer in the target tissue through an appropriate carrier system.

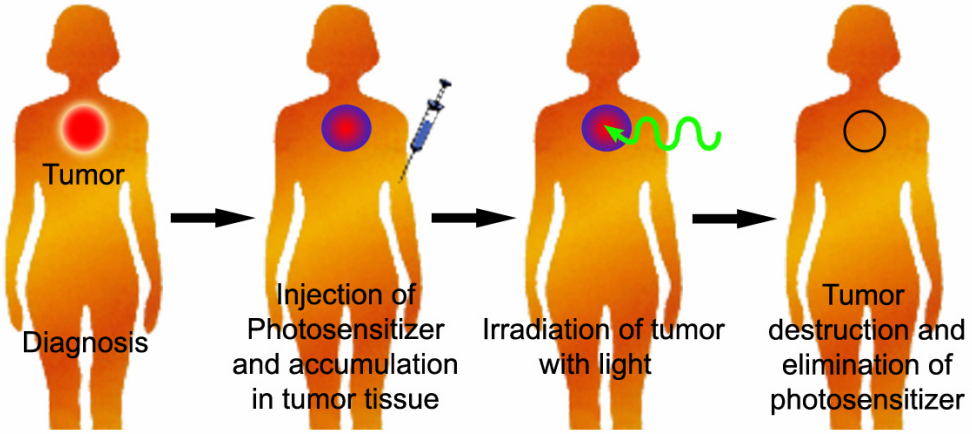

Figure 1. Schematic course of photodynamic therapy

Photosensitizers employed for PDT are mostly cyclic tetrapyrroles. [Röd90a, Ber05] They have an extended π-electron system which is the reason for a number of PDT relevant electronic properties. The molecules exhibit a high intersystem crossing and singlet oxygen quantum yield as well as long triplet lifetimes. [Kor98, Röd90b] As a subset of tetrapyrrolic compounds, porphyrins are used as photosensitizers for PDT. [Röd98,Wie01a,Wie01b] A

typical member is hematoporphyrin (Hp) derivate that was the first photosensitizer approved for clinical PDT in Canada in 1993 under the synonym Photofrin.[Nym04] Another representative of this class is zinc protoporphyrin which is part of the photosensitizer-carrier complexes investigated in chapter 7 and 8. Phorbides are also employed for PDT, a photosensitizer belonging to this family is pyropheophorbide a, part of the hexapyropheophorbide a-fullerene [C_{60}] molecular systems studied in chapter 6. [Reg07b, Ran07a, Erm05] Another class of molecules used as photosensitizers comprise the phthalocyanine and naphthalocyanine group. [Wöh06, Mak06, Pau02]

2.2 Photophysical processes of photosensitization

The primary photophysical processes involved in PDT are depicted in Figure 2. Through absorption of a photon of appropriate energy hν, the photosensitizing molecule is excited from its ground state (S_0) to the first excited singlet state (S_1) or to higher excited singlet states (S_2-S_n) in which case an immediate relaxation to the first excited state usually occurs (Kasha's rule). [Kas50]

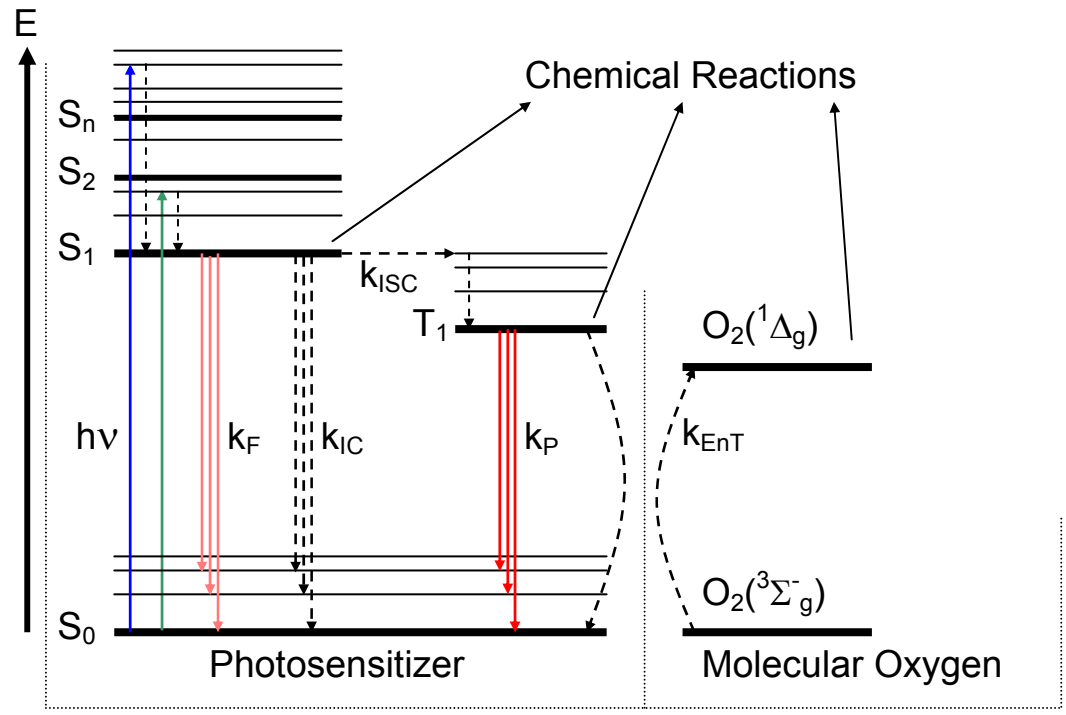

Figure 2. Jablonski diagram of the primary photophysical processes

The lifetime of the first excited state τ_F is typically in the nanosecond region which is too short to allow for significant chemical reactions with surrounding molecules. [Wan04] The S_1 state decays via fluorescence emission with rate k_F or nonradiative transitions (internal

conversion at rate k_{IC} or intersystem crossing k_{ISC}) to the ground state or first excited triplet state (T_1), respectively. [Lak99] [Bir70] An important parameter of the molecule is the fluorescence quantum yield (Φ_F). It can be calculated by

$$\Phi_F = \frac{k_F}{k_F + k_{IC} + k_{ISC}} \tag{2-1}$$

The transition $S_1 \rightarrow T_1$, known as intersystem crossing (ISC), involves a change of multiplicity, thus it is spin-forbidden. For tetrapyrrolic compounds this prohibition is weakened due to enhanced spin-orbit coupling leading to a high yield of triplet population. [Kas50, Kas52] The latter is characterized by the intersystem crossing quantum yield (Φ_{ISC}):

$$\Phi_{ISC} = \frac{k_{ISC}}{k_F + k_{IC} + k_{ISC}} \tag{2-2}$$

As direct transitions from the T_1 state to the ground state S_0 are strictly spin-forbidden, the lifetime of the triplet state is in the micro- to millisecond range. The long lifetime of the triplet state (τ_T) is a requirement for subsequent photoinduced chemical reactions which compete with phosphorescence emission occurring at low rate k_P.

There are two types of photodynamic reactions as defined by C.S. Foote, and followed by other authors. [Foo91, Sti93, Dou98, Nym04] An excited photosensitizer in the S_1 or T_1 state can react with a substrate or solvent (Type I) or with oxygen (Type II). In Type I reactions hydrogen or electron transfer may occur in both directions yielding radicals or radical ions. The produced reactive intermediates, for example hydroperoxyl, and hydroxyl radicals, as well as hydrogen peroxide, cause further oxidation of biomolecules. This may lead to cell death but concurrently the sensitizer radical immediately reacts with surrounding molecules. As a consequence the photosensitizer can not be activated repeatly. The disadvantage of the Type I mechanism is the lower efficiency of intermolecular reactions due to the short S_1 lifetime and the destruction of the photosensitizer. [Röd90a]

For tetrapyrrolic photosensitizers the Type II mechanism leads to reactive singlet molecular oxygen by energy transfer ($k_{EnT}[O_2]$) from the excited triplet photosensitizer to molecular oxygen ($^3O_2$) as illustrated in Figure 2. [Spi98, Pau04, Has89]. Additional deactivation pathways of the triplet state occurring with lower probability are electron transfer (k_{ET}) to molecular oxygen yielding O_2^- and physical quenching (k_{PQ}) by molecular oxygen. [Sch03] All of these processes depend on the concentration of molecular oxygen in the proximity of the photosensitizer. The competing processes leading to deactivation of the first excited triplet state can be summarized by the equations:

$$
\begin{aligned}
&P(T_1)+{}^3O_2 \xrightarrow{k_{EnT}[O_2]} P(S_1)+{}^1O_2 \\
&P(T_1)+{}^3O_2 \xrightarrow{k_{ET}} P^+ + O_2^- \\
&P(T_1)+{}^3O_2 \xrightarrow{k_{PQ}} P(S_1)+{}^3O_2 \\
&P(T_1) \xrightarrow{k_P} P(S_1) + h\nu_P
\end{aligned}
\qquad (2\text{-}3)
$$

In the following, we derive an expression, characterizing the ability of the photosensitizer to generate singlet oxygen in solution on the basis of the underlying photophysical processes. The proportion of the triplet state quenched by molecular oxygen (all processes) can be calculated by

$$S_\Delta = \frac{k_{EnT}[O_2] + k_{ET} + k_{PQ}}{k_P + k_{EnT}[O_2] + k_{ET} + k_{PQ}} \qquad (2\text{-}4)$$

The fraction of excited triplet sensitizer quenched by $^3O_2$ and leading to the generation of singlet oxygen is expressed by

$$f_T = \frac{k_{EnT}[O_2]}{k_{EnT}[O_2] + k_{ET} + k_{PQ}} \qquad (2\text{-}5)$$

The singlet oxygen quantum yield (Φ_Δ) of a photosensitizer is the ratio of photons absorbed to the number of singlet oxygen molecules generated, which is given by:

$$\Phi_\Delta = \Phi_{ISC} \cdot f_T \cdot S_\Delta = \Phi_{ISC} \cdot \frac{k_{EnT}[O_2]}{k_{EnT}[O_2] + k_{ET} + k_{PQ}} \cdot S_\Delta \qquad (2\text{-}6)$$

For tetrapyrroles under normal air conditions, phosphorescence emission has a very low probability compared to quenching processes in the presence of $^3O_2$, thus $k_P << (k_{EnT} + k_{ET} + k_{PQ})$. This means that equation (2-4) simplifies to $S_\Delta=1$ and the triplet state lifetime equals to $\tau_T = (k_{EnT}[O_2] + k_{ET} + k_{PQ})^{-1}$. The singlet oxygen quantum yield for tetrapyrrolic compounds can therefore be expressed as:

$$\Phi_\Delta = \Phi_{ISC} \cdot \tau_T \cdot k_{EnT}[O_2] \qquad (2\text{-}7)$$

In order to achieve a high singlet oxygen quantum yield Φ_Δ, the photosensitizing molecules should have a high intersystem crossing quantum yield Φ_{ISC}, a sufficiently long triplet state lifetime τ_T to increase the probability of close approaches to diffusing oxygen molecules and a high energy transfer rate k_{EnT} to molecular oxygen. [Lo03] The latter depends on additional characteristics which follow from the properties of singlet oxygen and the process of its generation.

2.3 Singlet molecular oxygen

The lowest excited singlet state $(2\sigma_g)^2\ (2\sigma_u)^2\ (3\sigma_g)^2\ (1\pi_u)^4\ (1\pi_g)^4$ ($^1\Delta_g$) of molecular oxygen lies by 0.94eV above the triplet ground state ($^3\Sigma_g^-$). [Mul32, Her34] As the transition from the ground state to the first excited state is strictly forbidden (violated selection rules for electronic dipole radiation: $\Delta S \neq 0$, $\Delta L \neq \pm 1$, parity is not different), the direct excitation by infrared light has a very low efficiency due to the weak absorbance. [Sch03] Excitation is therefore commonly realized by a spin-allowed energy transfer from a photosensitizer in the first excited triplet state, as it is utilized in PDT. For generation of singlet oxygen by energy transfer to $^3O_2$, the S_1-T_1 energy gap of the photosensitizer should be at least 0.94eV.

In pure liquids, the singlet oxygen lifetime τ_Δ strongly depends on the solvent due to physical quenching of $^1O_2$. In water a value of 3.1µs was obtained.[Sch92] The long lifetime of $^1O_2$, the allowed singlet-singlet reaction with organic molecules, and the excited state energy of about 94 kJ mol^{-1} are the reasons for the extraordinary chemical reactivity of singlet oxygen. It immediately reacts with biomolecules containing double bonds or allylic hydrogen by cycloaddition or the "ene" reaction, respectively. [Ran78, Aub95] When generated within cells, singlet oxygen destructs cellular constituents, e.g. membranes [Koc96], DNA [Rav04] and mitochondria [Pau03] which precipitates cell death. Due to the high reactivity, the lifetime of singlet oxygen in biological environments is very low $\tau_\Delta \leq 0.6\mu s$. [Moa90, Bak92, Nie02] The diffusion constant of $^1O_2$ in cells at room temperature is about $D = 1.4\times10^{-5} cm^2 s^{-1}$. [Moa81] Using these values, the mean diffusion length of $^1O_2$ can be calculated to $\delta = (6D\tau_\Delta)^{1/2} \leq 0.07\mu m$. From this estimation it is apparent that singlet oxygen reacts only on its side of formation.

The efficient generation of singlet oxygen is of key importance in the development of new photosensitizers, carrier systems and treatment conditions. Therefore the detection of singlet oxygen and determination of the $^1O_2$ lifetime, as an indicator of its immediate environment, has achieved great attention during the past decades. In the late 1970s direct spectroscopic detection of the weak 1270nm ($^1\Delta_g \rightarrow {}^3\Sigma_g^-$) phosphorescence emission from $^1O_2$ became possible. [Kra76] This method, using LN_2 cooled Ge-diodes as sensitive NIR detectors, has become the standard technique to investigate processes in which singlet oxygen is involved. Röder and co-workers demonstrated the time-resolved detection of singlet oxygen emission in a biological environment using red-cell ghost suspensions.[Oel94, Oel97] With the introduction of near infrared photomultipliers, whose quantum efficiency in the 1270nm region is an order of magnitude larger the Ge-diodes, the first determination of singlet oxygen

lifetime *in vivo* was made. [Nie02] Latest results showed that spatially resolved singlet oxygen detection is even possible on a subcellular level under the precondition that cells were incubated with D_2O. [And02, Zeb03, Zeb04, Sny04, Sko05, Sny05] In addition to the introduction to singlet oxygen, it is noteworthy that molecular oxygen has also a higher excited singlet state ($^1\Sigma_g^+$) with excitation energy of 157 kJmol^{-1} or 1.6eV. Direct excitation from the ground state violates the spin and parity selection rule, thus is not effective. Moreover the $^1\Sigma_g^+$ state is very fast and completely deactivated to the metastable $^1\Delta_g$ state in collisions with other molecules. [Sch03]

2.4 Factors affecting PDT efficiency

There are three areas to be considered for the design of effective PDT treatments. The first one concerns the photophysical and photochemical processes underlying PDT which have been introduced in the previous sections. The second matter deals with the application of light to the tumor, e. g. light doses, light penetration and light sources, a topic not covered in this thesis. The third area comprises *in vivo* transport and localization processes of the photosensitizing agent in the body which is dependent on the used carrier system.

So far in clinical PDT the first and second generation photosensitizers consisted of basic tetrapyrroles, therefore photosensitizing properties and tumor selective accumulation depended on the structure of the photosensitizer employed. [Wie01a] It turned out that not all demands of an effective treatment can be equally fulfilled by this approach. For example hydrophobic photosensitizers tend to aggregate in aqueous solutions decreasing their photodynamic activity, while hydrophilic photosensitizers display a decreased tumor cell uptake and are rapidly cleared in vivo. [Eic00, Röd00b, Woo92, Sch95] With the introduction of so called third-generation photosensitizers, consisting of the photosensitizing agent and a carrier system covering the whole pathway from administration to specific accumulation in tumor cells, more efficient PDT therapies can be developed. [Röd06a, Hel04, Ham01,Nos04] The requirements for suitable photosensitizers and the demands for adequate carrier systems are summarized in Table 1. An “ideal” photosensitizer should have a high singlet oxygen quantum yield, as outlined in section 2.2, and a high absorbance between 600nm and 900nm, in which biological tissue shows increased transmission. [Wil85, Nym04, All04] It should exhibit a low darktoxicity, meaning no toxicity without illumination, and a good biodegradability equivalent to a possible metabolic decomposition of the photosensitizer without the generation of toxic byproducts.

Photostability of the photosensitizer is required to avoid degradation of the molecule under illumination (photobleaching). On the contrary this can be an advantage as well because through degradation of the strongly absorbing photosensitizers in the upper cell layers, penetration of light to deeper tissues will be possible. [Pat94] The tendency of photosensitizers to aggregate within the cell is unwanted as it leads to a decrease of the triplet quantum yield as well as the singlet oxygen quantum yield according to equation (2-7) [Wan04, Eic00]

Table 1. Important requirements for effective photodynamic therapy

Photosensitizer related requirements	**Carrier system related demands**
High singlet oxygen quantum yield (Φ_Δ)	Selective accumulation in the tumor tissue
Strong absorption between 600nm-900nm	Enhancement of intracellular uptake
Low cytotoxicity	Low immunogenicity, Non toxicity
Biodegradability	High loading capacity
Photostability	Macromolecularity
Low self-aggregation within the tumor cell	Watersolubility (for parenteral administration)
Accumulation in vital subcellular structures of tumor cells	

A selective enrichment of the photosensitizer in tumor tissue keeps the concentration in healthy skin tissue low, thus the patient is not pronounced sensitive to sunlight, a serious problem in clinical treatment with photosensitizers of 1st generation.[Bel06] Moreover the amount of photosensitizer applied, in parenteral therapies typically 1-5mg photosensitizer per kg body weight, can be reduced. [Hir99, All04] A destruction of cancer cells via ROS generation is only achievable if the photosensitizer accumulates inside tumor cells, therefore the transport system should enhance the intracellular uptake of the photosensitizer. [Ran07b] Furthermore the carrier should be non-immunogenic and in a perfect sense completely shield the photosensitizer from its biological environment during passage to tumor cells ("Stealth delivery system"). This may result in minimization of systemic side effects, for example administrative irritations and pain, often observed in clinical PDT. [All04, Nym04] The carrier is supposed to have a high loading capacity for the photosensitizer. After tumor cell uptake the carrier releases the photosensitizer [Gil04, Rue99], or it remains attached to the dye molecules [Sav05]. In the first case the photosensitizer's tendency to accumulate in vital cell organelles, e.g. mitochondria, cell membrane (See section 2.3), is of importance while in

the latter case the carrier also influences the intracellular distribution of the photosensitizer.
Another requirement that has been gaining more attention during recent years is the macromolecularity of the carrier-photosensitizer complex. Small particles are rapidly washed out of the blood stream through the kidney whereas heavier particles have a longer plasma residence time [Mae01a]. The prolong circulation time is necessary to achieve higher concentrations of the complexes in the target tissues.

2.5 Macromolecular carrier systems

In this work polymers are used as building blocks of macromolecular carrier systems. Polymers are especially attractive, primarily because of their ease of processing and the ability to control their chemical and physical behaviour. Developments in polymer science allowed synthesizing water-soluble polymers which showed low immunogenicity, low polydispersity, nontoxicity and biodegradability which satisfies many of the demands disussed in the previous section. [Dun06, Haa06]
Macromolecular carrier systems for PDT can be classified into two categories according to their mechanism of targeting: active and passive targeting systems.

2.5.1 Active targeting

Active targeting refers to the efforts to increase the delivery of the photosensitizer to a target tissue through the use of specific interactions at target sites. These interactions include antigen receptor binding. [Yok05] To this category belong peptide-based delivery vehicles [Bis99], amino acid photosensitizer conjugates [Ogu05], glucose-based transporters [Zha03b] and photosensitizer immunoconjugates (PICs) employing antibodies as targeting units [Vro99, Sav03, Don04, Ran07b].

Several ways to realize such drug targeting systems have been proposed, initiated by Paul Ehrlich‘s vision of the “magic bullet” at the beginning of the last century. In 1975 Ringsdorf proposed a model where a number of drug molecules are bound by spacers to a linear polymer backbone to which targeting moieties or solubilizing groups may be connected additionally. [Rin75] An alternative concept was proposed by Röder, namely the modular carrier system (MCS) as depicted in Figure 3. [Röd00a] An adressing unit, e. g. an antibody or ligand, is connected to a multiplying system carrying a higher number of photosensitzing molecules

(PS) to achieve PDT relevant dye concentrations in the target tissue. The coupling of the several PS directly to the adressing unit may reduce its specific binding capability, therefore a multiplying system is employed which consumes only one binding site at the targeting unit.

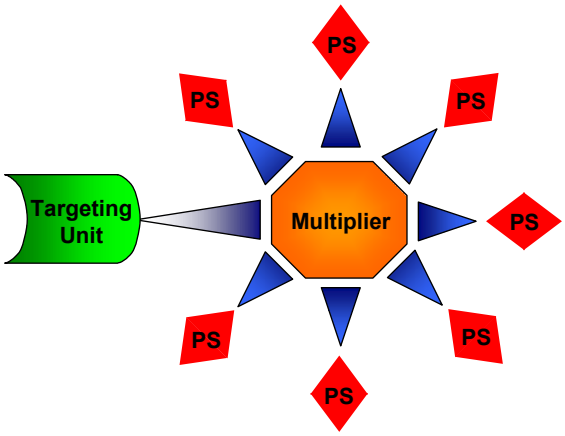

Figure 3. Scheme of the modular carrier system for PDT.

First attempts employed dendrimers as a multiplying systems.[Hac05, Pau03, Bat01] In this work hexapyropheophorbide a- fullerene [C_{60}] molecules were studied as a step towards the realization of a MCS. The multiplying system is constructed by a central building block, in this case a [C_{60}]-fullerene, and a dendritic branching architecture connecting the pyropheophorbide a photosensitizing moieties. [Erm05, Hel06, Röd06b, Reg07b]
In this work emphasis is placed on the photophysical transfer processes occurring in these multichromophoric conjugates after photoexcitation which directly influence their applicability as an active agent for PDT.

2.5.2 Passive targeting

Passive targeting is based on the physical and chemical properties of the carrier which are adjusted to meet the physiological differences between target and non-target tissues. Carriers belonging to this category include liposomes [Jia98, Der04, Sch05], protein nanoparticles [Pol02, Taw06], and polymeric micelles [Zha03a, Rob06, Reg07a, Nos04]. The power of passive targeting has been underestimated during the last ten years because it was not expected to reach the high specificity to target tissues that was possible with the use of antibodies. Due to the renaissance of the enhanced permeability and retention (EPR) effect discovered already in 1986 by Matsumura and Maeda, this situation has completely changed. [Mat86] Today passive accumulation in tumor tissue due to the EPR effect can be regarded as a standard for targeted delivery to solid tumors. For macromolecular carrier systems with

molecular weights above 40-50kDa, the EPR effect demonstrated *in vivo* drug enrichment factors beyond 2000 between blood stream and malignant tissue with high targeting accuracy [Mae00, Gre03].

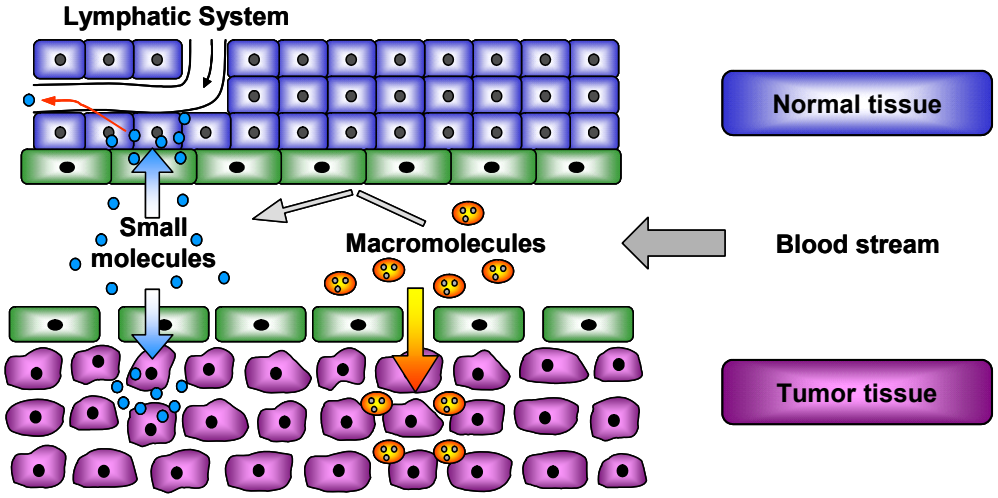

Figure 4. Schematic representation of the enhanced permeability and retention (EPR) effect.

The EPR-effect is based on structural differences between tumor tissue and healthy tissues. Low molecular weight compounds do not show any discrimination, they enter into normal and tumor tissue through the endothelia cell layer of blood capillaries by free diffusion-dependent equilibrium as shown in Figure 4. Macromolecules cannot pass the endothelial cell barrier of normal tissue but they can penetrate into tumor tissue because the endothelial cell layer of tumor tissue is leaky, resulting in an enhanced permeability of blood capillaries. In normal tissue clearance of macromolecules and small size particles occur rapidly and steadily via the lymphatic system whereas in tumor tissue the drainage system is defective. For this reason macromolecules are retained in the tumor and accumulate to high doses independent of the specific type of tumor. [Mae01a, Mae02]

In this thesis two constitutively different topologies of passively targeting carrier systems basing on the EPR-effect are investigated. Their principle structure is shown in Figure 5.

The first topology employs a linear polyethylene glycol (PEG) chain attached to Zn-protoporphyrin (ZnPP) by a spacer molecule. The PEG chain solubilizes the hydrophobic ZnPP molecule and imparts the desired macromolarity.

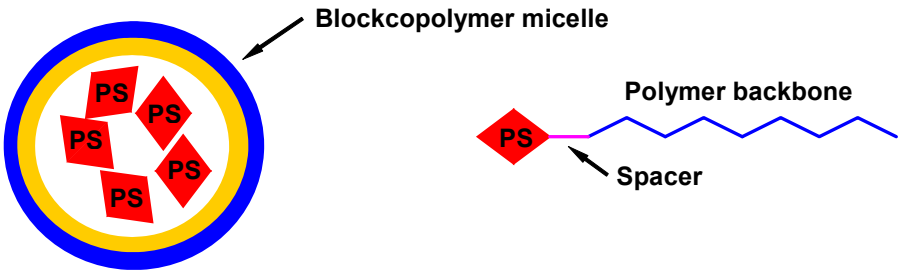

Figure 5. Passively targeting topologies of polymeric macromolecular carrier systems for PDT.

In contrast to the covalent coupling between PS and polymer carrier, the second system incorporates the photosensitizer in a non-covalent manner. It consists of a watersoluble poly styrene-maleic-acid (SMA) block-copolymer which forms stable micelles entrapping Zn-protoporphyrin.

3 Aim of the work

This thesis addresses a number of questions which influence the potential of the molecular systems under study for their use in photodynamic therapy. The questions may be divided into two groups.

The first issues address the suitability of the carrier system itself and the influence of the carrier system on incorporated or attached photosensitizers:

- Collection of basic photophysical properties of the carrier-photosensitizer complexes in solution in comparison to the photosensitizer alone.
- Does the polymer carrier change the ground state and/or excited state properties of the photosensitizer and if, how does it affect the photophysical parameters being relevant for PDT.
- Does the carrier system quench the generated singlet oxygen?
- Does the polymer carrier improve cellular uptake of the photosensitizer?
- Is the photosensitizer released by the transport system after tumor cell uptake?
- Which molecular topology of the systems investigated is most suitable for actively and passively targeting strategy?
- Are there any carrier induced effects which might be utilized to improve current PDT treatments?

The second set of questions is related to the photophysical interactions among photosensitizers in the different investigated systems as well as deactivation processes after photoexcitation:

- What kinds of energy transfer processes take place among photosensitizers incorporated or attached to the carrier after photoexcitation? What are the rate constants for these processes? How do they influence the energy transfer to molecular oxygen?
- In case that there are different types of interactions between photosensitizers, which process is dominant?
- How do the systems behave under *in vitro* conditions in comparison to their properties in solution?

The influence of the carrier system on the incorporated dye molecules and the photophysical interactions among photosensitzing molecules is expected to affect the phototoxicity of the studied systems against tumor cells. In order to evaluate this dependency, previous results from *in vitro* photobiological experiments will be reviewed and linked to the photophysical studies.

4 Experimentals

4.1 Methods

4.1.1 Steady state absorption and steady state fluorescence spectroscopy

Ground state absorption spectra were recorded using a commercial two beam-absorption spectrometer (UV-2501PC, Shimadzu, Japan) at room temperature. The optical density (OD) of the sample can be determined in the range from 200nm to 1100nm. The spectral bandwidth of the system is 2 nm and the error of the measured optical density is ±0.005 under the precondition that the OD ranges below 1.5. The precision of wavelength calibration is ± 0.5mm.

Steady state fluorescence spectra were measured in 1 cm × 1 cm Quartz optical cells containing the dissolved compound. The samples were excited using a combination of a cw-Xenon lamp (XBO 150, Osram, Germany) and a grating monochromator (model 77250, Lot-Oriel, Germany). A polychromator with an attached cooled CCD sensor (InstaSpec IV, Lot-Oriel, Germany) served to record photons emitted by the sample in the range between 400nm and 930nm. The fluorescence quantum yield of an unknown compound Φ_u can be obtained by comparison of the fluorescence intensity relative to a known standard according to

$$\Phi_u = \frac{A_S \cdot F_u \cdot n^2}{A_u \cdot F_S \cdot n_0^2} \cdot \Phi_S \qquad (4\text{-}1)$$

, where: the u subscript refers to the unknown and s to the standard and other symbols have the following meanings: (Φ is quantum yield, A is absorbance at the excitation wavelength, F is the integrated emission area across the band and n's are index of refraction of the solvent containing the unknown (n) and the standard (n_0), respectively. [Par60, Eat88]

4.1.2 Fluorescence lifetime measurements by TCSPC

Fluorescence lifetimes were measured by time-correlated single photon counting (TCSPC) technique [Con84]. It relies on the concept that the probability distribution for emission of a single photon after excitation yields the actual intensity distribution over time of all the photons emitted as a result of excitation. By sampling the single photon emission after a large number of excitation flashes, the experiment constructs this probability distribution or in other

words the fluorescence decay of the sample. The experimental set-up is shown in Figure 6. The femtosecond pulses of a mode-locked Ti:Sapphire laser (Coherent Mira 900, FWHM 200 fs, 75MHz) were frequency doubled by Second Harmonic Generation (SHG). These pulses (400nm) were used to excite the samples located in the probe chamber (Pr). The adjustment of polarizer P_1 allowed tuning the intensity of the laser beam in combination with the fixed polarisator P_2. The intensity was adjusted so low that approximately one fluorescence photon is detected every few hundred excitation pulses which satisfies the single photon counting condition. The excitation pulse is split such that a photodiode (PD) is triggered at the same time that the sample is excited and when a fluorescence photon is detected by the microchannel plate photomultiplier (S 3809, Hamamatsu), the time difference is measured electronically (SPC 600, Becker & Hickl GmbH, Germany). A monochromator (MC) in the detection path served to select the detection wavelength whereas an additional filter (F) cuts off scattered excitation light. All measurements were performed in the magic angle (Analyser A set to 54.7^0) to cancel out the influence of time-resolved anisotropies. [Mak06, Kor98]

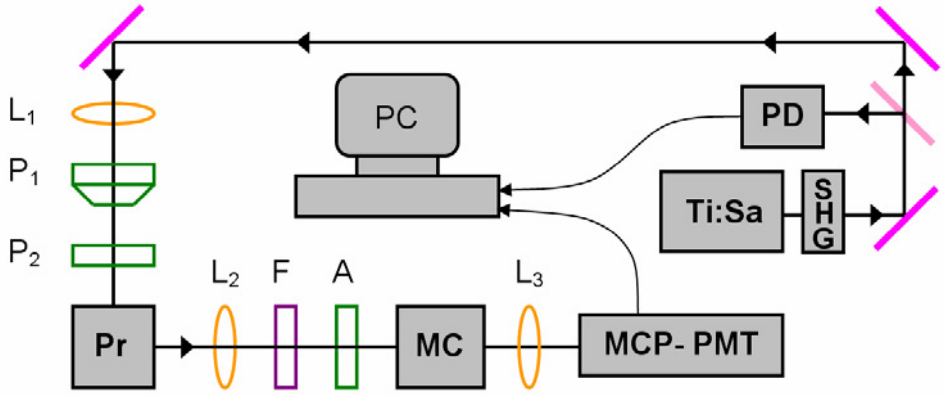

Figure 6. Schematic assembly of the TCSPC set-up. A: Analyser, F: Filter, $L_{1,2,3}$: Lenses, MC: Monochromator, $P_{1,2}$: Polarizer, PD: Photodiode, MCP-PMT: Micro channel plate photomultiplier, Pr: Probe chamber, SHG: Second Harmonic Generation

Depending on the sample, it is assumed that the fluorescence decay is one or multiexponential and can be described by a model function according to:

$$I(t) = \sum_{i=1}^{1-n} a_i \cdot \exp\left(-\frac{t}{\tau_i}\right) \qquad (4\text{-}2)$$

Because of the finite duration of the excitation puls and the response of the PMT, the measured fluorescence decay $M_E(t)$ is actually a convolution of the instrument function IRF(t) with I(t). The IRF could be measured at the excitation wavelength with Ludox (Aldrich, Germany), the FWHM of the IRF was determined to 80ps.

A testfunction M_T can be generated which predicts the measured fluorescence decay in dependence on the paramters a_i and τ_i contained in the model function.

$$M_T(t, a_i, \tau_i) = \int_0^t IRF(t')I(t-t')dt' \qquad (4\text{-}3)$$

Minimization of the least-square error function between M_T and M_E allows determining the parameters of the fluorescence decay:

$$\chi^2 = \sum_{k=1}^{n} \frac{[M_E(t_k) - M_T(t_k)]^2}{M_E(t_k)} \qquad (4\text{-}4)$$

A routine (vfit, written by S. Tannert) was applied to minimize the least-square error between the model function convoluted with the instrument response function and the measured data set.

4.1.3 Steady-state singlet oxygen luminescence spectroscopy

Spectrally resolved measurements of the weak 1270nm singlet oxygen luminescence generated by the sample were carried out utilizing the set-up depicted in Figure 7. A cw Ytterbium:YAG laser (Versadisk, ELS, Germany) equipped with a SHG unit was used to excite the sample within the probe chamber (Pr) at 515nm with 5-10mW power. The emitted luminescence was focused on the entrance slit of a Czerny-Turner monochromator (Digikröm 240, CVI Laser Corporation, USA, grating: Au coated, 600 lines/nm).

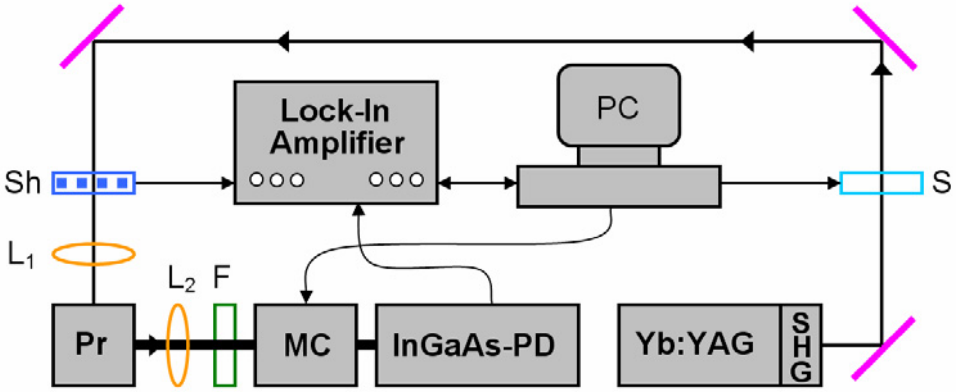

Figure 7. Schematic assembly steady-state singlet oxygen luminescence set-up. F: Silicon-Filter, InGaAs-PD: liquid nitrogen cooled InGaAs-photodiode, L_1,L_2: lenses, MC: Monochromator, Pr: Probe chamber, S: Shutter, Sh: Shopper, SHG: Second Harmonic Generation

The fluorescence emitted from the sample was suppressed by Silicon filter (F) placed in front of the entrance slit. The singlet oxygen luminescence was detected by a slow (f_{max}~20Hz)

liquid-nitrogen cooled InGaAs photodiode (ILN020, Electro-Optical System, USA). Lock-in technique was employed to recover the luminescence signal from the noise background. For this purpose a shopper (Sh) operating at 4Hz modulated the excitation beam. The sinusoidal signal from the photodetector was fed in the Lock-in amplifier (Mod. 5109, EG&G, USA) together with reference signal from the chopper. The output voltage signal of the Lock-in was read out by a personal computer (PC) which also controlled an additional shutter (S) to prevent photobleaching of the sample prior to the measurement. [Spi98]

For a homogenous solution, the signal obtained from the photodiode is given by the product of the sensitivity α of the set-up, the radiative decay constant of singlet oxygen k_r and the number of singlet oxygen molecules $[^1O_2]$ contributing to the signal.

$$I = \alpha \cdot k_r \cdot \left[{}^1O_2\right] \tag{4-5}$$

The number of singlet oxygen molecules can be obtained by solving the differential equations under steady state conditions and constant illumination I_{ex} of the sample basing on the processes shown in the Jablonski diagram. (See Figure 2.) By a stepwise procedure, starting with $[S_1]$ state, followed by the $[T_1]$ state, we can obtain the $[^1O_2]$ population:

$$\begin{aligned}
\left[\dot{S}_1\right] &= -\frac{\left[S_1\right]}{\tau_F} + I_{ex}(1-10^{OD}) \overset{!}{=} 0 \quad \Rightarrow \quad \left[S_1\right] = \tau_F \, I_{ex}(1-10^{OD}) \\
\left[\dot{T}_1\right] &= -\frac{\left[T_1\right]}{\tau_T(O_2)} + k_{ISC}\left[S_1\right] \overset{!}{=} 0 \quad \Rightarrow \quad \left[T_1\right] = \tau_T(O_2) k_{ISC} \tau_F \, I_{ex}(1-10^{OD}) \\
\left[{}^1\dot{O}_2\right] &= -\frac{\left[{}^1O_2\right]}{\tau_\Delta} + k_{EnT}\left[T_1\right] \overset{!}{=} 0 \quad \Rightarrow \quad \left[{}^1O_2\right] = \tau_\Delta k_{EnT} \tau_T(O_2) k_{ISC} \tau_F \, I_{ex}(1-10^{OD})
\end{aligned} \tag{4-6}$$

I_{ex} is the number of incident photons per second along the optical path and the product $I_{ex}(1-10^{OD})$ refers to the number of excited photosensitizer molecules per second. For a description of τ_F, k_{ISC}, k_{EnT} and τ_Δ see section 2.2 and 2.3. The expression for the $[^1O_2]$ state can be further simplified by introducing $\Phi_{ISC} = k_{ISC} \cdot \tau_F$ and substituting equation (2-7). We get:

$$\left[{}^1O_2\right] = \tau_\Delta \Phi_\Delta I_{ex}(1-10^{OD}) \tag{4-7}$$

Replacing the expression for $[^1O_2]$ in equation (4-5), yields the equation for the signal measured by the photodiode:

$$I = \alpha \cdot k_r \cdot \tau_\Delta \cdot \Phi_\Delta \cdot I_{ex} \cdot (1-10^{OD}) \tag{4-8}$$

The measured signal is directly proportional to the singlet oxygen quantum yield of the sample. This opens up the possibility of determining the singlet oxygen quantum yield of an

unknown sample by comparison of the spectrally integrated signal generated by the unknown compound and a known standard. If the sensitivity of the set-up α, the optical density OD, the excitation intensity I_{ex} and the singlet oxygen lifetime τ_Δ are kept constant, the singlet oxygen quantum yield of the unknown sample is given by:

$$\Phi_\Delta^{sample} = \frac{I^{sample}}{I^{ref}} \cdot \Phi_\Lambda^{ref} \qquad (4\text{-}9)$$

4.1.4 Time-resolved singlet oxygen luminescence

The time-resolved detection of singlet oxygen generated by the photosensitizer was performed by measurement of the 1270nm luminescence of $^1O_2$. The experimental set-up is shown in Figure 8. The sample in the probe chamber (Pr) was excited using the pulses generated by an optical parametric oscillator (OP 901-355, BM Industries) which was pumped by the THG of a Nd:YAG laser (BM Industries, Evry Cedex, France). Pulses are generated at a frequency of 20Hz, the length of the excitation puls is a few nanoseconds and the energy of each puls ranges between 0.1 and 1 mJ which could be controlled utilizing a puls energy meter (PEM100, LTB, Berlin).

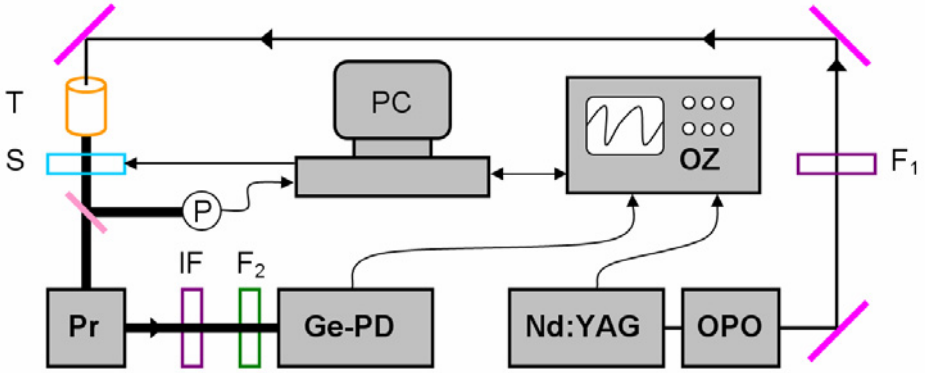

Figure 8. Schematic assembly of the time-resolved singlet oxygen luminescence set-up. $F_{1,2}$: Filter, Ge-PD: liquid nitrogen cooled Ge-photodiode, IF: Interference filter, OPO: Optical parameteric oscillator, OZ: Oscilloscope, P: Puls energy meter, Pr: Probe chamber, S: Shutter, T: Telescope

A telescope (A) served to widen the beam and a filter (F_1) was employed to limit the intensity of the excitation light. The singlet oxygen emission was detected using a liquid nitrogen cooled Ge-photodiode (North Coast, Inc., Santa Rosa, CA). For wavelength selection, a combination of a silicon filter (F_2) and interference filter (IF) for 1270 nm was placed in front of the Ge-photodiode. An oscilloscope (HP 54542A, Hewlett Packard, USA) recorded the

detector signal over time which in turn was transmitted to a personal computer (PC). The latter also controlled a shutter (S) to prevent photobleaching of the sample prior to the measurement. [Oel97]

Similar to the steady-state singlet oxygen measurement, the signal obtained from the photodiode is governed by equation (4-5) but the number of singlet oxygen molecules is now time-dependent. The time evolution of $[^1O_2]$ can be obtained by solving the differential equation for the $O_2(^1\Delta g)$ state basing on the processes shown in the Jablonski diagram. (See Figure 2.) Inserting the solution in equation (4-5) yields the rise and decay kinetics of the time-resolved $^1O_2$ signal:

$$I(t) = \alpha \cdot k_r \cdot \Phi_\Delta \cdot \frac{\tau_\Delta}{\tau_\Delta - \tau_T(O_2)} \cdot \left[\exp\left(-\frac{t}{\tau_{^1O_2}} \right) - \exp\left(-\frac{t}{\tau_T(O_2)} \right) \right] \cdot I_{ex} \cdot (1 - 10^{OD}) \qquad (4\text{-}10)$$

,where the product $I_{ex}(1\text{-}10^{OD})$ denotes the number of excited photosensitizing molecules shortly after excitation (t=0). τ_Δ and $\tau_T(O_2)$ are the singlet oxygen lifetime and the lifetime of the first excited triplet state of the photosensitizer under the presence of oxygen. From equation (4-10) it is apparent that the amplitude of I scales linear with the singlet oxygen quantum yield. This opens up the possibility of determining the singlet oxygen quantum yield of an unknown sample by comparison of the signal generated by the unknown compound and a known standard. Under the conditions that sample and reference compound are dissolved in the same solvent and exhibit the same optical density at the excitation wavelength, the singlet oxygen quantum yield of the unknown sample is given by:

$$\Phi_\Delta^{sample} = \frac{I^{sample} \cdot I_{ex}^{ref}}{I^{ref} \cdot I_{ex}^{sample}} \cdot \Phi_\Lambda^{ref} \qquad (4\text{-}11)$$

, where I^{sample}, I^{ref} are the measured amplitudes of the 1270 luminescence signal and I_{ex} refers to the excitation puls energies for sample and reference accordingly. For the validity of equation (4-11) it is further necessary that the sensitivity α of the set-up is held constant and the excitation intensity is kept low to avoid bleaching effects.

4.1.5 Laser flash photolysis

In this work, laser flash photolysis was employed to study the time-dependent population of the first excited triplet state of the photosensitizer. Figure 9 depicts the experimental set-up. The probe was excited using laser pulses emerging from the OPO system / Nd:YAG laser as already described in section 4.1.4. The cw probe beam traversed the sample perpendicular to

the excitation beam and was generated by a combination of a Xenon arc lamp (XBO 100, Osram, Germany) with attached monochromator. The transmitted light passed an interference filter for the wavelength of the probe beam to suppress scattered excitation light in addition to fluorescence emitted by the sample and was further detected by a fast Si-photodiode. The signal was amplified, recorded by an oscilloscope (HP 54542A, Hewlett Packard, USA) and transmitted to a personal computer.

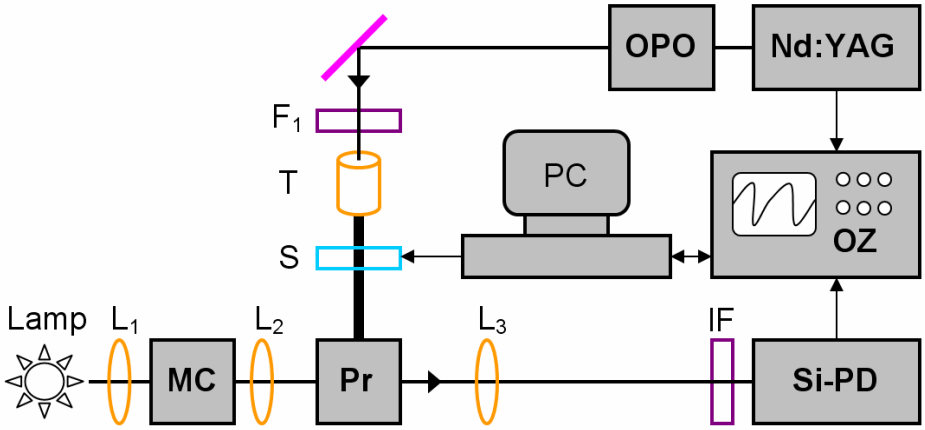

Figure 9. Schematic assembly of the laser-flash photolysis set-up. F_1: Filter, IF: Interference filter, $L_{1,2,3}$: Lenses, OPO: optical parameteric oscillator, OZ: Oscilloscope, Pr: Probe chamber, S: Shutter, PD: fast Si-photodiode, T: Telescope

The parameter monitored by laser flash photolysis is the time-dependent change in the sample's optical density ΔOD(t) probed at the wavelength λ of the T_1-T_n transition of the photosensitizer, and it is given by

$$\Delta OD_\lambda(t) = OD_\lambda(t \prec 0) - OD_\lambda(t) = \log_{10}\left(\frac{I_0}{I(t)}\right) = \Delta\varepsilon_T \cdot [T_1] \cdot l \qquad (4\text{-}12)$$

where OD(t<0) and OD(t) are the optical densities before and after excitation, respectively. These are related by the Lambert-Beer Law to the intensities of the transmitted light before and after excitation denoted by I_0 and I(t), respectively, or to the product of the triplet difference molar absorption coefficient $\Delta\varepsilon_T(t)$, the time-dependent concentration of the molecules in the first excited triplet state $[T_1]$ and the path length l through the sample solution.

The decadic logarithm in equation (4-12) can be substituted by the natural logarithm due to the identity $\log_{10}(x) = \ln(x)/\ln(10)$. For small changes of x around 1, the natural logarithm can be approximated by $\ln(x) \approx x\text{-}1$. Expression (4-12) can further be simplified to

$$\Delta OD_{\lambda}(t) = \frac{I_0 - I(t)}{I(t) \cdot \ln 10} \approx \frac{\Delta I}{I_0 \cdot \ln 10} = \Delta \varepsilon_T \cdot [T_1] \cdot l \qquad (4\text{-}13)$$

Equation (4-13) shows that by measuring the change in the intensity ΔI, the time-resolved decay of the first excited triplet state can be obtained.

The method of laser flash photolysis was also used to determine the generation of singlet oxygen indirectly via triplet lifetime measurement. In the following, an expression is derived relating the first excited state triplet lifetime τ_T in the presence and absence of oxygen to the singlet oxygen quantum yield Φ_Δ.

In the absence of molecular oxygen in solution (remove of oxygen by flushing of the sample with N_2 gas), a sample excited to the first excited triplet state T_1 will decay with an unimolecular (first order) decay rate constant $k(N_2)$. This constant is the sum of all deactivation processes of the triplet state in the absense of molecular oxygen and is given by $k(N_2) = k_{ET} + k_{PQ}$ as explained in section 2.2. This is only valid under the precondition that low intensity excitation pulses (<10% conversation to the triplet state) are used. In this case interactions among excited triplet photosensitizers are improbable due to the low generated concentration of triplet photosensitizers $[T_1]$. The concentration decreases with time according to:

$$\frac{d[T_1]}{dt} = -k(N_2) \cdot [T_1] \quad k(N_2) = \frac{1}{\tau(N_2)} = k_{ET} + k_{PQ} \qquad (4\text{-}14)$$

The decay lifetime of the triplet state in the absence of oxygen $\tau(N_2)$ can be obtained by an exponential fit to ΔOD(t) or ΔI(t). When the triplet state is being quenched by molecular oxygen, a second order decay is observed:

$$\frac{d[T_1]}{dt} = -k(N_2) \cdot [T_1] - k_{EnT} \cdot [T_1] \cdot [O_2] = -[T_1] \cdot \{k(N_2) + k_{EnT}[O_2]\} \qquad (4\text{-}15)$$

Normally the ground state oxygen concentration $[O_2]$ (typically 10^{-3} to 10^{-4} M) is much higher than the concentration of photosensitizers in the triplet state (typically 10^{-6} to 10^{-7} M) and so a pseudo-first order rate constant $k(O_2)$ can be assumed:

$$\frac{d[T_1]}{dt} = -k(O_2) \cdot [T_1] \quad k(O_2) = \frac{1}{\tau(O_2)} = k(N_2) + k_{EnT} \cdot [O_2] \qquad (4\text{-}16)$$

The triplet lifetime in the presence of oxygen and absence of oxygen is given by $\tau_T(O_2) = \left(k_{EnT}[O_2] + k_{ET} + k_{PQ}\right)^{-1}$ and $\tau_T(N_2) = \left(k_{ET} + k_{PQ.}\right)^{-1}$, respectively. Substituting both expressions in equation (2-6), the value of the singlet oxygen quantum yield can be indirectly

determined by:

$$\Phi_{\Delta} = \Phi_{ISC} \cdot \left(\frac{\tau_T(N_2) - \tau_T(O_2)}{\tau_T(N_2)} \right) \cdot S_{\Delta} \qquad (4\text{-}17)$$

4.1.6 Picosecond transient absorption spectroscopy (ps-TAS)

Transient absorption spectroscopy (TAS) is usually performed to follow population dynamics of different electronic states and deactivation processes after excitation. The typical pump-probe experimental set-up is shown in Figure 10.

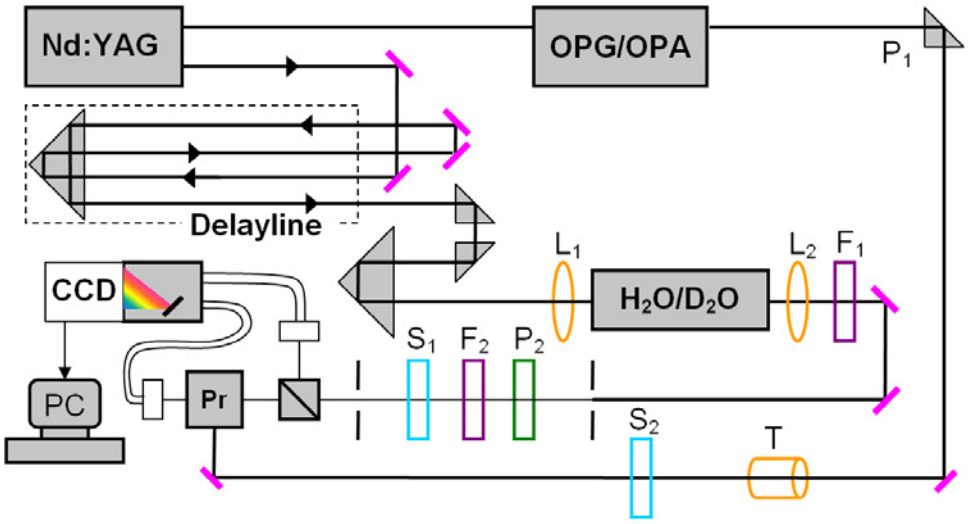

Figure 10. Schematic assembly of the ps-TAS set-up., $F_{1,2}$: Filter, $L_{1,2}$: Lenses, OPG/OPA: optical parametric generation/amplification, P: Polarizer, Pr: Probe, $S_{1,2}$: Shutter, T: Telescope

The probe beam consisted of a white light continuum which was generated in a cell with D_2O/H_2O mixture using intense 25 ps single pulses from a Nd:YAG laser (PL 2143A, Ekspla) at 1064 nm. Before focusing into the cell using lens L_1, the IR laser radiation passes through the 4-pass mechanical delay line to introduce a time delay up to 15ns with respect to the pumping light. After white-light was generated, it is re-collimated by a lens L_2 and traverses a filter F_1 to remove remaining IR laser radiation. Two pinholes reduce the diameter of the white light beam to 1 mm, a second filter F_2 allowed adjusting the intensity of the beam. The polarizer P_2 was set to the magic angle (54.7^0) in order to avoid time-dependent anisotropy. Before passing through the probe Pr, the continuum radiation was split to get a reference spectrum. The transmitted as well as the reference beam were focused into two optical fibers and were recorded simultaneously at different traces on a CCD-matrix (Lot-Oriel, Instaspec IV). Radiation from an OPG/OPA (Ekspla PG 401/SH, tuning range 200 – 2300 nm) pumped

by third harmonic of the same laser was used to excite the molecules at the chosen optical transition. Polarization rotating prism P_1 rotated the polarization plane of the excitation beam from horizontal to vertical and the telescope was introduced to increase the homogeneity of the excited area. The pump beam is focused slightly by a cylindrical lens to obtain a 5mm × 2 mm excited area on the 5mm Quartz cell. The probe beam passes through the excited region just behind the front wall of the cell.

The measurand of TAS is the change in the optical density of the sample ΔOD(λ,t) in dependency of the delay between pump puls and probe puls

$$\Delta OD(\lambda,t) = OD^*(\lambda,t) - OD(\lambda) = -\log_{10}\left\{\frac{T(\lambda)}{T^*(\lambda,t)}\right\} \tag{4-18}$$

, where OD^*, T^* are the optical density and transmission of the excited probe. OD and T refer to the optical density and transmission of the non-excited probe. The analysis of TAS spectra is more complicated because three different processes (transients) contribute to the ΔOD signal. Firstly, a fraction of the photosensitizer molecules remain in the ground state and therefore show a reduced or so-called saturated absorption compared to the unexcited ensemble. This behaviour is characterized by an absorption cross section σ_{GA} and leads to a negative ΔOD signal. Second, the photosensitizer molecules in the excited S_1 state or T_1 state cause a positive ΔOD signal due to possible transitions to higher excited states. An induced absorption cross section σ_{IA,S_1} for S_1-Sn transitions or σ_{IA,T_1} for T_1-T_n transitions reflects this feature. Third, the probe beam causes stimulated emission emerging from the photosensitizer's excited S_1 state. This process, named transient amplification, is described by the absorption cross section σ_{TA} and leads to a negative ΔOD signal. Considering all of the three transients, the ΔOD signal for a three-level (S_0,S_1,T_1) system is given by

$$\Delta OD(\lambda,t) = \frac{l}{\ln 10}\left\{\left(\sigma_{IA,S_1} - \sigma_{TA}\right)\cdot[S_1] - \sigma_{GA}\cdot\Delta[S_0] + \sigma_{IA,T_1}\cdot[T_1]\right\} \tag{4-19}$$

, where $\Delta[S_0] = [S_1] + [T_1]$ denotes the ground state depletion. [Zeu02b] As the transients are located separately or partly overlapping in the ΔOD(λ,t) spectra, the time-evolution of the S_1 and S_0 state can be obtained in addition to excited state absorption cross sections and intersystem crossing efficiencies. This was accomplished by utilizing a fitting procedure described in [Rüc97] and coded by Dr. A. Zeug.

4.2 Materials

4.2.1 P6, FHP6 and FP6

The hexapyropheophorbide a-fullerene [C60] super molecules were synthesized by Dr. Matthias Helmreich and Dr. Jux from the research group of Prof. Hirsch. Erlangen University, Germany. The preparation of **FHP6**, **P6** and **FP6** and reference materials P1, P2 included a high number of synthetic steps and elaborate purification and characterization procedures. These are described in detail in the doctoral thesis of Dr. Helmreich. [Hel06]

Briefly, for the synthesis of **FHP6** and **FP6**, malonic acid was modified by the attachment of a C_6-spacer unit and further coupled to a first generation Newkome dendrimer. The resulting malonate was deprotected and subsequently reacted with the pyropheophorbide carrier to give the desired reference material **P6**. For the synthesis of **FP6** the malonate was coupled to C_{60} yielding the fullerene monoadduct. After removal of the protecting groups, the fullerene hexaacid was obtained and immediately coupled with the pyropheophorbide carrier which yields compound **FP6**. To obtain **FHP6** five additional diethyl malonates were coupled to the fullerene core on the stage of the fullerene monoadduct. The resulting [5:1]-hexakisadduct was deprotected and subsequently coupled to the pyropheophorbide carrier, thus the desired [5:1]fullerene hexakisaddukt **FHP6** was obtained.

4.2.2 PEG-Zinc protoporphyrin

The synthesis of **PEG-ZnPP** was performed in the research group of Prof. Maeda at Kumamoto University School of Medicine, Japan. The sequence of synthetic steps required to obtain the pegylated form of ZnPP is described in detail in reference [Sah02]. Firstly an aminated derivate of protoporphyrin was obtained by a stepwise reaction with ethylchloroformate and ethylenediamine. The resulting bis(ethylenediamino)protoporphyrin was reacted with succinimidyl PEG (average MW of 5000). In order to remove unreacted PEG, dialysis against distilled water was performed yielding the pegylated protoporphyrin (PEG-PP). By addition of zinc acetate to a solution of PEG-PP in chloroform, chelation of Zn^{2+} into the porphyrin macrocycle occurred. The product **PEG-ZnPP** was dialysed again to obtain pure pegylated ZnPP. The material was characterized by size exclusion chromography und complete reaction between succinimidyl PEG and aminated ZnPP was checked by quantification of the free amino groups of **PEG-ZnPP**.

4.2.3 SMA-Zinc protoporphyrin

SMA-ZnPP was also prepared in the group of Prof. Maeda in Japan. The synthesis of this material has been published previously. [Iye07] In a first step the SMA copolymer with a mean molecular weight of 1280Da was purified by a solvent precipitation technique. Afterwards the maleic anhydride residue of the SMA polymer was hydrolyzed to the water-soluble maleic acid form by addition of NaOH. Later, the SMA was neutralized and freeze-dryed. ZnPP was synthesized by addition of zinc acetate to a solution of protoporphyrin in DMSO. **SMA-ZnPP** micelles were prepared by dissolving ZnPP in DMSO and addition of hydrolyzed SMA (1:1 weight ratio). The hydrolyzed SMA instantaneously formed hydrophobic associations with ZnPP leading to precipitation of the micelles. Through subsequent centrifugation and washing procedures DMSO was removed and the micelles were resuspended in H_2O. The solution was titrated with NaOH to pH 10.45 and adjusted back to 7.4 by addition of HCl. Finally ultrafiltration with a membrane (cut-off of 10kDa) was carried out to purify and concentrate the **SMA-ZnPP** micelles.

5 Theoretical Fundamentals of Photoinduced Transfer Processes

This chapter introduces the concepts of electronic energy transfer (EET) and electron transfer (ET) processes of photoexcited molecules in solution. The description of the underlying theory is restricted to those types of EET and ET processes which are relevant for the analysis of the photophysical investigations carried out in this work.

5.1 Energy Transfer Processes

Energy transfer processes are regarded as a transfer of excited state energy from a donor (D) to an acceptor (A) molecule. The discussion is focused on incoherent nonradiative electronic energy transfer processes of optically excited molecules. The EET process can be described by the general scheme:

$$D + A \xrightarrow{h\nu} D^* + A \xrightarrow{\text{Energy Transfer}} D + A^* \qquad (5\text{-}1)$$

Through absorption of a light quantum hν, the ground state donor molecule undergoes a transition to an excited state. The following energy transfer from D to A may occur by different mechanisms depending on the strength of the interaction between D and A.

Simpson and Peterson proposed a practicable criterion to estimate the strength of the interaction and thus, provided a classification of the energy transfer mechanisms. [Sim57] This criterion is based on a characteristic result of the interaction between D and A, namely the generation of an exciton band. Its bandwidth (2U) is dependent on the oscillator strength of the corresponding electronic transitions, their relative orientation and it is dependent on the distance between D and A. [Dav62] The strong and weak coupling cases are characterized by the criteria $2U/\Delta\varepsilon >> 1$ and $2U/\Delta\varepsilon << 1$, where $\Delta\varepsilon$ is the Frank-Condon band width of the corresponding molecular electronic transition in the individual molecular unit.

Both cases can be treated by exciton theory which is being briefly introduced in the next section. [Kas63] In case of very weak coupling, stated by the modified criteria $U/\Delta\varepsilon' << 1$, where $\Delta\varepsilon'$ is the individual vibronic band width, energy transfer occurs by a dipole-dipole resonance interaction, the so-called Förster resonance energy transfer (FRET). [För48] This type will be discussed in section 5.1.2.

5.1.1 Exciton theory for molecular dimers

The formal treatment of the interaction between two identical molecules was firstly elaborated by Michael Kasha. [Kas65] The theoretical description of molecular dimers undergoing strong coupling is especially significant for the understanding of photophysical data obtained for the systems studied during this work. For this reason the exciton theory for molecular dimers will be presented in the following.

Kasha used first order perturbation theory to estimate the interaction between donor (D) and acceptor (A). The overlap of the wavefunctions is assumed to be small, so that the Hamiltonian operator can be written as the sum of the monomer operators plus a perturbation term describing the interaction:

$$\hat{H} = \hat{H}_A + \hat{H}_D + \hat{V}_{DA} \tag{5-2}$$

The perturbation term $\hat{V}_{DA}$ has the form:

$$\hat{V}_{DA} = \underbrace{-\sum_{i,j}\frac{e^2}{\overrightarrow{R_{Ai}}-\overrightarrow{r_{Dj}}}-\sum_{i,j}\frac{e^2}{\overrightarrow{R_{Di}}-\overrightarrow{r_{Aj}}}}_{V_1}+\underbrace{\sum_{i,j}\frac{e^2}{\overrightarrow{R_{Ai}}-\overrightarrow{R_{Di}}}}_{V_2}+\underbrace{\sum_{i,j}\frac{e^2}{\overrightarrow{r_{Ai}}-\overrightarrow{r_{Di}}}}_{V_3} \tag{5-3}$$

where $\overrightarrow{R_{Ai}}$ are the coordinates of the nuclei and $\overrightarrow{r_{Ai}}$ refer to the coordinates of the electrons of acceptor A. The donor coordinates are named accordingly. The interaction is described by three contributions. The attraction between donor nuclei and acceptor electrons and vice versa is represented by the first potential V_1 in equation (5-3). The second one (V_2) characterizes the Coulomb repulsion between donor and acceptor nuclei wheras the third term (V_3) reflects the repulsion of the electrons belonging to donor and acceptor, respectively.

The ground state wavefunction of the dimer is given by the product of the ground (G) state monomer wavefunctions $|\Psi_G\rangle = |\psi_A\rangle|\psi_D\rangle$. The energy E_G of the ground state dimer can be obtained by solving the time-independent Schrödiger equation:

$$\hat{H}|\Psi_G\rangle = E_G|\Psi_G\rangle \quad \Rightarrow \quad E_G = E_A + E_D + \langle\psi_A\psi_D|\hat{V}_{DA}|\psi_A\psi_D\rangle \tag{5-4}$$

The solution shows that E_G is given by the sum of the ground state energies of the monomer (E_A, E_D) and the van der Waals interaction energy which corresponds to the last term on the right-hand side of equation (5-4). The van-der-Waals term lowers the energy of the dimer. In the next step, we are interested in the excited states of the dimer. For this purpose, the excited (E) state can be constructed by $|\Psi_E\rangle = c_1|\psi_{A^*}\rangle|\psi_D\rangle + c_2|\psi_A\rangle|\psi_{D^*}\rangle$ where $|\psi_{A^*}\rangle, |\psi_{D^*}\rangle$ are the excited state wavefunctions of the acceptor and donor, respectively and c_1, c_2 are coefficients

to be determined. The solution of the Schrödinger equation provides the wavefunctions and the related energies of the dimer:

$$\left|\Psi_E^{1,2}\right\rangle = \frac{1}{\sqrt{2}}\left[\left|\psi_{A^*}\right\rangle\left|\psi_D\right\rangle \pm \left|\psi_A\right\rangle\left|\psi_{D^*}\right\rangle\right]$$
$$E_E^{1,2} = E_{A^*} + E_D + \left\langle\psi_{A^*}\psi_D\left|\hat{V}_{DA}\right|\psi_{A^*}\psi_D\right\rangle \pm \left\langle\psi_{A^*}\psi_D\left|\hat{V}_{DA}\right|\psi_A\psi_{D^*}\right\rangle \quad (5\text{-}5)$$

As it can be seen from (5-5), the excited state of the dimer splits into two states with different energies. The energy of the excited states is given by the sum of the energy of the excited state of the monomer (here it is the excited energy level of the acceptor E_{A^*}), the ground state energy (in this case the donor ground state energy E_D), the Van-der-Waals term $\left\langle\psi_{A^*}\psi_D\left|\hat{V}_{DA}\right|\psi_{A^*}\psi_D\right\rangle$ and the exciton splitting term $\left\langle\psi_{A^*}\psi_D\left|\hat{V}_{DA}\right|\psi_A\psi_{D^*}\right\rangle$. If we take the difference of the Van-der Waals terms in equations (5-4) and (5-5) as ΔD and the difference $E_{A^*} - E_A$ as $\Delta E_{Monomer}$, the transition energy of the dimer molecule can be expressed by calculating $\Delta E_{Dimer} = E_E - E_G$:

$$\Delta E_{Dimer}^{1,2} = \Delta E_{Monomer} + \Delta D \pm \left\langle\psi_{A^*}\psi_D\left|\hat{V}_{DA}\right|\psi_A\psi_{D^*}\right\rangle \quad (5\text{-}6)$$

By analysis of the exciton splitting term in the frame of the Born-Oppenheimer approximation, one finds that the first two terms (V_1,V_2) of the operator $\hat{V}_{DA}$ do not contribute to the matrix element. Instead only the electron-electron repulsion expressed by V_3 (see equation (5-3)) yields a non-zero term which can be further simplified in the point-dipole approximation.[McR64] The exciton splitting then becomes

$$\Delta E_{Dimer}^{1,2} = \Delta E_{Monomer} + \Delta D \pm \left[\frac{\overrightarrow{\mu_D}\cdot\overrightarrow{\mu_A}}{R^3} - \frac{3}{R^5}\left(\vec{R}\cdot\overrightarrow{\mu_D}\right)\left(\vec{R}\cdot\overrightarrow{\mu_A}\right)\right] \quad (5\text{-}7)$$

$\overrightarrow{\mu_A}, \overrightarrow{\mu_B}$ are the transition dipole moments of the D → D* and A → A* transitions and $\vec{R}$ is the position vector of the donor dipole referred to the acceptor dipole as origin. As the acceptor and donor molecule are identical in case of the dimer, the exciton splitting term can be reduced to:

$$\Delta E_{Dimer}^{1,2} = \Delta E_{Monomer} + \Delta D \pm \frac{\left|\overrightarrow{\mu}\right|^2}{R^3}\left(\cos\varphi - 3\cos^2\theta\right) \quad (5\text{-}8)$$

In this case, $\vec{\mu}$ is the transition dipole moment for the singlet-singlet transition of the monomer, the angle φ denotes the non-planarity of the transition dipoles and θ refers to the incline between the transition dipoles. Figure 11 depicts the energy levels of the dimer for

specific geometrical orientations between co-planar ($\varphi = 0$) orientated transition dipole moments. Under this cirumstance, allowed transitions are given for a parallel orientation ($\theta = 90^0$), head-to-tail alignment ($\theta = 0^0$) and oblique orientations (all θ but not 0^0, 90^0 or $54{,}7^0$!).

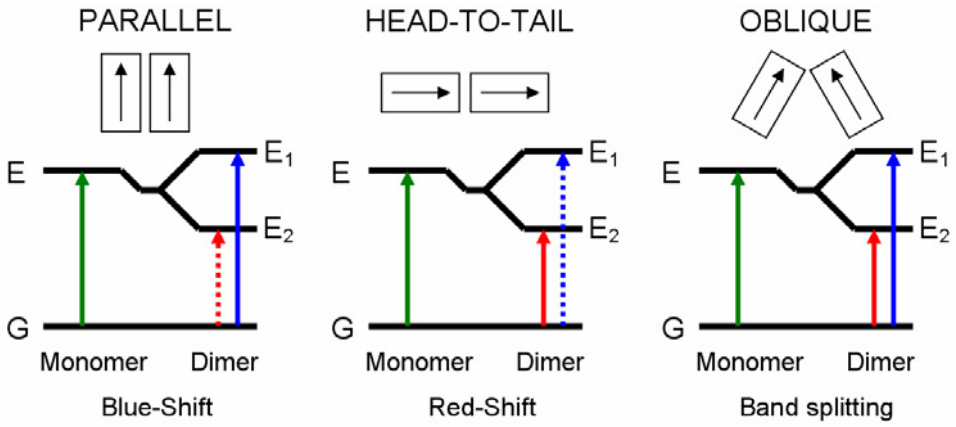

Figure 11. Scheme of the exciton band structure in molecular dimers with various geometrical arrangements of transition dipole moments. Adapted from [Kas63].

The exciton splitting in the strong-coupling case has two important consequences for the photophysical properties of the dimer. The first one is obvious from Figure 11, namely, that the electronic transition will be hypsochromic or bathochromic shifted with respect to the monomer. The second effect is the enhancement of non-radiative transitions in the dimer accompanied by a quenching of the fluorescence of the dimer.

Looking at the transfer rate for the strongly coupled dimer, it was found that energy transfer occurs much faster ($\sim 10^{14}\ s^{-1}$) in comparison to relaxation processes to the ground state. This means that the excitation energy is located neither at the donor nor on the acceptor site. The exciton state is delocalized over the dimer or phenomenologically spoken; excitation energy is bundled as a free exciton. [Röd99] This is in sharp contrast to the Förster resonance energy transfer mechanism introduced in the following section.

5.1.2 Förster Resonance Energy Transfer (FRET)

A donor chromophore in its excited state can transfer energy by a non-radiative long-range dipole-dipole coupling mechanism to an acceptor chromophore. Förster obtained an expression to describe the rate of this process. [För48] The derivation of the important equations is briefly shown below. [Lin71][Lin93][Spe96]

The electronic energy transfer (EET) rate is that of the transition from the initial (i) state

D* + A described by the two-electron wavefunction Ψ^i to the final (f) state D + A* described by Ψ^f:

$$\Psi^i = \frac{1}{\sqrt{2}}\left[\Psi_{D^*}(1)\Psi_A(2) - \Psi_{D^*}(2)\Psi_A(1)\right]$$
$$\Psi^f = \frac{1}{\sqrt{2}}\left[\Psi_D(1)\Psi_{A^*}(2) - \Psi_D(2)\Psi_{A^*}(1)\right] \quad (5\text{-}9)$$

According to the Born-Oppenheimer Approximation, the molecular wavefunction Ψ is given by the product of the nuclear Φ and electronic wavefunction χ. The interaction matrix element V_{EET} expressing the coupling between initial and final state is given by

$$V_{EET} = \left\langle \Psi^i \middle| V \middle| \Psi^f \right\rangle \quad V = \frac{e^2}{\varepsilon \cdot r} \quad (5\text{-}10)$$

V is the perturbation part of the total Hamiltonian of the system and reflects the repulsion between the two electrons involved in the energy transfer. ε is the dielectric constant of the medium and r is the distance between the electrons. The interaction matrix element V_{EET} is the sum of two terms, namely the Couloumb interaction and the exchange interaction. Energy transfer via the exchange mechanism or so-called Dexter mechanism is only efficient for short distances (~0.5-1nm) between D and A, therefore is not further considered. The Coulombic term can be approximated by expanding it in series and maintaining only the dipole-dipole term in the expansion thus obtaining

$$V_{EET} = \frac{1}{\varepsilon \cdot R^3}\left[\overrightarrow{\mu_D} \cdot \overrightarrow{\mu_A} - \frac{3}{R^2}\left(\vec{R} \cdot \overrightarrow{\mu_D}\right)\left(\vec{R} \cdot \overrightarrow{\mu_A}\right)\right] \cdot \prod_j \left\langle \chi_j^i \middle| \chi_j^f \right\rangle \quad (5\text{-}11)$$

μ_D and μ_A are the transition dipole moments of the D → D* and A → A* transitions. Equation (5-11) can be rewritten by introduction of an orientational factor k:

$$V_{EET} = \frac{\overrightarrow{\mu_D} \cdot \overrightarrow{\mu_A}}{\varepsilon \cdot R^3} \cdot k \cdot \prod_j \left\langle \chi_j^i \middle| \chi_j^f \right\rangle \quad k = 2\cos\theta_D \cos\theta_A - \sin\theta_D \sin\theta_A \cos(\varphi_A - \varphi_B) \quad (5\text{-}12)$$

The relative orientation of the interacting transition dipole moments controls the strength of the interaction. (See Figure 12 for a graphical representation of the geometrical arrangement of the dipole-dipole interaction) In a situation where they are aligned perpendicular, for example $\theta_D = 90^0$, $\theta_A = 0^0$, the orientational factor is zero as well as the coupling matrix element. In this situation, Förster energy transfer is not to be expected.

By using Fermis Golden rule, the EET rate constant can be written as

$$k_{EET} = \frac{2\pi}{\hbar} \cdot \sum_i \sum_f P^i \cdot V_{EET}^2 \cdot \delta\left(E^i - E^f\right) \quad (5\text{-}13)$$

where P^i is the distribution of the initial state and E^i, E^f are the energies of the initial and final states, respectively. Substituting equation (5-12) into equation (5-13), we find:

$$k_{EET} = \frac{2\pi}{\hbar} \cdot \left(\frac{\overrightarrow{\mu_D} \cdot \overrightarrow{\mu_A}}{\varepsilon \cdot R^3} \cdot k \right)^2 \cdot \sum_{\nu} \sum_{\eta} P_{\nu}^{i} \cdot \left(\prod_{j} \left| \left\langle \chi_{j,\nu}^{i} \middle| \chi_{j,\eta}^{f} \right\rangle \right| \right)^2 \delta\left(E_{\nu}^{i} - E_{\eta}^{f} \right) \tag{5-14}$$

The population of the vibrational states of the excited donor and the ground state acceptor (initial state) are determined by the Boltzmann distribution P_{ν}^{i}.

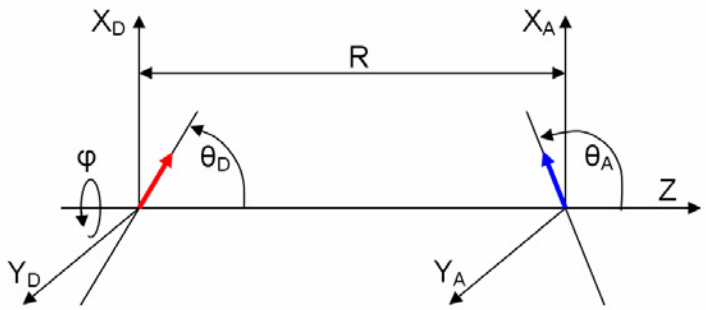

Figure 12. Geometrical configuration of dipole-dipole interaction between donor and acceptor molecules.

The next step is very important, since measurable spectroscopic quantities are introduced in equation (5-14). Using the expression for the absorption coefficient,

$$\varepsilon_A(\omega) = \frac{4\pi^2 \omega}{3\hbar c a''} \sum_{\nu} \sum_{\eta} P_{\nu}^{Ai} \left| \left\langle \chi_{\eta}^{Af} \middle| \overrightarrow{\mu_A} \middle| \chi_{\nu}^{Ai} \right\rangle \right|^2 \delta\left(\omega_{\eta,\nu}^{A} - \omega \right) \tag{5-15}$$

the normalized spectral emission distribution given by equation (5-16),

$$\overline{F_D}(\omega) = \frac{4\omega^3 a' \tau_D}{3c^3} \sum_{\nu} \sum_{\eta} P_{\nu}^{Di} \left| \left\langle \chi_{\eta}^{f} \middle| \overrightarrow{\mu_A} \middle| \chi_{\nu}^{i} \right\rangle \right|^2 \delta\left(\omega - \omega_{\eta,\nu}^{D} \right) \tag{5-16}$$

the integral representation of the δ function and carrying the integration over t, we finally obtain the Förster expression for dipole-dipole induced EET rate constant:

$$k_{EET} = \frac{9000 \cdot \ln 10 \cdot k^2 \cdot \Phi_D}{128 \cdot \pi^5 \cdot n^4 \cdot N_A \cdot \tau_D \cdot R^6} \int_0^{\infty} \frac{\overline{F_D}(\bar{\nu}) \cdot \varepsilon_A(\bar{\nu})}{\bar{\nu}^4} d\bar{\nu} \tag{5-17}$$

n is the refractive index of the medium, Φ_D and τ_D are the donor fluorescence quantum yield and its lifetime in the absence of acceptor molecules, $F_D(\nu)$ is the normalized donor fluorescence spectrum, $\varepsilon_A(\nu)$ is the acceptor's absorption spectrum expressed by its extinction coefficient and N_A is Avogadro number. Equation (5-17) shows that energy transfer of Förster type requires an overlap between the donor fluorescence spectrum and the acceptor's

absorption spectrum. Typically, equation (5-18) is given in terms of the Förster radius R_0:

$$k_{EET} = \frac{1}{\tau_D}\left(\frac{R_0}{R}\right)^6 \qquad R_0 = \sqrt[6]{\frac{9000 \cdot \ln 10 \cdot k^2 \cdot \Phi_D}{128 \cdot \pi^5 \cdot n^4 \cdot N_A} \cdot \int \frac{\overline{F_D}(\bar{\nu})\varepsilon_A(\bar{\nu})}{\bar{\nu}^4} d\bar{\nu}} \tag{5-18}$$

The Förster radius is the distance between donor and acceptor at which the energy transfer process has a probability of 50% with respect to all other processes depopulating the donor's excited state. For aromatic compounds R_0 ranges typically between 10 Å and 100 Å. [Spe96] For a random distribution of dipole moments, e.g. for separate dye molecules in solution, the orientational factor is given by $k^2 = 2/3$. [Spe96]

5.2 Electron Transfer Processes

The discussion will be limited to photoinduced electron transfer processes in solutions, in which after light excitation of a donor (D) an electron is transferred from the donor to an electron accepting species (A). Electron transfer can be regarded as a multi-step process:

$$D + A \xrightarrow{h\nu} D^* + A \xrightarrow{Encounter} [D^* + A] \xrightarrow{ET} [D^+ + A^-] \xrightarrow{Separation} D^+ + A^- \tag{5-19}$$

Following excitation of the donor, the formation of an encounter complex [D^* + A] between excited donor and acceptor is required which may occur by diffusion or is achieved by covalent attachment of D and A. After electron transfer (ET) took place, an ion-pair [$D^+ + A^-$] is created, also known as a charge-transfer intermediate. [Kav93] In this state, the ions are attracted by Coulomb's force and may further separate through rearrangement of solvent molecules, yielding two stabilized free ions. Quenching of the photoexcited donor state by ET competes with other deactivation processes, e.g. radiative transitions or internal conversion. Whether ET is the favourable quenching process or not can be estimated from the associated thermodynamic driving force, namely, the Gibs free energy change.

5.2.1 Rehm-Weller Equation

The calculation of the Gibs free energy change ΔG^0 for an electron transfer between donor and acceptor allows estimating if the reaction will proceed exergonic ($\Delta G^0 < 0$) or endergonic ($\Delta G^0 > 0$). In case of an exergonic reaction, electron transfer occurs spontaneously but no information is provided about the expected transfer rate, hence the word spontaneously is often misleading.

The free energy change for a one electron transfer process can be calculated using the Rehm-Weller-equation:

$$\Delta G^0 = e \cdot \left[E_{1/2}^{ox}(D/D^+) - E_{1/2}^{red}(A/A^-) \right] - \Delta E^* - \frac{e^2}{4\pi\varepsilon_0 \varepsilon_s R} \tag{5-20}$$

The first term in parentheses multiplied by the charge of an electron refers to the difference between the energy required for oxidation of the donor ($D \rightarrow D^+ + e^-$ or D/D^+) and the energy released by reduction of the acceptor ($A + e^- \rightarrow A^-$ or A/A^-). The subscript 1/2 of the associated potentials $E_{1/2}^{ox}(D/D^+)$ and $E_{1/2}^{red}(A/A^-)$ indicate that these values are defined as half-wave, a necessary convention coming from the way these potentials are measured by cyclic voltametry. The second term ΔE^* is the energy supplied to the thermodynamic system by photoexcitation of the donor and corresponds to the difference between the energy of first excited state (S_1 or T_1) and the ground state of the donor. The latter presumes that electron transfer always takes place from the equilibrated lowest excited state. When the ion pair is formed, attractive Coloumb forces will draw the two ions closer together up to the contact distance R. This process is related with the release of energy represented by the last term in equation (5-20).

The solvent has an important influence on oxidation and reduction potentials but this dependency is not parameterized in equation (5-20). The Born equation provides correction terms for a transfer of ions from reference solvent with the dielectric constant ε_{ref}, where the potentials have been measured in, to the solvent (ε_s) used in the experiment:

$$\begin{aligned} e \cdot E_{1/2}^{ox}(D/D^+) &= e \cdot E_{1/2}^{ox}(D/D^+)^{ref} - \frac{e^2}{8\pi\varepsilon_0 r_{D+}} \left(\frac{1}{\varepsilon_{ref}} - \frac{1}{\varepsilon_s} \right) \\ e \cdot E_{1/2}^{red}(A/A^-) &= e \cdot E_{1/2}^{red}(A/A^-)^{ref} + \frac{e^2}{8\pi\varepsilon_0 r_{A-}} \left(\frac{1}{\varepsilon_{ref}} - \frac{1}{\varepsilon_s} \right) \end{aligned} \tag{5-21}$$

r_{D+} and r_{A-} are the radii of the donor cation and the acceptor anion. By substituting equation (5-21) in (5-20) we obtain the solvent dependence of the Rehm-Weller-equation:

$$\begin{aligned} \Delta G^0 = {} & e \cdot \left[E_{1/2}^{ox}(D/D^+) - E_{1/2}^{red}(A/A^-) \right] - \Delta E^* \\ & - \frac{e^2}{4\pi\varepsilon_0\varepsilon_s R} - \frac{e^2}{8\pi\varepsilon_0} \left[\frac{1}{r_{d+}} + \frac{1}{r_{a-}} \right] \left[\frac{1}{\varepsilon_{ref}} - \frac{1}{\varepsilon_s} \right] \end{aligned} \tag{5-22}$$

Under polar conditions, where ε_s is large, ΔG^0 is lower compared to the situation in unpolar solvents. Therefore, electron transfer is mostly favoured in polar solvents. The reason is that when ions are formed from neutral reactants, polar solvent molecules rapidly surround each ion and screen the electrostatic interactions between the oppositely charged ions.

5.2.2 Marcus Theory

Marcus theory allows estimating the photoinduced electron transfer rate k_{ET} for a given donor- acceptor pair in solution. In the following, derivation of the important equations is drafted in combination with the main underlying ideas.

Thermodynamic calculations based on the abovementioned Rehm-Weller-equation suggested a favourable electron transfer for many donor-acceptor systems but experiments showed that charge-separation proceeded quite slowly. It was found that the presence of a kinetic barrier characterized by a free energy of activation ΔG_{el} is responsible for this behaviour. A straight forward approach was therefore, to formulate the dependence of k_{ET} on ΔG_{el} basing on the Arrhenius law and additionally introduce suitable preexponential factors:

$$k_{ET} = \nu_n \cdot \kappa_{el} \cdot \exp\left[-\frac{\Delta G_{el}}{k_B T}\right] \tag{5-23}$$

ν_n is the nuclear frequency and refers to the vibrational motion of encounter complex. [Mar85] With higher frequency, the probability to overcome the activation barrier increases. The electronic factor k_{el} refers to the overlap between the initial reactant state [D^*-A] and final product state [$D^+ + A^-$] and therefore cover the quantum-mechanical aspects of electron transfer.

If D and A approach close enough during the encounter complex, there is sufficient overlap between reactant and product state to ensure a transition to the charge-separated state. In this situation, the electronic factor is in the range of $k_{el} \cong 1$. The so-called adiabatic electron transfer can be treated by classical Marucs theory. In this model, the reactant state [D^*-A] and product state [$D^+ + A^-$] are approximated by harmonic enthalpy energy curves along a generalized reaction coordinate as depicted in Figure 13. The point where reactant and product state intersect corresponds to the activation energy ΔG_{el}. Due to the significant overlap of their wavefunctions, the potential enthalpy curves merge at the transition point. An electron transfer process starts with the excitation into the Frank-Condon State (vibrationally excited state) of the reactant [D^*-A]. This state undergoes rapidly equilibration to the lowest vibrational level. This step is followed by a gain of energy from thermal collisions with surrounding molecules until the activation barrier is reached. [Kav93] After charge separation took place, the product state relaxes to the lowest vibrational level. This process involves a rearrangement of the nuclei and a reorientation of solvent molecules.

For estimation of k_{ET} from equation (5-23), a relationship between the activation energy ΔG_{el}

and the free energy change ΔG^0 as a known quantity from Rehm-Weller equation, is desired. By geometrical considerations of potential energy curves shown in Figure 13, Marcus and Hush were able to obtain this relation:

$$\Delta G_{el} = \frac{(\Delta G^0 + \lambda)^2}{4\lambda} \tag{5-24}$$

The total reorganisation energy λ is the energy required to distort the product state and its surroundings to reach the equilibrium configuration of the reactant state. (See Figure 13).

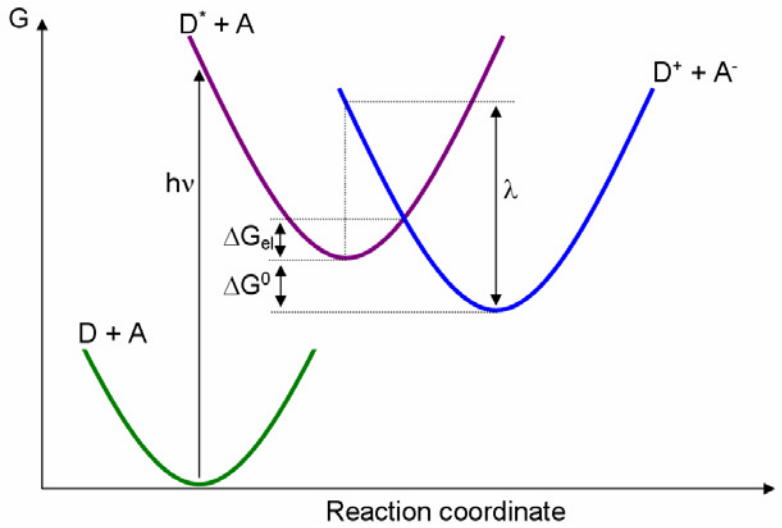

Figure 13. Potential energy curves of initial donor-acceptor pair (D + A), encounter reactant complex (D^* + A) and charge separated product state ($D^+ + A^-$).

It is the sum of the internal reorganisation energy λ_i associated with changes in bond lengths between reactant and product state, and the solvent reorganisation energy λ_s which refers to the effects of orientational changes of solvent molecules surrounding the reactant. For estimation of the total reorganisation energy, the Born-Hush approach can be used:

$$\lambda = \lambda_i + \lambda_s = \lambda_i + \frac{e^2}{4\pi\varepsilon_0}\left[\frac{1}{n^2} - \frac{1}{\varepsilon_S}\right]\left[\frac{1}{2r_{a-}} + \frac{1}{2r_{d+}} - \frac{1}{R}\right] \tag{5-25}$$

n is the refractive index of the solvent, ε_s is the dielectric constant of the solvent, r_{a-} and r_{d+} are the radii of the acceptor anion and donor cation. R refers to the separation distance between donor and acceptor. With $k_{el} \cong 1$ and substitution of equation (5-24) into equation (5-23), the electron transfer rate for adiabatic ET processes equals to:

$$k_{ET} = \nu_n \cdot \exp\left[-\frac{(\Delta G^0 + \lambda)^2}{4\lambda k_B T}\right] \tag{5-26}$$

The nuclear frequency may range from ~10^{12} to $10^{14}s^{-1}$ and is an upper limit for the transfer rate under adiabatic conditions.

In case that donor and acceptor are well separated, the orbital overlap is really low (k_{el} « 1) and electron transfer is classified as non-adiabatic. It then occurs by a tunnelling process which can be treated only by quantum mechanics. The electron transfer rate can be calculated by Fermi's Golden Rule.

$$k_{ET} = \frac{2\pi}{\hbar} \cdot |V|^2 \cdot FCWD \tag{5-27}$$

V describes the electronic matrix element describing the electronic coupling of the reactant's electronic state with the product's electronic state. FCWD is the Frank-Condon weighted density of vibronic states: It is the sum of products of overlap integrals of the vibrational and solvational wavefunctions of the reactants with those of the products. By a treating the reactant and product states quantum-mechanically as harmonic oscillators and consider the motion of the solvent classically, Marcus was able to obtain the electron transfer rate on the basis of equation (5-27) for non-adiabatic ET processes in a semiclassical way. [Mar84]

$$k_{ET} = \left(\frac{4\pi^3}{h^2 \lambda k_B T} \right)^{1/2} \cdot V^2 \cdot \exp\left[-\frac{(\Delta G^0 + \lambda)^2}{4\lambda k_B T} \right] \tag{5-28}$$

Reactions are non-adiabatic if the coupling matrix element V is smaller than k_BT (approximately ~200cm^{-1} at room temperature). V diminishes with distance and can be approximated by: [De98]

$$V^2 = V_0^{\,2} \exp(-\beta(R - r_{a-} - r_{d+})) \tag{5-29}$$

where V_0 is the coupling matrix element at contact and ß is constant, scaling the distance dependence. Equation (5-29) reproduces the exponential dependency of the rate constant which is typical for tunneling processes through a barrier.

Whether adiabatic or non-adiabatic electron transfer, three different regions exist in Marcus theory. Barrierless electron transfer can occur if ΔG^0 equal λ, this is called the optimal region. In case that $\lambda > -\Delta G^0$, the ET rate increases with larger thermodynamic driving force. Instead, in the inverted region ($\lambda > -\Delta G^0$), this behaviour is reversed.

6 Hexapyropheophorbide a-fullerene [C_{60}] molecules as part of modular carrier systems

6.1 Introduction

Dendrimers are repeatedly branched molecules, with many end groups emanating from one central core. [Smi05] In contrast to conventional polymers, dendrimers are prepared by a stepwise procedure, leading to a highly regular branching pattern, well-defined architecture, and a unique molecular weight (MW). They can contain a strictly controlled number of functional groups for the attachment of drugs and also host molecules in inner cavities and deep ditches caused by their multi-branched structure. This design has been proven to be of superior significance for the development of drug delivery systems for PDT and in medicine generally. Another very interesting application of dendrimers is the construction of artificial light harvesting antenna systems. [Dic05]

The photophysical investigations of hexapyropheophorbide a- fullerene [C_{60}] molecules (**P6**, **FHP6**, **FP6**) presented throughout this chapter are a continuation of recent studies in the group of Prof. Röder on more basic molecular architectures (P1, P2, FHP1, FP1) covering both directions of research, namely the development of suitable delivery systems for PDT and artificial complexes mimicking the energy conversion in photosynthesis. [Erm04a, Erm04b, Oma04]

The macromolecules under study, in which six pyropheophorbide a chromophores are covalently linked by a Newkome dendrimer and further coupled to a C_{60} fullerene (See Figure 14), represent a major step towards the realization of a modular carrier system for PDT as it was introduced in section 2.5.2. It is known that the C_{60} fullerene can be used as a versatile building block for the construction of globular dendrimers. [Hac05, Röd06a, Ran05a] This concept is established within the hexakis (pyropheophorbide a)-fullerene [5:1] hexaadduct (**FHP6)** and the hexakis (pyropheophorbidea)-C_{60} **(FP6)** molecule where C_{60} serves as a central construction core. C_{60} is linked to the dendritic polymer and allows coupling of a targeting unit additionally, for example an antibody. This may also increase the water insolubility of these compounds. The employed first generation Newkome dendrimer allowed increasing the number of attached photosensitizing molecules compared to its previously investigated precursor FHP1 (monofullerene hexaadduct-*bis*pyropheo) by a factor of three. **FHP6** differs structurally from **FP6** by the addition of five diethyl malonate addends in the remaining octahedral positions of the fullerene. (See Figure 14) As an important consequence,

the conjugation of the π-electron system of fullerene is broken up and the well-known electron accepting ability of C_{60} is strongly reduced. [Bou95] It was shown that in recently studied monofullerene–*bis*pyropheo (FP1) the electron-accepting fullerene core strongly affects the photoactivity of the pyropheophorbide a (pyropheo) moieties resulting in a strong reduction of the singlet oxygen quantum yield compared to the values obtained for the reference compound *bis*pyropheo (P2). [Erm04a] Since a low singlet oxygen quantum yield limits effective PDT, compound **FHP6** containing the substituted fullerene was envisaged as a potential compound for PDT. Interestingly, it was found that in **FHP6** the fluorescence as well as singlet oxygen quantum yields were quenched compared to those values of FHP1. These results were explained by applying the phenomenological model of energy traps and efficient delivery of excitation to them via Förster energy transfer. [Erm05]

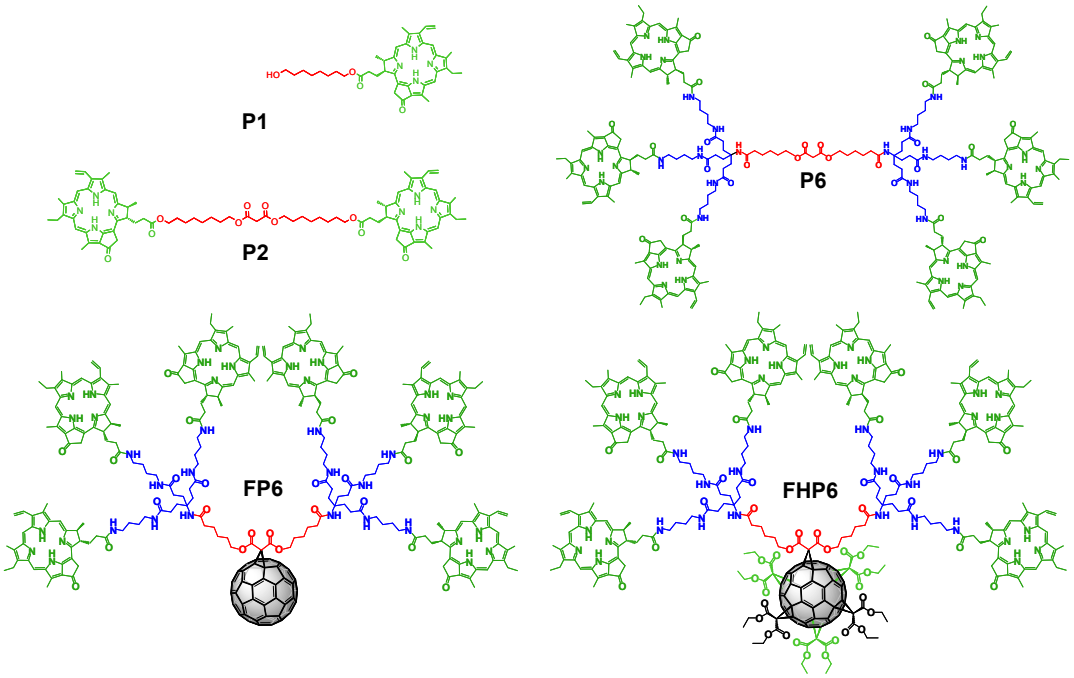

Figure 14. Structural formulas of **FHP6**, **P6** and **FP6** and reference compounds **P1** and **P2**.

Due to the capability of the unsubstituted C_{60} to act as an excellent electron acceptor within the **FP6** molecule, an electron transfer (ET) from the photoexcited pyropheophorbide a chromophores to the fullerene is expected similar to the ET process observed for FP1, consisting of a fullerene with two attached pyropheo molecules. [Erm04b, Oma04] Hexapyropheophorbide a (**P6**), as shown in Figure 14, allowed studying the photoinduced transfer and deactivation processes without the influence of the fullerene core.

The presented work is a comparative investigation of the hexapyropheophorbide series, one without fullerene (**P6**) and two with an electron accepting (**FP6**) and completely substituted

(**FHP6**) fullerene core. It is expected that the deactivation pathways of the excited states of the pyropheo chromophores are different in **P6**, **FHP6** and **FP6** molecular systems. The influence of the fullerene core on the relative efficiency of photoinduced transfer processes is also investigated. Furthermore the *in vitro* phototoxicity generated by **FHP6** and **P6** is reviewed in order to evaluate the potential of these compounds for photodynamic therapy.

The pyropheophorbide a (pyropheo) moieties are attached to the multiplying dendron by octyl spacer chains which modify the photophysical properties of pyropheo. Accordingly, the compounds pyropheo-8-hydroxyoctylester (P1) and bis (8-hydroxyoctyl) malonate-bis-pheophorbide-a-ester (P2), as depicted in Figure 14, are more reliable for the purpose of comparison with photophysical data of the hexapyropheo compounds. Important properties of P1 dissolved in DMF were published previously, the fluorescence lifetime, intersystem crossing quantum yield and singlet oxygen quantum yield have values of 7ns, 0.55 and 0.5, respectively. The fluorescence lifetime and singlet oxygen quantum yield of P2 was reported to 5.7ns and 0.43. [Erm04a,Erm04b]

6.2 Photophysical parameters of FHP6, P6, FP6

In this section the fundamental photophysical parameters concerning **FHP6**, **P6** and **FP6** are presented. These were determined by steady state absorption, fluorescence and singlet oxygen luminescence spectroscopy as well as time resolved fluorescence spectroscopy employing time correlated single photon counting (TCSPC) and transient absorption spectroscopy (TAS). All measurements were performed in DMF.

6.2.1 Steady state absorption spectra

The absorption spectra of **FHP6, P6**, **FP6** and of the reference compounds **P1** and **P2** in DMF are shown in Figure 15. The shape of the absorption spectrum is similar to that of metal free tetrapyrroles consisting of the Soret band located at 413 nm and the splitted $Q_{x,y}$-bands. The absorbance of **P2** containing two pyropheo units is nearly twice the absorbance of **P1** over the whole spectral range. For **P6** consisting of six pyropheo chromophores the absorbance does not increase by a factor of six with respect to **P1**. The $Q_y(0,0)$ absorption transition of **P1** has an extinction coefficient of $\varepsilon=4.2\times10^4$ $M^{-1}cm^{-1}$ whereas for **P6** this value is $\varepsilon=19.2\times10^4$ $M^{-1}cm^{-1}$.

As can it be seen from Figure 15, the absorbance of **FHP6** is about six times the value of **P1** over the whole UV/Vis spectral region. For **FP6** the extinction coefficient of the $Q_y(0,0)$ absorption band is $\varepsilon=12.7\times10^4$ $M^{-1}cm^{-1}$ which is lower than the value obtained for **FHP6** and even for **P6**. The fullerene core with high electron accepting capabilities in **FP6** leads to a strong decrease in absorbance of this compound, indicating the strong influence of C_{60} on the ground state properties of the attached pyropheo chromophores.

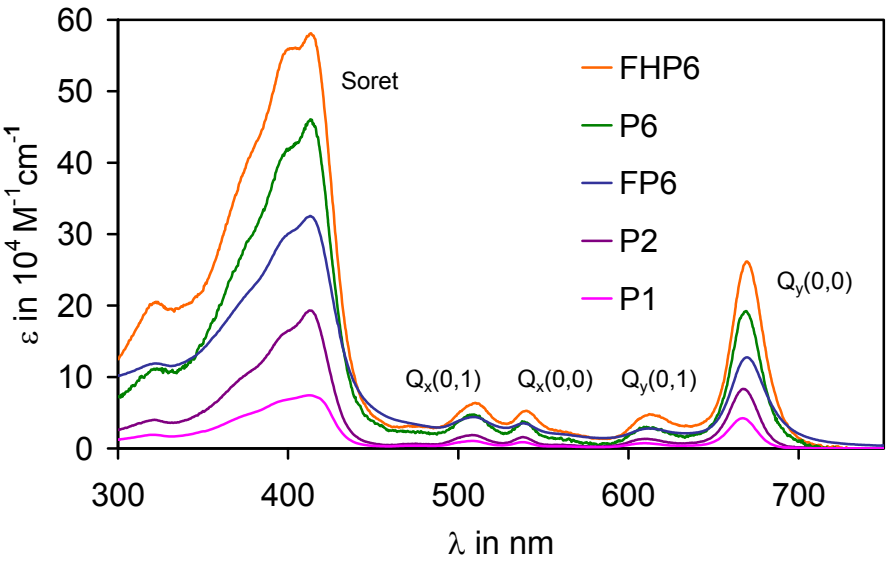

Figure 15. Absorption spectra of **FHP6**, **P6** and **FP6** in DMF. The spectra of **P1** and **P2** are also shown for comparison.

The compounds **FHP6**, **FP6** and **P2**, **P6** show a pronounced splitting of the Soret band in comparison to **P1**. The $Q_y(0,0)$ band of **FHP6**, **P6** and **FP6** is bathochromically shifted compared to **P1** by about 1, 2 and 2.5 nm, respectively.

6.2.2 Steady-state fluorescence

Normalized fluorescence of the investigated compounds and the reference compound spectra are depicted in Figure 16.The samples were excited in the $Q_y(0,0)$ absorption band, the OD was adjusted to 0.2 at this wavelength. The spectra of **FHP6**, **P6** and **FP6** have similar shapes compared to **P2** which shows that the fluorescence emission originates from the pyroPheo units. Furthermore the shape of the fluorescence spectra of **FHP6**, **FP6** and **P6** is broadened compared to **P2**.

The fluorescence intensity of **FHP6** and **P6** is reduced compared to **P2**. By comparison of the integrated intensities, the relative fluorescence quantum yield with respect to **P2** can be

determined. For **FHP6** a value of 42% was obtained and 25% in case of **P6**. For **FP6** a very weak fluorescence emission was detected, the relative fluorescence quantum yield was below 1%. (See Table 2)

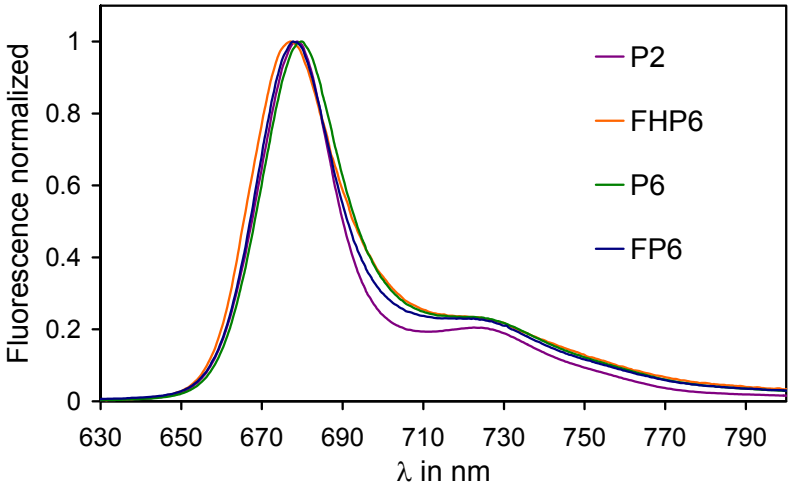

Figure 16. Fluorescence spectra of **FHP6**, **P6**, **FP6** and reference **P2** in DMF.

6.2.3 Time-resolved fluorescence

The fluorescence signal was recorded over time employing the time-correlated single photon counting technique. The samples were excited at 400nm and the fluorescence was detected at 678nm.

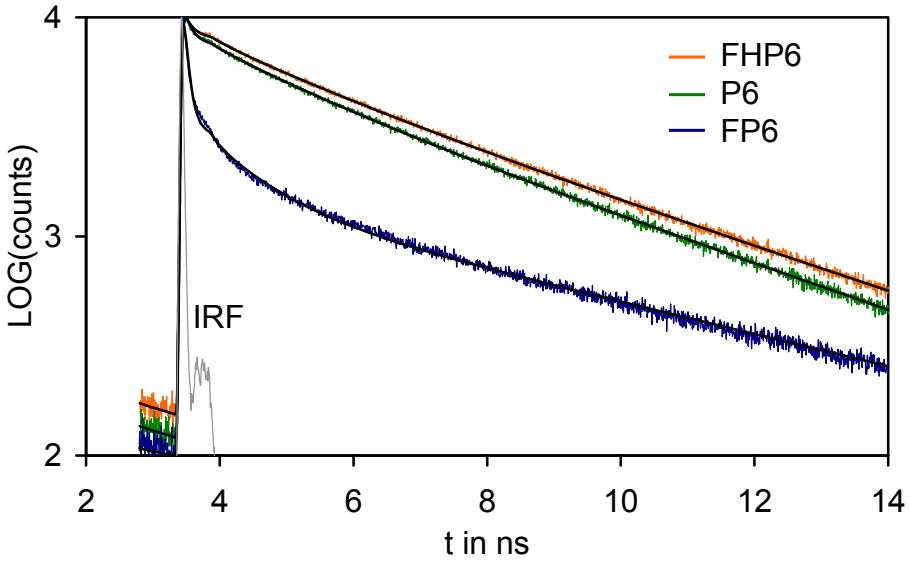

Figure 17. Time resolved fluorescence emission of **FP6**, **P6** and **FHP6** in DMF.

The fluorescence decay of **FHP6**, **P6** and **FP6** shows a complicate character and was fitted in all cases by a four exponential function. (See Figure 17). The fluorescence decay of **FP6** exhibits a fast (τ_q = 110 ps) and dominant quenching process of the S_1-state. The intermediate times were determined to 0.6 ns and 1.7 ns, respectively. The long decay time was every time fixed to a value of τ_{long} = 5.7 ns similar to the decay time of **P2** representing the fluorescence decay of non-interacting pyropheo chromophores.[Erm04a]

The quenching rate k_q in case of **FP6** is given by $k_q = \frac{1}{\tau_q} - \frac{1}{\tau_{long}} = 8.9 \times 10^9 s^{-1}$. For **FHP6** and **P6** the short component was measured to be 0.17 ns and 0.16 ns, respectively. The two intermediate decay components had nearly similar values (about 0.8 ns and 3.5 ns) for **FHP6** and **P6** compounds. It should be mentioned, that all fluorescence decay times estimated for **P6** are slightly shorter compared to **FHP6**. The long decay component had the lowest amplitude (below 10%) for all three compounds under investigation.

6.2.4 Steady-state singlet oxygen generation

Photosensitized steady-state singlet oxygen luminescence was measured to determine the singlet oxygen quantum yield of **FHP6**, **P6** and **FP6** in DMF.

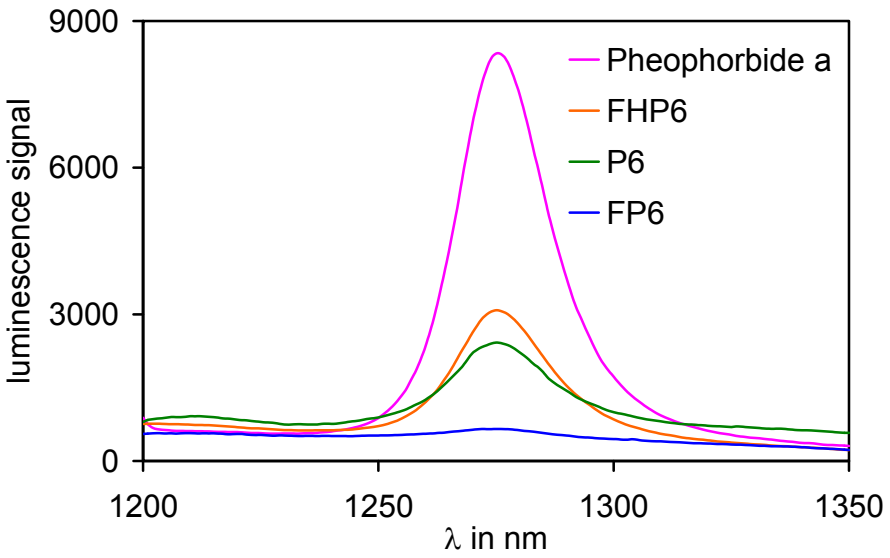

Figure 18. Steady-state singlet oxygen emission photosensitized by **FHP6**, **P6** and **FP6** in DMF. Pheophorbide a in DMF served as a reference.

The spectrally resolved 1270nm singlet oxygen emission is shown in Figure 18. The singlet oxygen quantum yield was determined by comparison of the integrated line intensity of unknown compounds to the integrated line intensity obtained from a reference photosensitizer. For this purpose pheophorbide *a* in DMF was used. It generates singlet oxygen with a quantum yield of $\Phi_\Delta = 0.52$. [Spi98].

The singlet oxygen quantum yields of **FHP6**, **P6** and **FP6** were calculated from equation (4-5) and gave values of 0.22, 0.15 and 0.02, respectively. These are significantly lower than the values reported for P1 and P2 of 0.5 and 0.43 in that order. [Erm04a] The reduction of the singlet oxygen quantum yield might be a consequence of a reduced intersystem crossing quantum yield according to equation (2-6). In the following the results of transient absorption spectroscopy answer this question and provide further insights about the photophysical processes within these molecules.

6.2.5 Transient Absorption Spectroscopy

Transient absorption spectroscopy (TAS) was performed to follow population dynamics of the first excited singlet states and the ground state of **FHP6**, **P6** and **FP6**. The TAS measurement provided a set of transient absorption spectra $\Delta OD(\lambda, \Delta t)$ showing the differences in absorption before and after excitation of the sample at different delay times, Δt. Figure 19 shows the transient absorption spectra of **FHP6**, **P6** and **FP6** at a delay time of 50 ps after excitation. For comparison the ground state absorption spectrum and the fluorescence spectrum of **FHP6** are given at the bottom of Figure 19.

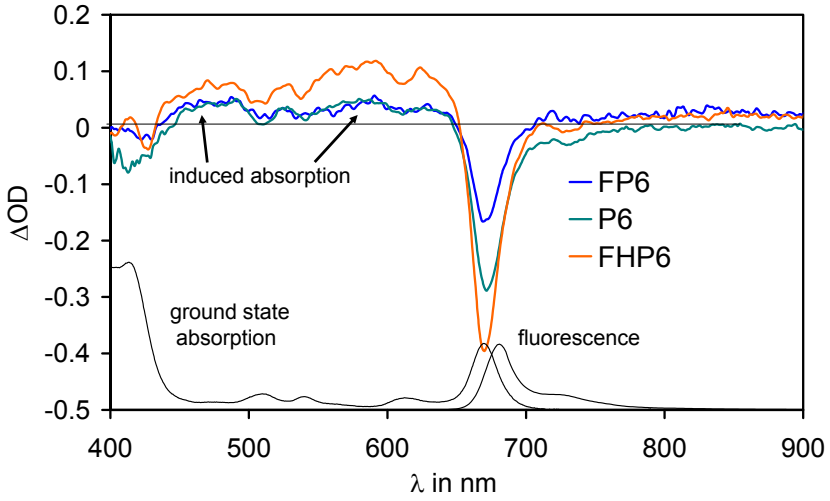

Figure 19. Transient absorption spectra of **FHP6**, **P6** and **FP6** in DMF measured at delay time 50ps.

A strong bleaching is observed at the S_0-S_1 transition of pyropheo around 673 nm caused by the light-induced depletion of the ground state of the molecules. Due to the small Stokes shift, the fluorescence emission of pyropheo partly superimposes the bleaching observed in the region of the S_0-S_1 transition.

Between 500 nm and 630 nm the light-induced excited state absorption (S_1-S_n) of pyropheo causes an increase of the ΔOD signal whereas in the region around 480 nm the T_1-T_n induced absorption of the chromophores results in a positive ΔOD signal. [Zeu01] The fullerene in **FHP6** and **FP6** has more than 30 times lower ground-state extinction coefficient at the excitation wavelength positioned at the $Q_x(0,1)$ band of the pyropheo molecules (515 nm), thus mainly pyropheo was excited during the TAS measurements.[Oma04]

Using the compensation method [Rüc97] the change in the ground state population $\Delta S_0(t)$ and decay of the first excited singlet state population $S_1(t)$ can be determined from the ΔOD spectra in the region from 600 nm to 800 nm in which the S_0-S_1 transition and the fluorescence emission are partly overlapping.

The decay of the first excited singlet state $S_1(t)$ of **FHP6**, **P6** and **FP6** was fitted by a three exponential function. (See Figure 20) For **FHP6**, **P6** and **FP6** the fast decay component of the S_1-state depopulation was measured to 49 ps, 30 ps and 24 ps, respectively (see Table 2). These short times could not be resolved by TCSPC and represent an additional process. The intermediate decay times confirm the results of TCSPC measurements.

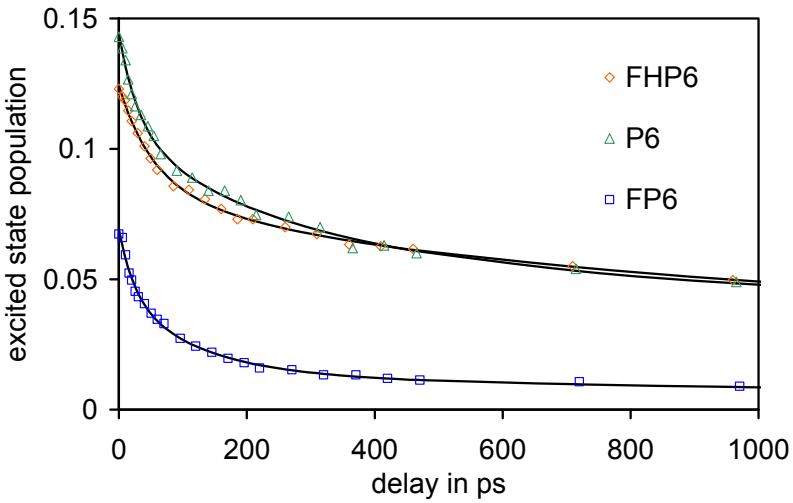

Figure 20. Excited state population of **FHP6**, **P6** and **FP6** as determined by ps-TAS.

For **FP6** the dominant deactivation process was determined to 120 ps which is in a good agreement to the value obtained from time-resolved fluorescence measurements. The long

decay components measured by TAS have values of 2.8, 3.6 and 2.3 ns for **FHP6**, **P6** and **FP6** respectively. This component is an average value of the decay times in the nanosecond range obtained by TCSPC.

The ground state depletion of **P6**, **FHP6** and **FP6** fitted by three exponential functions is shown in Figure 21. The short components have the same values as the fast decay times determined from transient amplification. The intermediate decay times were determined to 138 ps, 101 ps, 261 ps and the long decay times were fitted to 3.7, 3.1 and 5.2 ns for **FHP6**, **P6** and **FP6**, respectively.

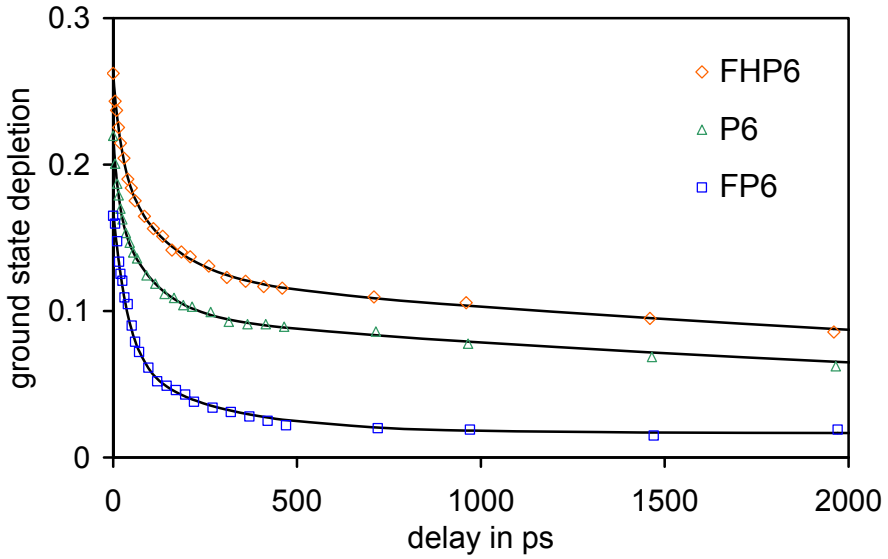

Figure 21. Ground state depletion of **FHP6**, **P6** and **FP6** as measured by ps-TAS.

The intersystem crossing quantum yield (Φ_{ISC}) can be estimated by comparing the depletion of the ground state shortly after excitation (Δt=0 ps) to the value after a long delay time (Δt=15 ns), when the population of the first excited state is negligible. [Rüc97] The intersystem crossing quantum yield of **FP6** was determined to Φ_{ISC}=0.06 which is significantly lower compared to the values for **FHP6** and **P6** (0.24 and 0.16, respectively). [Erm05] These different Φ_{ISC} values support the results obtained by singlet oxygen measurements. The reduction of the singlet oxygen quantum yield is a consequence of the reduced intersystem crossing quantum yield. As an example, **FP6** has a very low singlet oxygen quantum yield (Φ_{Δ}) of only 0.02 because of its strongly reduced ISC quantum yield of 0.06. (see Table 2)

6.2.6 Compilation of photophysical parameters

Table 2 summarizes the photophysical properties of **FHP6**, **P6**, **FP6** in DMF obtained from steady steady and time-resolved spectroscopies in the UV/VIS/NIR range. The longer S_1 lifetime components were determined by time-resolved fluorescence (τ_{Trap3}, τ_{Trap2} ,τ_{Trap1}, τ_q, τ_F) whereas the short process (τ_{Short}) could only be resolved by ps-TAS as aforementioned in section 6.2.5.

Table 2. Important photophysical parameters of FHP6, P6 and FP6 (reference compound P2) in DMF.

sample	**S_1 decay components**			**Φ_{Frel}**	**Φ_{Δ}**	**Φ_{ISC}**
	τ_F [ns]	**Amplitude**	**Assignment**			
P2	5.7		τ_F	1	0.43	0.49
FHP6	0.049	0.27	τ_{Short}	0.42	0.22	0.24
	0.17	0.17	τ_{Trap3}			
	0.9	0.11	τ_{Trap1}			
	3.7	0.39	τ_{Trap2}			
	5.7	0.06	τ_F			
P6	0.030	0.25	τ_{Short}	0.25	0.15	0.16
	0.16	0.32	τ_{Trap3}			
	0.7	0.09	τ_{Trap1}			
	3.3	0.29	τ_{Trap2}			
	5.7	0.05	τ_F			
FP6	0.024	0.35	τ_{Short}	<0.01	0.02	0.06
	0.11	0.47	τ_q			
	0.6	0.08	τ_{Trap1}			
	1.7	0.05	τ_{Trap2}			
	5.7	0.05	τ_F			

The notation of the lifetime components is in anticipation of the detailed analysis of this data

presented in sections 6.4, 6.5 and 6.7. The relative fluorescence quantum yield Φ_{Frel} with respect to P2, the singlet oxygen quantum yield Φ_{Δ} and the intersystem crossing quantum yield Φ_{ISC} were obtained by steady state fluorescence spectroscopy, steady state singlet oxygen luminescence and transient absorption spectroscopy, respectively. For the purpose of a later comparison the photophysical parameters of **P2** are also shown.

6.3 Molecular modeling

Molecular modeling was performed to obtain energetically minimized structures of **FHP6**, **P6** and **FP6** which provided insight about intramolecular interactions and distances among molecular subunits in the optimized conformations. This information supported the interpretation and theoretical analysis of photoinduced energy and electron transfer processes within these molecules presented in the next sections of this chapter.

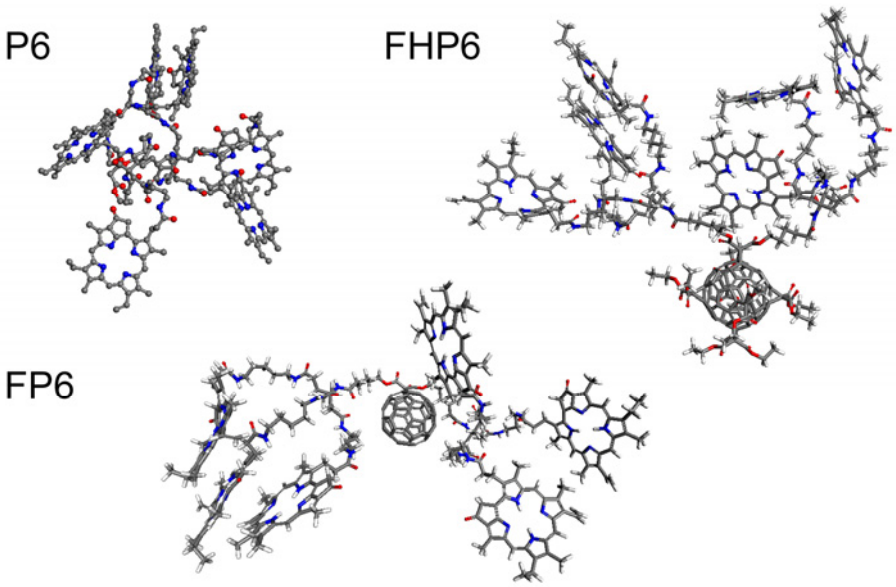

Figure 22. Energy minimized conformations of **FHP6**, **P6** and **FP6** calculated with simulated annealing + geometry optimization.

Geometry optimization of **FHP6**, **P6** and **FP6** was computed in vacuo with Material Studio (MS) 3.2 [MatSt] using the COMPASS (condensed-phase optimized molecular potentials for atomistic simulation studies) forcefield and a combination of gradient and Newton methods encapsulated in the modul Discover of MS. In order to avoid trapping the structure in a conformation that represents a local energy minimum, geometry optimization was performed in combination with simulated annealing (Modul Forcite of MS). The molecules were heated to 700K and then cooled to 300K over a period of 1000fs for up to 500 cyles. During each

cycle the atoms are allowed to move according to their kinetic energy at temperature T. After each annealing cycle geometry optimization was executed to obtain the energetically minimized conformation. The structures with the lowest potential energy were selected for analysis and are shown in Figure 22.

All distances measured among the chromophores and C_{60} refer to center-to-center distances. The possible conformations of **P6**, **FHP6** and **FP6** have one feature in common. The pyropheo units are partly stacked together at intramolecular distances of about (9±1) Å. **P6** tends to fold to a dense coil. A variety of orientations and angles between the planar pyropheo molecules could be identified. The average distance R between adjacent pyropheo units (centre-to-centre) in **P6** was estimated from the corresponding minimized structure to (13±1) Å. The average distance between non-neighboring molecules is approximately (24±2) Å. For **FP6** the situation is completely different. The molecule does not fold as dense as **P6**. The average distance of neighboring molecules is about (13±3) Å but the average distance between non-neighboring units is about (32±7) Å and therefore significantly longer compared to **P6**. It was found that one of the pyropheo units can be located in close proximity to C_{60} at distances of around 12 Å. Such a close approach is hindered in **FHP6** because the malonate units connected to C_{60} act as spacers.

6.4 Photoinduced energy transfer processes in P6, FHP6, FP6

Two different types of energy transfer mechanism have been identified in **FHP6**, **P6** and **FP6** molecules. Förster resonance energy transfer (FRET) allows the long-range radiationless intramolecular hopping of energy from an initially excited pyropheo donor to other pyropheo units within the molecule. The other mechanism is known as excitonic interaction requiring two participating pyropheo units in a close proximity. In this case the excitation energy is delocalized over the whole dimer. [Hel97, Kas65] In the following subsections both types of energy transfer in **FHP6**, **P6** and **FP6** will be discussed basing on the photophysical parameters and molecular modeling results presented in section 6.2 and section 6.3, respectively.

6.4.1 Förster resonance energy transfer in P6, FHP6 and FP6

For a pyropheo-pyropheo FRET a significant overlap between absorption and fluorescence spectrum exists and therefore we assume that FRET may occur between adjacent pyropheo molecules. The theory developed by Förster allows the estimation of the energy transfer rate k_D. [För48]

$$k_D = \frac{1}{\tau_D}\left(\frac{R_0}{R_{DA}}\right)^6 \qquad (6\text{-}1)$$

where R_{DA} is the centre-to-centre distance between donor and acceptor and τ_D is the lifetime of the excited pyropheo donor in the absence of any acceptor molecules. As τ_D we will use the fluorescence lifetime of **P2** in DMF measured to 5.7 ns. [Erm04b] Förster radius R_0 can be estimated from the overlap integral of the absorption ε_A and normalized fluorescence spectrum I_D^n of the pyropheo molecules: [Kle00]

$$R_0[nm] = \sqrt[6]{\frac{8.8\times10^{17}\cdot k^2\cdot\Phi_F}{n^4}\cdot\int\frac{I_D^n(\tilde{\nu})\varepsilon_A(\tilde{\nu})}{\tilde{\nu}^4}d\tilde{\nu}} \qquad (6\text{-}2)$$

The refractive index of DMF is n = 1.43. The average orientation between the interacting dipole moments is not known, therefore we assume for the orientation factor a value of k^2 = 2/3 corresponding to a random distribution of dipole moments. Using these values R_0 was calculated to 56 Å. The average distance of neighboring pyropheo units R_{DA} we assumed to be 13 Å for **P6**. (See section 6.3) The resulting FRET rate is 1.1×10^{12} s^{-1}. This means that the excitation energy remains only one picosecond on the initially excited molecule before hopping to the nearest neighbor. Excitation jump to the more distant non-neighboring units (average R_{DA} = 24 Å) is more than one order of magnitude less probable and the excitation should remain around 35 ps on the pyropheo moiety. For **P6** the short component of the fluorescence lifetime was measured to 30 ps.

In the studied multichromophoric system with different distances and mutual orientations between the pyropheo units, a number of subsequent steps of FRET should occur before the energy is delivered to a trap resulting in the observed average transfer time of 30 ps. As the jump to the nearest neighbor is much faster than any other process we can assume that several FRET jumps take place until the energy is caught by a trap.

For **FHP6** the fast component of the fluorescence lifetime (49 ps) is longer than the value measured for **P6**. This is in agreement with molecular modeling results where the average distances between pyropheo units in **FHP6** are longer compared to **P6**. For **FP6** the fast fluorescence decay component was determined to 24 ps and this value is even shorter compared to that one of **P6**. **FP6** is not folded as dense as **P6** pointing out that a lower number of jumps occur until the dye molecules are deactivated. This may indicate the presence of another trapping process which we assume to be an electron transfer.

6.4.2 Excitonic interactions in P6, FHP6 and FP6

The absorption spectra of **FHP6**, **P6** and **FP6** show a pronounced splitting of the Soret band. Together with the observed reduction of the fluorescence as well as ISC quantum yields compared to these values of reference **P2** compound, this is an indication for excitonic interactions between adjacent pyropheo molecules.[Kas65,Kas50] The formation of pyropheo dimers in **FHP6**, **FP6**, and **P6** has two important consequences.

Firstly the absorption cross section of a dimer is reduced in contrast to the monomer [Eic00], thus the overall absorbance should be decreased if dimer formation takes place. Indeed a significant reduced absorbance of **P6** relative to **FHP6** was observed. This is attributed to the denser folding of the **P6** molecule compared to **FHP6** (See section 6.3), and as result, the probability of a trap formation is higher for **P6**. In **FHP6** the fullerene with added malonate units can be considered as a spacing unit lowering the probability of dimer formation. **FP6** has the lowest absorbance of all compounds carrying six pyropheo chromophores. As a larger spacing between the pyropheo chromophores mediated by the fullerene would lead to an increase of absorbance compared to **P6** another effect induced by C_{60} seems to be more important. The fullerene core in **FP6** with its extended π–electron system is assumed to influence the electronic ground state properties of the attached pyropheo chromophores leading to a significant reduction of the absorbance of this compound.

Second, the pyropheo dimers can act as efficient energy traps. The arrangement of the transition dipole moments of the pyropheo units forming the dimer and the distance between them determine the properties of a trap as it was previously reported. [Hac05, Röd06b] The observation of intermediate fluorescence decay times of τ_{Trap1}=0.7 ns (τ_{Trap2}=3.3 ns) for **P6** and τ_{Trap1}=0.9 ns (τ_{Trap2}=3.7 ns) for **FHP6** are attributed to traps with prevalent face-to-face (oblique) arrangement of the transition dipole moments. The reduced fluorescence lifetime of the dimers is based on enhanced non-radiative transitions. As a consequence the fluorescence intensity of **FHP6** and **P6** is reduced compared to **P2**. The fluorescence quenching of **P6** is stronger than in **FHP6**, supporting the argument that in **FHP6** dimer formation is less probable.

6.5 Photoinduced electron transfer processes in FP6

It was found that for **FP1** photoinduced electron transfer from initially excited pyropheo moiety to the electron accepting C_{60}-fullerene is the dominant process leading to the fast

deactivation of the first excited singlet state of pyropheo with a rate of 1.8×10^9 s^{-1}. [Erm04b] Investigation of **FP6** revealed a strongly reduced fluorescence quantum yield, Φ_{Frel}, of 0.01 relative to **P2**, a low intersystem crossing quantum yield, Φ_{ISC}, of 0.06 and the occurrence of a fast dominant quenching process visible in the time-resolved fluorescence decay. These findings can be attributed to an efficient process deactivating the S_1 state of **FP6**. An energy transfer process to the fullerene is unfavorable because although the first excited singlet state of C_{60} (1.75 eV) [Hal00] is energetically close to the singlet state of pyropheo (1.84 eV), the extinction coefficient of C_{60} monoadduct in the region of the fluorescence band of pyropheo is very low, thus the overlap integral and the Förster radius are very small too.[Sun00] For **FHP6** the reduction of fluorescence (quantum yield 0.42 relative to **P2**) and intersystem crossing quantum yield (Φ_{ISC} =0.24) is not as strong as for **FP6**. As the first electron reduction potential of fullerene hexakisadduct is relatively high, about 0.8 V lower than for the fullerene monoadduct [Bou95], the electron accepting capabilities of the fullerene moiety in **FHP6** are strongly reduced compared to **FP6**.

From a thermodynamic point of view the question of a possible electron transfer for **FP6** between excited pyropheo donor (D) and C_{60} acceptor (A) can be addressed by calculating the free energy change using the Rehm-Weller equation: [Pet06, Reh69, Reh70]

$$\Delta G^0 = e\cdot\left[E_{1/2}^{ox}(D/D^+) - E_{1/2}^{red}(A/A^-)\right] - \Delta E^* - \frac{e^2}{4\pi\varepsilon_0\varepsilon_s R} - \frac{e^2}{8\pi\varepsilon_0}\left[\frac{1}{r_{d+}}+\frac{1}{r_{a-}}\right]\left[\frac{1}{\varepsilon_{ref}}-\frac{1}{\varepsilon_s}\right] \tag{6-3}$$

The half-wave oxidation potential of the pyropheo in DMF is $E_{1/2}^{ox}\left(D/D^+\right)$ = 0.42 V [Osu96]. The first step half-wave reduction potential of a similar fullerene monoadduct ($C_{60}H_2$) dissolved in benzonitrile (PhCN) was reported to be -1.05 eV (versus the ferrocene/ferrocenium cation or Fe/Fc^+). [Gua93] By referencing this value to the saturated calomel electrode (SCE) electrode (+0.40V) [Gag80] and applying a solvent correction (+0.02V for PhCN $\rightarrow$ DMF), we assume a reduction potential of $E_{1/2}^{red}\left(A/A^-\right)$ = -0.63 V for the C_{60} monoadduct in DMF, ΔE^* is the energy difference between first excited singlet and ground states of pyropheo which was derived from the absorption and fluorescence spectra to ΔE^* = 1.84 eV. The effective radii of the fullerene anion is r_{a-} = 4 Å [Chi81] whereas the value of the pyropheo donor cation is r_{d+} = 4.4 Å. The separation distance between donor and acceptor was assumed to be R = 12 Å. The last two values were estimated from molecular modeling. The dielectric constant of DMF is $\varepsilon_s = \varepsilon_{ref}$ = 37. For the free energy change we

calculated a value of ΔG^0 = -0.82 eV. A negative ΔG^0 implies that the electron transfer from photoexcited pyropheo to the fullerene core is an exergonic reaction. The energy of the charge separated state is $E_{CS} = \Delta E^* + \Delta G^0 = 1.02$ eV. This value lies below the energy of the first excited singlet as well as triplet state of pyropheo. When donor and acceptor are spaced by more than ~5 Å, electron transfer can be treated in the nonadiabatic or weak coupling limit. [Ven98] The widely used expression developed by Marcus [Mar85] allows the calculation of the transfer rate k_{ET}:

$$k_{ET} = \left(\frac{4\pi^3}{h^2 \lambda k_B T}\right)^{1/2} \cdot V^2 \cdot \exp\left[-\frac{(\Delta G^0 + \lambda)^2}{4\lambda k_B T}\right] \qquad (6\text{-}4)$$

In the first term h is the Planck constant, $T = 293K$ is the room temperature, k_B is the Boltzmann constant and λ is the reorganization energy, λ is the sum of the intramolecular reorganization energy λ_I and the solvent reorganization energy λ_S. The intramolecular reorganization energy is around 0.3eV [Gou90,Gou91] whereas λ_S can be approximated by

$$\lambda_S = \frac{e^2}{4\pi\varepsilon_0}\left[\frac{1}{n^2} - \frac{1}{\varepsilon_S}\right]\left[\frac{1}{2r_{a-}} + \frac{1}{2r_{d+}} - \frac{1}{R}\right] \qquad (6\text{-}5)$$

Using the values already mentioned the solvent reorganization energy is λ_S = 1.08 eV. The total reorganization energy is then calculated to λ = 1.38 eV. In order to estimate the electron transfer rate the coupling matrix element V is also needed. A precise determination would require a quantum mechanical approach but it was shown that V^2 can be approximated by the term: [De98]

$$V^2 = V_0^{\,2} \exp(-\beta(R - r_{a-} - r_{d+})) \qquad (6\text{-}6)$$

The highly flexible spatial arrangement of the pyropheo donor and C_{60} acceptor may allow conformations, in which the through-space distance is lower than the through-bond pathway. For this reason electron transfer may also occur by a through-space mechanism, even if the coupling matrix element at contact (V_0) is usually smaller than for a trough-bond situation. [Sak97,Wei04] For fullerene-based donor acceptor systems high values of V_0=100cm^{-1} for through-bond ET have been reported. This value is used as an upper limit for the molecular systems investigated. The distance attenuation factor ß for saturated hydrocarbon spacers typically exhibit values of 1 Å^{-1}. [Mur94,Gra05] Similar factors have been obtained for pure liquid electron transfer in polar solvents, therefore the damping factor is assumed to be ß=1 Å^{-1}, approximating both through-bond and through space ET. [Tav00,Sai04]

Using the values mentioned above the electron transfer rate was calculated to $k_{ET} = 8.9\times10^9$ s^{-1}

or τ_{ET} = 112 ps. The determined quenching rate from the observed short fluorescence decay component (τ_q=110 ps) of **FP6** is $k_q = 8.9\times10^9$ s^{-1} (see section 6.2.3) which is in very good agreement with this theoretical value. Comparable electron transfer rates have been reported for self-assembled zinc porphyrin-fulleropyrrolidine dyads in which donor and acceptor are spaced by about 10 Å.[Sou02]

After photoexcitation of the **FP6** molecule an intramolecular competition between energy delivery to the traps and transport to the pyropheo chromophore located close to the fullerene takes place. On the one hand the energy transfer to traps reduces the probability of an electron transfer. On the other side, FRET facilitates delivery of excitation from the periphery of the system to the pyropheo chromophore in close distance with the fullerene. As result, the probability of electron transfer is increased and therefore becomes the major deactivation pathway in the **FP6** molecule.

6.6 Non-radiative relaxation processes in P6, FHP6 and FP6

The occurrence of the shorter fluorescence decay times of 170ps and 160ps for **P6** and **FHP6** may be attributed to a trap consisting of a single pyropheo molecule, where the lowest excited singlet state is coupled to a large number of nearly degenerate, highly excited vibrational levels of the ground state of the whole molecule. This leads to effective nonradiative relaxation of the excited singlet state of the pyropheo molecule; the energy is converted to vibronic motion of the whole complex. In case of **FP6** a fast fluorescence decay time of 0.11ns with dominant amplitude of 0.47 was observed and has been attributed to an electron transfer process. This decay time is in the same time range of the shorter fluorescence lifetimes observed for **P6** and **FHP6**, therefore non-radiative relaxation processes may be a relevant factor of deactivation in the **FP6** molecule.

A formal treatment for nonradiative transitions in large molecules was developed between 1960 and 1980, and was published in [Rob62, Sie67,Avo77]. Two conditions must be fulfilled to observe strong non-radiative transitions. Firstly, the molecule must have a large number of vibrational modes in the ground state which is likely the case for the hexapyropheo molecular systems. Second, the coupling of the excited state to the excited vibrational states of the ground state must be effective enough. This might be valid for specific conformations of the molecules. Due to the high flexibility of the dendron system the probability to find the molecules in such a conformation is very high. Prediction of nonradiative relaxation rates would require the knowledge about number and energy of vibrational states. From UV/VIS

spectra it is not possible to obtain this information as vibrational states are only reflected in the broadening of the different electronic transitions visible in the absorption and fluorescence spectra only.

6.7 Macroscopic model for the transport processes in P6, FHP6, and FP6

The mathematical modeling of the electronic system of **P6**, **FHP6** and **FP6** should provide an enhanced understanding of the transfer processes from an initially excited pyropheo molecule to other pyropheo moieties and to different kinds of energy traps present in these systems. The main benefit of the purposed macroscopic model is that the efficiency of the excited state energy transport to the different traps can be evaluated from time-resolved fluorescence data as determined by TCSPC and from S_1 decay data as measured by TAS.

6.7.1 The model

Each **P6**, **FHP6** and **FP6** molecule contains 6 pyropheo chromophores. Within each complex the formation of different kinds of energy traps can occur. From an initially excited pyropheo donor molecule, the excited state energy can hop by Förster energy transfer to acceptors like energy traps, single pyropheo molecules or an electron transfer trap in case of **FP6**. The different types of acceptors are assumed to be of the following types:

Trap I consists of two pyropheo molecules forming a dimer where the dipole moments are aligned in parallel. The S_1 state lifetime of this trap type is referred to τ_{Trap1} and was determined to have a value of 0.7 to 0.9 ns.

Trap II comprises of a pyropheo dimer with oblique orientation of dipole moments, the S_1 state lifetime (τ_{Trap2}) was measured to 3.3 ns and 3.7 ns. The properties of Trap I and II have been discussed im section 6.4.2 and were also reported in recent publications [Erm05, Röd06b].

Trap III is assumed to consist of a single pyropheo molecule where the lowest excited S_1 state interacts with a large number of highly excited vibrational levels of the ground state of the whole molecule as supposed in section 6.6. The fluorescence lifetime of Trap III was found to be 170ps and 160ps for **P6** and **FHP6**, respectively**.**

Besides these types of traps, a well-separated pyropheo molecule can act as an acceptor as well. It exhibits a fluorescence lifetime of 5.7ns in DMF. Deactivation takes place mainly by fluorescence, internal conversion and intersystem crossing to the first excited triplet state. In

contrast to **P6** and **FHP6**, an additional dominant trapping process is active in the **FP6** molecule, namely electron transfer from pyropheo to C_{60} as it was discussed in section 6.5. This deactivation process will be denoted by **Trap IV** and is characterized by a fluorescence lifetime of 0.11ns.

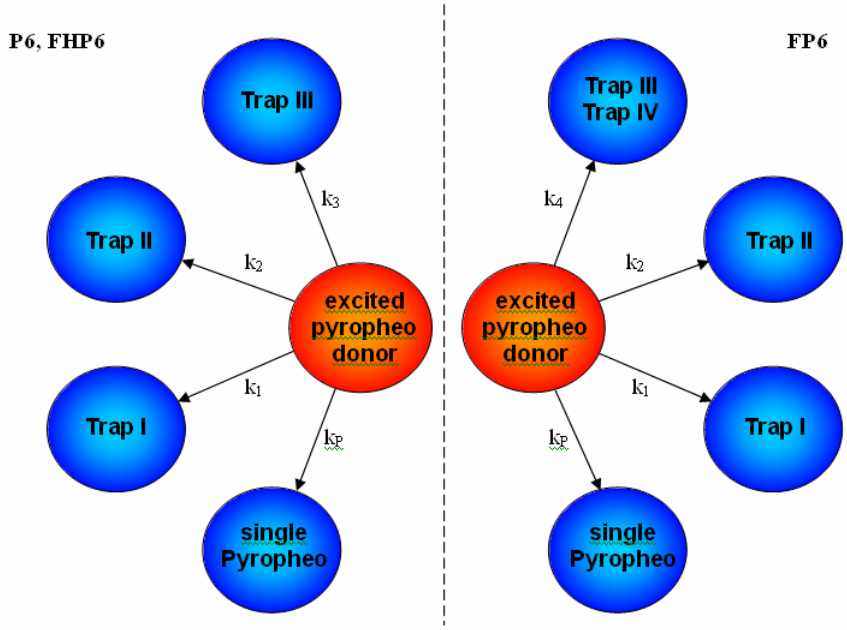

Figure 23. Average Förster energy transport rates from an initially excited pyropheo to the different possible acceptors for **P6**, **FHP6** and **FP6**.

Trap III and Trap IV have similar fluorescence lifetimes; therefore they can not be distinguished from fluorescence decay data. For this reason they are treated as one acceptor in the model for the **FP6** molecule as shown in Figure 23.

The proposed model is based on two hypotheses (***A, B***) and two simplifying assumptions (***C, D***):

***A*:** In a single **P6**, **FHP6** or **FP6** molecule not all types of traps exist but by observing a large number of molecules all types of energy acceptors can be found. (Ensemble average). The model is therefore only valid for a large number of molecules.

B: The energy can hop by Förster energy transfer from the excited pyropheo donor to an acceptor but also backwards with lower probability due to the lower fluorescence quantum yield of a trap with respect to pyropheo and associated lower FRET rate according to equations (6-1) and (6-2). Averging over a high number of excitations a directed transport of excited state energy to the acceptors occurs. The respective average transport rates for the excited state energy are noted as k_1, k_2, k_3, k_4 and k_p (See Figure 23). The inverse of the

transport rate is the average time to deliver excited state energy to the acceptor.

C: During excitation the incident photons may be captured directly by one of the acceptors. Due to the fact that the absorbance of traps is reduced to the pyropheo monomer (See section 6.4.2) it will be assumed that the incident photons can be harvested only by well separated "lonely" pyropheos chromophores.

D: The traps may exchange their excited state energy among each other but with a lower probability compared to deactivation processes occurring at each trap. We assume that no energy exchange occurs among the different types of traps.

For the purposed model a Jablonski diagram can be worked out containing the major deactivation processes.

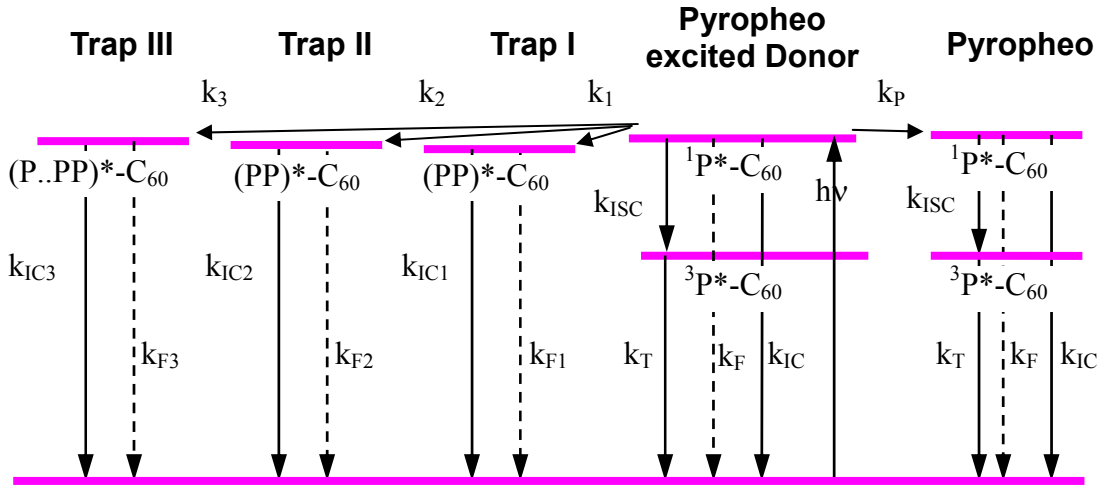

Figure 24. Jablonski Diagram for **P6** and **FHP6** based on the model assumptions.

In the following, a system of linear differential equation is set up and subsequently solved to obtain the time-dependent population of the excited states. Afterwards an expression for the theoretical time-dependent fluorescence emission is derived. This will be done for **P6** and **FHP6** by example, the calculation for **FP6** is similar and thus not explicitly given.

6.7.2 Formal treatment and solution of the differential equation system

For a mathematical representation of the system, abbreviations for states need to be introduced: **S1D**: Donor Pyropheo first excited singlet state; **T1D**: Donor Pyropheo first excited triplet state, **S1A**: Acceptor Pyropheo first excited singlet state; **T1A**: Acceptor Pyropheo first excited triplet state, **TR1**: Trap I first excited singlet state of the dimer; **TR2**: Trap II first excited singlet state of the dimer, **TR3**: Trap III pyropheo coupled to highly vibrationally excited levels of the ground state of the whole complex, **S0**: ground state of the

macromolecule.

The sum of all processes depopulating the first excited S1 pyropheo donor state (S1D) will be noted by

$$k = k_F + k_{ISC} + k_{IC} + k_P + k_1 + k_2 + k_3 \tag{6-7}$$

In case that the excitation pulse is short related to all other processes, the linear system of differential equations describing the processes summarized in the Jablonski diagram of **P6** and **FHP6** shown in Figure 24 is given by:

$$\begin{bmatrix} \dot{S1D} \\ S1A \\ TR1 \\ TR2 \\ TR3 \\ T1D \\ T1A \end{bmatrix} = \begin{bmatrix} -k & 0 & 0 & 0 & 0 & 0 & 0 \\ kp & -k_{ISC}-k_F-k_{IC} & 0 & 0 & 0 & 0 & 0 \\ k_1 & 0 & -k_{IC1}-k_{F1} & 0 & 0 & 0 & 0 \\ k_2 & 0 & 0 & -k_{IC2}-k_{F2} & 0 & 0 & 0 \\ k_3 & 0 & 0 & 0 & -k_{IC3}-k_{F3} & 0 & 0 \\ k_{ISC} & 0 & 0 & 0 & 0 & -k_T & 0 \\ 0 & k_{ISC} & 0 & 0 & 0 & 0 & -k_T \end{bmatrix} \cdot \begin{bmatrix} S1D \\ S1A \\ TR1 \\ TR2 \\ TR3 \\ T1D \\ T1A \end{bmatrix} \tag{6-8}$$

It is assumed that at t = 0, a fraction of N^* molecules from a total number N are in the pyropheo donor first excited state (S1D). The number of molecules remaining in the ground state are $S_0(t=0) = N - N^*$ under the precondition that all other states are not populated at t = 0. The initial conditions are:

$$\begin{gathered} S1D(0) = N^* \quad S1A(0) = 0 \quad TR1(0) = 0 \quad TR2(0) = 0 \quad TR3(0) = 0 \quad T1D(0) = 0 \\ T1A(0) = 0 \\ S1D(t) + S1A(t) + T1D(t) + T1A(t) + TR1(t) + TR2(t) + TR3(t) + S_0(t) = N \end{gathered} \tag{6-9}$$

The solution of the differential equation system with respect to the constraints yields the population of the different states over time. With the introduction of the average Förster energy transport rates k_1, k_2, k_3 and k_p, the system can be solved exactly in an algebraic closed form. The solution was obtained using the computer algebra system Maple 8.[Maple] Since only the time-dependent population of fluorescence emitting states is of interest, we can write:

$$S1D(t) = N \cdot \exp(-kt)$$

$$\begin{aligned} S1A(t) &= \frac{Nk_P}{k - k_F - k_{ISC} - k_{IC}} \cdot \left[\exp(-(k_F + k_{ISC} + k_{IC})t) - \exp(-kt)\right] \\ TR1(t) &= \frac{Nk_1}{k - k_{IC1} - k_{F1}} \left[\exp(-(k_{IC1} + k_{F1})t) - \exp(-kt)\right] \\ TR2(t) &= \frac{Nk_2}{k - k_{IC2} - k_{F2}} \left[\exp(-(k_{IC2} + k_{F2})t) - \exp(-kt)\right] \end{aligned} \tag{6-10}$$

$$TR3(t) = \frac{Nk_3}{k - k_{IC3} - k_{F3}}\left[\exp(-(k_{IC3} + k_{F3})t) - \exp(-kt)\right]$$

The expected fluorescence intensity $I_{theo}(t)$ emitted from a number of excited molecules is proportional to the product of the radiative rate constant and the time-dependent population of the $S_1(t)$ state. [Lak99] In case of **P6** and **FHP6** the observed fluorescence decay is the sum of the fluorescence emission from the excited donor and the different types of acceptors multiplied with their radiative rates.

$$I_{theo}(t) \sim k_F \cdot S1D(t) + k_F \cdot S1A(t) + k_{F1} \cdot TR1(t) + k_{F2} \cdot TR2(t) + k_{F3} \cdot TR3(t) \qquad (6\text{-}11)$$

k_{F1}, k_{F2} and k_{F3} denote the radiative fluorescence rate of the different traps whereas k_F refers to the emissive rate of the pyropheo molecule. (See Figure 24) Inserting the time-dependent population of the states S1D(t), S1A(t), TR1(t) TR2(t) and TR3(t) in (6-11) yields:

$$I_{theo}(t) \sim N^* \left\{ \begin{aligned} &\left(k_F - \frac{k_F \cdot k_P}{k - k_F - k_{isc} - k_{IC}} - \frac{k_{F1} \cdot k_1}{k - k_{F1} - k_{IC1}} - \frac{k_{F2} \cdot k_2}{k - k_{F2} - k_{IC2}} - \frac{k_{F3} \cdot k_3}{k - k_{F3} - k_{IC3}}\right) \cdot \exp(-kt) \\ &+ \frac{k_F \cdot k_P}{k - k_F - k_{ISC} - k_{IC}} \cdot \exp(-(k_F + k_{ISC} + k_{IC})t) + \frac{k_{F1} \cdot k_1}{k - k_{F1} - k_{IC1}} \cdot \exp(-(k_{F1} + k_{IC1})t) \\ &+ \frac{k_{F2} \cdot k_2}{k - k_{F2} - k_{IC2}} \exp(-(k_{F2} - k_{IC2})t) + \frac{k_{F3} \cdot k_3}{k - k_{F3} - k_{IC3}} \exp(-(k_{F3} - k_{IC3})t) \end{aligned} \right\} \qquad (6\text{-}12)$$

The rate constants can be replaced by the respective fluorescence lifetimes:

$$\tau_{TRAP1} = \frac{1}{k_{IC1} + k_{F1}} \quad \tau_{TRAP2} = \frac{1}{k_{IC2} + k_{F2}} \quad \tau_{TRAP3} = \frac{1}{k_{IC3} + k_{F3}} \quad \tau_{short} = \frac{1}{k} \quad \tau_F = \frac{1}{k_F + k_{ISC} + k_{IC}} \qquad (6\text{-}13)$$

The fluorescence lifetimes are introduced because they are observables which can be determined from fluorescence decay data (See section 6.2.3 and 6.2.6). We get:

$$I_{theo}(t) \sim N^* \left\{ \begin{aligned} &\left(k_F - \frac{k_F k_P \tau_F \tau_{Short}}{\tau_F - \tau_{Short}} - \frac{k_{F1} k_1 \tau_{TRAP1} \tau_{Short}}{\tau_{TRAP1} - \tau_{Short}} - \frac{k_{F2} k_2 \tau_{TRAP2} \tau_{Short}}{\tau_{TRAP2} - \tau_{Short}} - \frac{k_{F3} k_3 \tau_{TRAP3} \tau_{Short}}{\tau_{TRAP3} - \tau_{Short}}\right) \cdot \exp\left(-\frac{t}{\tau_{Short}}\right) \\ &+ \frac{k_F k_P \tau_F \tau_{Short}}{\tau_F - \tau_{Short}} \cdot \exp\left(-\frac{t}{\tau_F}\right) + \frac{k_{F1} k_1 \tau_{TRAP1} \tau_{Short}}{\tau_{TRAP1} - \tau_{Short}} \cdot \exp\left(-\frac{t}{\tau_{TRAP1}}\right) + \\ &\frac{k_{F2} k_2 \tau_{TRAP2} \tau_{Short}}{\tau_{TRAP2} - \tau_{Short}} \exp\left(-\frac{t}{\tau_{TRAP2}}\right) + \frac{k_{F3} k_3 \tau_{TRAP3} \tau_{Short}}{\tau_{TRAP3} - \tau_{Short}} \exp\left(-\frac{t}{\tau_{TRAP3}}\right) \end{aligned} \right\} \qquad (6\text{-}14)$$

In order to compare this function with the normalized measured fluorescence decay we need to normalize $I_{theo}(t)$ by requiring $I_{theo}(t=0)=1$. We finally obtain for the normalized time-resolved fluorescence decay based on the described model:

$$I_{theo}^{N}(t) =$$
$$\left(1-\frac{k_p\tau_F\tau_{Short}}{\tau_F-\tau_{Short}}-\frac{k_{F1}k_1\tau_{TRAP1}\tau_{Short}}{k_F(\tau_{TRAP1}-\tau_{Short})}-\frac{k_{F2}k_2\tau_{TRAP2}\tau_{Short}}{k_F(\tau_{TRAP2}-\tau_{Short})}-\frac{k_{F3}k_3\tau_{TRAP3}\tau_{Short}}{k_F(\tau_{TRAP3}-\tau_{Short})}\right)\cdot$$
$$\exp\left(-\frac{t}{\tau_{Short}}\right)+\frac{k_p\tau_F\tau_{Short}}{\tau_F-\tau_{Short}}\cdot\exp\left(-\frac{t}{\tau_F}\right)+\frac{k_{F1}k_1\tau_{TRAP1}\tau_{Short}}{k_F(\tau_{TRAP1}-\tau_{Short})}\cdot\exp\left(-\frac{t}{\tau_{TRAP1}}\right)+ \qquad (6\text{-}15)$$
$$\frac{k_{F2}k_2\tau_{TRAP2}\tau_{Short}}{k_F(\tau_{TRAP2}-\tau_{Short})}\exp\left(-\frac{t}{\tau_{TRAP2}}\right)+\frac{k_{F3}k_3\tau_{TRAP3}\tau_{Short}}{k_F(\tau_{TRAP3}-\tau_{Short})}\exp\left(-\frac{t}{\tau_{TRAP3}}\right)$$

The values of interest are the average energy transport rates k_1, k_2, k_3 and k_P from the initially excited pyropheo donor molecule to the acceptors. (See Figure 23 and Figure 24) There is no a-priori knowledge about the radiative rates of the traps k_{F1}, $k_{F2,}$ k_{F3} but it is known that the radiative rate does not vary with dimer formation significantly [Kha99], therefore we assume that these rates are equal to the radiative rate k_F of pyropheo. The reduction of the fluorescence quantum yield of **FHP6**, **P6** is mainly attributed to a significant increase of k_{IC} within the pyropheo dimers. All other values, namely τ_{Short}, τ_{Trap3}, τ_{Trap2}, τ_{Trap1}, τ_F were determined from time-resolved fluorescence and TAS measurements (See Table 2). By comparing the preexponential factors of the theoretical fluorescence decay time calculated using equation (6-15) with the measured values for the amplitudes of the five-exponential fluorescence decay shown in Table 2, the average energy transport rates k_1, k_2, k_3 and k_P can be determined.

The results are shown in Table 3 in addition to the transport quantum efficiencies which are given by the ratio of the average transport rate to the sum of all other transport rates for a given acceptor. For **FP6** a similar calculation was performed whereas the dominant electron transfer process is represented by Trap IV. Calculated values for **FP6** are also presented in Table 3.

Table 3. Average energy transport rates and average transport quantum efficiencies for FHP6, P6 and FP6 in DMF.

sample	type of acceptor	Average transport rate	Transport quantum efficiency
FHP6	Trap I	$k_1 = 2.1\times10^9 s^{-1}$	$\Phi_{TRAP1} = 0.16$
	Trap II	$k_2 = 7.9\times10^9 s^{-1}$	$\Phi_{TRAP2} = 0.54$
	Trap III	$k_3 = 2.6\times10^9 s^{-1}$	$\Phi_{TRAP3} = 0.20$
	Pyropheo	$k_P = 1.2\times10^9 s^{-1}$	$\Phi_{pyropheo} = 0.10$
P6	Trap I	$k_1 = 2.9\times10^9 s^{-1}$	$\Phi_{TRAP1} = 0.12$
	Trap II	$k_2 = 9.6\times10^9 s^{-1}$	$\Phi_{TRAP2} = 0.41$
	Trap III	$k_3 = 9.1\times10^9 s^{-1}$	$\Phi_{TRAP3} = 0.40$
	Pyropheo	$k_P = 1.7\times10^9 s^{-1}$	$\Phi_{pyropheo} = 0.07$
FP6	Trap I	$k_1 = 3.2\times10^9 s^{-1}$	$\Phi_{TRAP1} = 0.14$
	Trap II	$k_2 = 2.1\times10^9 s^{-1}$	$\Phi_{TRAP2} = 0.09$
	Trap III / Trap IV	$k_4 = 1.5\times10^{10} s^{-1}$	$\Phi_{TRAP3/TRAP4} = 0.67$
	Pyropheo	$k_P = 2.1\times10^9 s^{-1}$	$\Phi_{pyropheo} = 0.10$

6.7.3 Analysis

The average transport rates for **P6**, **FHP6** and **FP6** to the different types of traps can be estimated from the introduced model above. These rates represent a directed transfer which is actually the sum of several FRET transfer from the donor towards the acceptor and vice versa. For this reason these values are slower than the estimated rate for a single FRET event among pyropheo molecules in the range of a few picoseconds as it was calculated in section 6.4.1.

The rates determined for **FHP6** are all lower compared to the rates obtained for **P6.** This supports molecular modeling results where lower distances among the pyropheo molecules were observed for **P6** compared to **FHP6**. Consequently, the Förster energy transfer rates are higher compared to **FHP6**. The fullerene hexadduct in the **FHP6** molecule acts as a spacing element, preventing the dense folding of the complex. **FP6** can not be compared with **P6** and **FHP6** in this way because the electron transfer process denoted by Trap IV dominates over all other transport rates by at least 4.5 fold.

Within **FHP6** and **P6** the energy transport rate to Trap II with oblique orientation of the transition dipole moment is higher than to Trap I with parallel orientation of the dipole moments. For **FHP6** more than 50% of the energy transported by Förster transfer is stored in Trap II. We conclude that finding traps with oblique orientation of dipole moments is more probable. This is understandable as the number of possible arrangements between two pyropheo molecules with oblique orientation of transition dipole moments is higher compared to the possibilities of alignment with parallel orientation. The higher probability for the formation of Trap II was not found in case of the **FP6** molecule. This can be explained by a larger error in the lifetime of Trap II for **FP6.** It is rather large since the dominant electron transfer process leads to a strong reduction of the amplitude of all other processes which subsequently makes a precise fit very difficult.

The nonradiative deactivation of excited state energy mediated by Trap III is strongly enhanced in the **P6** molecule compared to **FHP6**. This behaviour is also reflected in the fluorescence quantum yields which are $\Phi_F = 0.42$ and $\Phi_F = 0.25$ for **FHP6** and **P6** relative to **P2**. [Reg07b] The transport quantum efficiency to Trap III in **P6** is two-fold higher compared to **FHP6**. Molecular modeling results showed that **P6** tend to fold densely. This may allow an efficient coupling of the pyropheo excited state to the large number of vibrationally excited ground states. (See section 6.6) The transport quantum efficiency of Trap III in the **FP6** molecule can not be extracted from the sum of Trap III and Trap IV, namely the electron transfer process but it was shown in section 6.5 that electron transfer is the main deactivation pathway.

With a probability of only 10%, the energy from the excited donor is transferred via Förster mechanism to single pyropheo units. The energy may further radiated by fluorescence, deactived by internal conversion or stored in the pyropheo T_1 state. In all other cases (90%), the energy is passed to different types of traps. The high efficiency of the trapping processes can be understood when we consider the quantum efficiency of a FRET event: $\Phi_{FET} = \frac{k_{FET}}{k_F + k_{IC} + k_{ISC} + k_{FET}}$. As the Förster energy transfer among neighboring pyropheos is so fast (1-20ps) compared to all other processes, a FRET process has a high probability to occur. Therefore a high number of FRET jumps is likely to take place after photoexcitation of the complex. Even if only one trap is present in a **P6**, **FHP6** or **FP6** molecule the probability that the excited state energy is stored in that trap by chance is greatly enhanced. This behavior is reflected in the low transport quantum efficiency to single pyropheo molecules.

6.8 Cellular uptake and Phototoxicity

The cellular uptake of **FHP6** and **P6** by Jurkat leukaemia cells (a special line of T-lymphocytes) and the generated phototoxicity of these compounds against these cells have been investigated by F. Rancan. Subcellular localization studies employing a confocal laser scanning microscope have been done as well. [Ran07a] The photobiological activity of **FHP6** and **P6** in comparison to the free photosensitizer (pyropheo) is briefly reviewed in the following section for the purpose of a combined analysis. Showing a very low singlet oxygen quantum yield (Φ_Δ=0.02), a significant photodynamic activity is not expected for **FP6**; hence it was not part of the photobiological study.

Table 4. Cellular uptake of FHP6, P6 and pyropheo by Jurkat cells and generated phototoxicity under illumination.

Incubation conc. [µM]	Cellular Uptake Extract concentration [nM]			Phototoxicity Living cells in %		
	Pyropheo	FHP6	P6	pyropheo	FHP6	P6
0.33	61 ± 7	49 ± 3	2 ± 1	46 ± 5	67 ± 4	100 ± 4
0.5	106 ± 10	158 ± 6	4 ± 3	42 ± 5	61 ± 7	99 ± 3
1.0	223 ± 8	259 ± 5	4 ± 2	18 ± 5	34 ± 7	99 ± 5
1.67	408 ± 18	317 ± 7	5 ± 2	9 ± 5	14 ± 7	94 ± 6

The intracellular uptake and phototoxicity of pyropheophorbide a, **FHP6** and **P6** was studied by incubation of Jurkat cells in a growth medium containing four different pyropheo equivalent concentrations.[Ran07a] Because of their water insolubility, the compounds were dissolved in DMF and afterwards mixed with the cell suspension resulting in a 0.5% DMF content of the mixture. For determination of the amount of sensitizer uptaken by the cell suspension, cells were harvested 24h after incubation and the photosensitizer was extracted from tumor cells using DMF. Concentration of the PS was quantified by fluorescence intensity of the extract relative to a standard curves. It was found that the intracellular uptake of **FHP6**, **P6** and pyropheo increased with the concentration of the compounds in the incubation suspension. Pyropheo reached the highest intracellular concentration, followed by **FHP6** and **P6**. The higher value observed for free pyropheo is a consequence of its low molecular size (MW: 536 g·mol^{-1}) and associated different uptake mechanism by tumor cells. Small molecules like pyropheo accumulate by diffusion through the cell membrane whereas

larger particles in the kDa range enter cells by endocytosis. This result is also supported by subcellular localization experiments which showed that **FHP6** and **P6** enriched mainly in lysosomes, a target of endocytosed molecules. In contrary, pyropheo distributed to various intracellular places for example vesicles near the cell nuclei, the perinuclear region and the plasma membrane. The cellular uptake of **P6** was significantly lower than **FHP6**. Rancan attributed this finding to the more asymmetric structure and higher amphiphilicity of the **FHP6** molecule in distinction to **P6**. As a result, the **FHP6** molecule might interact with receptors on the cell membrane directing a more efficient receptor mediated endocytotic uptake.

The phototoxicity experiments demonstrated a correlation between intracellular accumulation and singlet oxygen quantum yield of the compounds, and the percentage of dead cells after irradiation. Pyropheo exhibited a strong phototoxic effect (only 40% of living cells at an incubation concentration of 0.33μM), most of the cells had undergone apoptosis. At higher incubation concentrations, pyropheo induced mainly a necrotic cell death. It is assumed that at higher intracellular concentrations, the large amount of generated ROS under illumination causes an extensive damage to the cells, thus they undergo necrosis rapidly. **FHP6** showed intracellular concentration comparable to pyropheo but its phototoxicity is slightly lower with respect to pyropheo. This behaviour is ascribed to the lower singlet oxygen quantum yield of this compound. Consequently, **FHP6** is inducing predominatly apoptosis under illumination. The photoactivity of **P6** was the lowest relative to **FHP6** and pyropheo for the reason of the low cellular uptake and reduced singlet oxygen quantum yield of this compound.

6.9 Conclusions

Within chapter 6, photophysical data of hexapyropheophorbide a-fullerene [C60] molecules have been presented as obtained by steady state and time-resolved spectroscopic measurements in the UV/VIS/NIR range in addition to molecular modeling results and theoretical analysis of photoinduced intramolecular transfer processes. Furthermore a model was developed allowing quantitative statements about the efficiency of different deactivation processes after photoexcitation. Finally a brief review of the photobiological activity of **P6** and **FHP6** has been given.

In addition to its length, the flexibility of the dendron system connecting the six pyropheophorbide *a* molecules among one another (**P6**) and coupling it to a fullerene core (**FHP6**, **FP6**) allows a huge variety of possible conformations. In such systems with high degrees of freedom complex intramolecular interactions are conceivable.

Among adjacent pyropheo units excitonic interactions were observed in **FHP6**, **P6** and **FP6** leading to the formation of efficient energy traps. Two different types of pyropheo dimers could be resolved experimentally; one of them is formed by face-to-face stacking of two pyropheo molecules with parallel orientation of dipole moments (Trap I), the other one is characterized by oblique orientation of dipole moments (Trap II). [Hac05,Erm05,Hel05] The occurrence of a shorter fluorescence decay time in the range of 0.16-0.17ns might be attributed to a Trap III consisting of a single pyropheo molecule, where the S_1 state is coupled to a large number of nearly degenerated vibrational levels of the ground state of the whole molecule. (See section 6.6).

The excitation energy can hop from an initially excited pyropheo unit by Förster energy transfer to every other pyropheo molecule. Because the Förster transfer rate decreases with $1/r^6$ the jump to the nearest neighbor (distance 13 Å for **P6**) is much more probable than to non-neighboring pyropheos (average distance 24 Å for **P6**, 32 Å for **FP6**, and 38 Å for **FHP6**). For **P6** and **FHP6** a cascade of energy transfers is likely to occur until the energy vanishes in one of the traps. Also but with minor probability the energy is emitted via fluorescence or stored in the T_1 state of pyropheo. The trapping of excitation energy results in a reduction of singlet oxygen quantum yields of **FHP6** and **P6** compared to free pyropheo by 2.5 fold and nearly 4 fold, respectively, thereby limiting the potential phototoxicity of these compounds.

On the basis of the model introduced in section 6.7 it was estimated that the energy from the initially excited pyropheo molecule is transferred with a probability of 41% (**P6**) and 54% (**FHP6)** to Trap II and with a lower chance of 12% (**P6**) and 16% (**FHP6**) to Trap I. This was explained by the higher probability of finding traps with oblique orientation of dipole moments rather than discovering dimers having parallel orientation of their transition dipole moments. Furthermore the model revealed that in case of **P6** non-radiative transitions (trap III) are strongly enhanced compared to **FHP6** which has been attributed to a denser folding of the former as indicated by molecular modeling.

For **FP6** molecular simulation showed that one pyropheo unit can be located in closer proximity to the electron-accepting C_{60} fullerene core. This opens up the possibility of a fast electron transfer from the photoexcited pyropheo unit to the fullerene core. The measurements suggested that such a fast ET is indeed the main deactivation pathway. It was found that the electron transfer occurs with a rate constant of $k_q = 8.9\times10^9$ s^{-1} which is in very good agreement with the theoretical value as it was calculated using Marcus theory in section 6.5.

With a maximum probability of 67%, the energy from the initially excited pyropheo chromophore is passed to the pyropheo-C_{60} charge separating pair. Consequently, the singlet oxygen quantum yield of **FP6** is strongly reduced (Φ_{Δ}=0.02) and therefore applicability for PDT is not given. Instead, the **FP6** molecular system can be considered as combination of a light-harvesting system consisting of several separate pyropheo molecules and a charge-separating center. The observed formation of intramolecular sub divisions with different functions in a spontaneous self-assembling way may give ideas for the design of artificial molecular complexes of photosynthesis.

The intracellular uptake and phototoxicity of **P6** and **FHP6** as studied by F. Rancan showed that the covalent coupling of the pyropheo chromophores to the carrier system strongly influenced their photobiological properties. **FHP6** demonstrated a high cellular uptake compared to **P6** by Jurkat leukaemia cells, it reached nearly the intracellular concentration observed for free pyropheo. This property had been ascribed to the grade of asymmetry/amphiphilicity of **FHP6** in difference to **P6**. At the highest incubation concentration studied (1.67µM) only 14% of the tumor cells survived in case of **FHP6**, indicating the potential of the fullerene hexakis-adducts for multiplying units in molecular carrier systems for PDT. **P6** did not exhibited significant phototoxicity under illumination because of the lower uptake as well as reduced singlet oxygen quantum yield of this compound. Taking together all of the aforementioned aspects, **FHP6** can be regarded as the most promising complex of the investigated hexapyropheophorbide a series (**P6**, **FP6**, **FHP6**) for PDT. The major drawback, namely the water insolubility of this compound, can be overcome by coupling to an antibody; a proof of concept for a similar molecule carrying 12 pyropheo moieties has been reported already. [Hel06]

7 Poly (ethylene-glycol) based polymer carriers: PEG-ZnPP

7.1 Introduction

Among other water-soluble polymers, polyethylene glycol (PEG) is particularly attractive as a carrier for PDT because PEG is already used as a pharmaceutical excipient and is known to be non-toxic, non-immunogenic and biodegradable. (See Figure 25) PEG has a flexible, highly water-soluble chain; only three molecules of H_2O are required for the hydration of each ethylene oxide unit. [Liu69] Its high degree of hydration means that the polymer chain effectively has a "water shell", and this masks the photosensitizer from its biological environment during delivery to tumor cells. [Dun06] The process of covalent attachment of a PEG chain is known as "Pegylation". [Lo03, Ham01] The photosensitizer-polymer conjugate (**PEG-ZnPP**) investigated throughout this work consists of two PEG chains with a molecular weight of 5000 each conjugated through an ethylenediamine linkage to propionic acid residues of the hydrophobic zinc-protoporphyrin (**ZnPP**) photosensitizing molecule. (See Figure 25) The resulting conjugate with an MW of 11kDa is highly watersoluble, in contrast to ZnPP which is very hydrophobic. **ZnPP** was selected among other photosensitizers because it can kill tumor cells not only by its photosensitizing property but also exhibits antitumor activity by two alternative mechanisms which are also active in the absence of light.

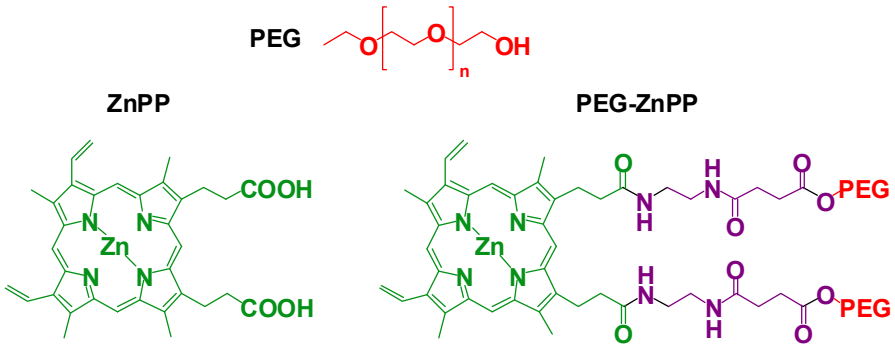

Figure 25. Chemical structures of polyethylene glycol (PEG), zinc protoporphyrin (**ZnPP**) and the conjugate **PEG-ZnPP**

Firstly, **ZnPP** is known to inhibit heme-oxygenase-1 (HO-1) which is highly upregulated in many cancer cells. HO-1 catalyses the degradation of heme in the presence of oxygen to liberate biliverdin, iron and CO. Biliverdin is further converted to bilirubin which is a very potent antioxidative agent. [Fan03] Therefore the suppression of HO-1 by **ZnPP** makes cells

more vulnerable to oxystress which is usually present under *in vivo* conditions. It was published that **PEG-ZnPP** significantly reduces tumor growth in mice through this mechanism. [Fan03,Fan04] Secondly there is evidence that **ZnPP** can affect signal transduction in tumor cells involving down regulation of oncogenes which is associated with reduced survival of malignant cells. [May04] The utilization of the photosensitizing property of **ZnPP** for photodynamic therapy did not gain much attention in the past for two reasons. It is known that protoporphyrin is photooxygenated in the presence of molecular oxygen. Investigations showed that nearly all of the photoproducts formed via direct irradiation resulted from singlet-oxygen attack on the ground-state protoporphyrin.[Cox82] Besides the reduced photostability, ZnPP also has a low absorbance in the therapeutic window of biological tissue. (See section 2.4) The working hypothesis is that, despite these drawbacks, the combination of all antitumor mechanisms by **ZnPP** would lead to a superior therapeutic effect. The fluorescence lifetime τ_F and quantum yield Φ_F of **ZnPP** dissolved in ethanol have been reported to 1.8ns and 0.034, respectively. Similar compounds like zinc porphyrin (ZnP) and zinc octaethylporphyrin (ZnOEP) have nearly identical τ_F and Φ_F values, indicating that conjugation of methyl or ethyl groups at the outer positions of the pyrrole rings do not have a significant effect on the electronic system of the protoporphyrin macrocycle. The ISC quantum yield of **ZnPP** has been measured to Φ_{ISC}=0.90 in ethanol. [Fei86] Φ_{ISC} is very high compared to the metal-free protoporphyrin, a direct consequence of enhanced spin-orbit coupling between singlet and triplet states induced by the zinc atom; a phenomenon called heavy-atom effect. [Sol05] ZnP, structurally similar to **ZnPP**, has a triplet state energy of 1.8eV and a singlet-triplet energy gap of 0.38eV. [Fei82] For ZnOEP the S_1-state lies 2.15eV above the ground state as measured in acetonnitrile.[Bar84]

The influence of PEG chains on the photophysical properties of **ZnPP** and the generation of singlet oxygen under illumination is unknown and will be investigated in a first step. After evaluation of the photophysical behaviour of **ZnPP** and **PEG-ZnPP** in solution, the generation of singlet oxygen by **PEG-ZnPP** in tumor cells is studied by means of *in vitro* laser flash photolysis. In the second step the photobiological activity of **PEG-ZnPP** is compared to **ZnPP** in order to estimate the potential of **PEG-ZnPP** for photodynamic therapy use. For this purpose the cellular uptake and phototoxicity of **PEG-ZnPP** against Jurkat leukaemia cells will be reviewed.

7.2 Photophysical characterization

7.2.1 Steady-state absorption spectra

The absorption spectrum of free **ZnPP** in EtOH reassembles that of metalloporphyrins consisting of the Soret band and the Q_x and Q_y band transitions with lower transition dipole moments and therefore lower absorbance. (See Figure 26)

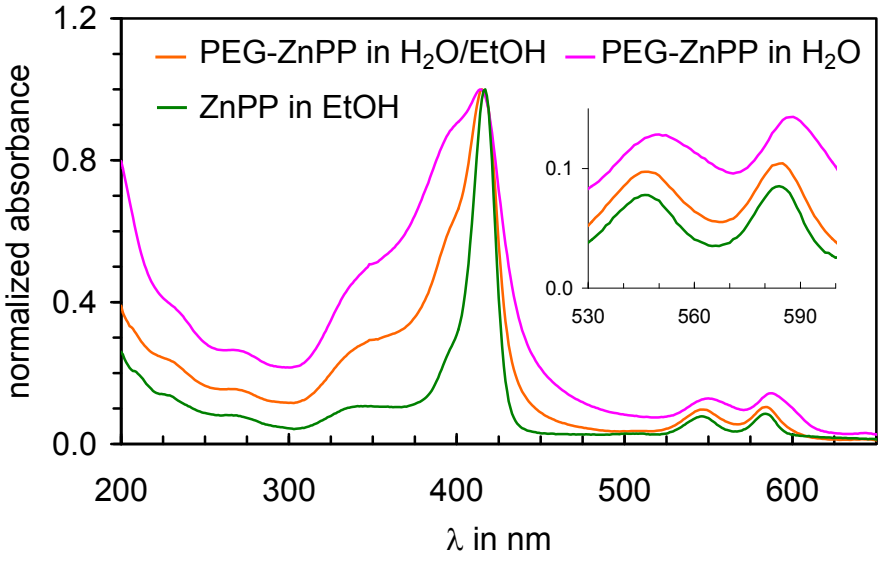

Figure 26. Normalized absorption spectra of **PEG-ZnPP** in H_2O/EtOH (30:70) mixture and **PEG-ZnPP** in H_2O. For comparison the spectrum of ZnPP in ethanol is also shown.

The Soret band of **PEG-ZnPP** in a H_2O/EtOH (30:70) mixture and in H_2O exhibits a hypsochromic shift by 2nm and 3nm, respectively, compared to that of **ZnPP** in ethanol. Furthermore a strong broadening of the Soret band was observed for this compound. The Q_x and Q_y band of **PEG-ZnPP** in H_2O and in H_2O/EtOH are red-shifted relative to **ZnPP** in EtOH and the relative intensities of the Q-bands with respect to the Soret band are enhanced for **PEG-ZnPP**. These effects increase with lower content of ethanol in the H_2O/EtOH mixture and achieve a maximum for **PEG-ZnPP** dissolved in H_2O. In addition, there is no indication that the PEG polymer contributes to the UV/VIS region of the absorption spectrum of pegylated **ZnPP**.

The changes in the absorption spectrum of **PEG-ZnPP** compared to free **ZnPP** are attributed to excitonic interactions among aggregated **PEG-ZnPP** molecules. Similar effects in the absorption spectrum have been observed for aggregated **ZnPP** clusters in nanoporous

environments. [Lin06] Excitonic coupling describes the interaction between transition dipole moments of chromophores in close proximity. In case of a mutual distribution of angles of the aggregated chromophores, a prevalent blue or red shift of the Soret band is not expected, instead a broadening of the Soret band for a larger ensemble of aggregated **PEG-ZnPP** molecules occurs. With higher ethanol content, aggregation tendency of **PEG-ZnPP** decreases, visible in the spectral characteristics already described.

7.2.2 Steady-state fluorescence

The fluorescence spectra of **PEG-ZnPP** in H_2O, **PEG-ZnPP** in a H_2O/EtOH mixture and **ZnPP** in ethanol were measured by excitation of the samples at 550nm, the optical density was adjusted to 0.2 at this wavelength. The normalized fluorescence spectra are depicted in Figure 3. The wavelength positions of the fluorescence band maxima are not dependent on the solvents used, they are located at 589nm and 644nm for all of the investigated samples.

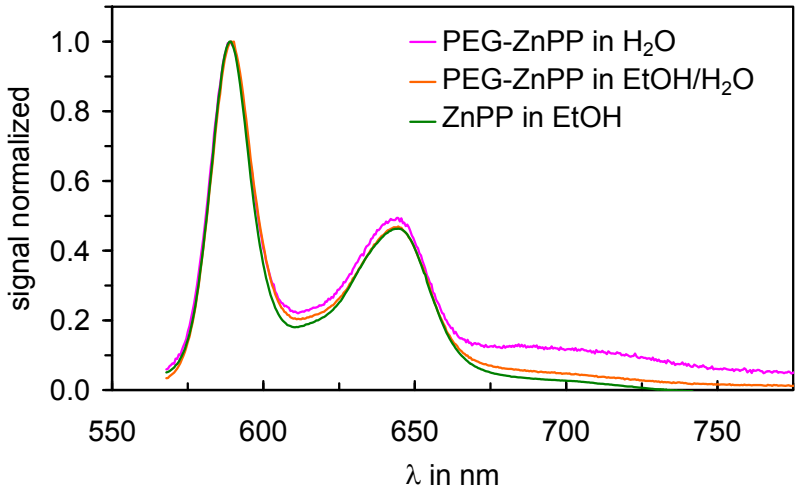

Figure 27. Normalized fluorescence spectra of **PEG-ZnPP** in a H_2O/EtOH (30:70) mixture and **PEG-ZnPP** in H_2O. For comparison the spectrum of ZnPP in ethanol is also shown.

For **PEG-ZnPP** a significant broadening of the fluorescence band was observed in comparison to **ZnPP** in ethanol which is especially visible in the red tail of the fluorescence above 675nm. The broadening increases with higher water content of the solvent, e.g. higher polarity, and achieves a maximum for **PEG-ZnPP** dissolved in pure H_2O. For determination of the fluorescence quantum yield according to equation (4-1), ZnTPP in ethanol (Φ_F=0.022) was selected as a standard because of its similar absorption and fluorescence spectrum. [Aav84] The fluorescence quantum yield of **ZnPP** in ethanol was determined to 0.040.

This low value is a direct consequence of enhanced intersystem crossing induced by the zinc atom. For **PEG-ZnPP** a strong fluorescence quenching was observed. In a H_2O/EtOH mixture a value of 0.023 and in pure H_2O a value of 0.008 was obtained.

The observed quenching of fluorescence intensity and broadening of the fluorescence spectrum in case of **PEG-ZnPP** is an additional indicator for the aggregation of **PEG-ZnPP** molecules in solution. Excitonic interactions among aggregated **ZnPP** chromophores lead to delocalisation of excitation energy over the formed cluster. With increasing number of participating molecules, the number of available states increases corresponding to the observed broadening of the fluorescence spectrum. Quenching of the fluorescence intensity has been observed for many aggregated systems. [Lin06, Tog04, Eic00] This effect increases with higher polarity of the solvent.

7.2.3 Time-resolved fluorescence

The fluorescence lifetime of **ZnPP** in EtOH and **PEG-ZnPP** were measured by time-correlated single photon counting technique. The samples were excited at 400nm using the frequency doubled pulses of a Ti:Sa laser. In order to minimize the aforementioned photobleaching of **ZnPP** by singlet oxygen, the samples were flushed with N_2 for 40min prior to the measurement. The fluorescence was detected at the intensity maximum of the fluorescence band located at 589nm.

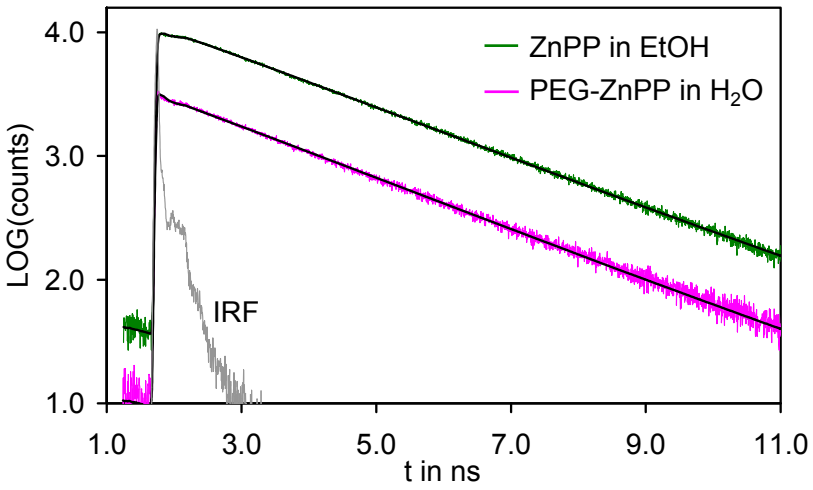

Figure 28. Time-resolved fluorescence emission decay curves of **ZnPP** in EtOH and **PEG-ZnPP** in H_2O. The FWHM of the instrument response function (IRF) was determined to 80ps.

The measured fluorescence decay curves of **ZnPP** and **PEG-ZnPP** were fitted by two-exponential functions which gave low chi-square error values between 1.1 and 1.3. **ZnPP** in EtOH exhibits a fast (τ_{Short} = 0.15ns) decay component with a low amplitude of 11% and a longer decay time of τ_{long} = 2.09 ns possessing a dominant amplitude of 89%. The long decay time belongs to monomeric **ZnPP** in EtOH whereas the short component is attributed to a **ZnPP** aggregates. It is known that free **ZnPP** tend to form aggregates, even at low concentrations in unpolar solvents. [Lin06]

For **PEG-ZnPP** a short decay component of τ_{Short}=0.133ns having an amplitude of 35% and a long decay component of 2.04ns with 65% were found. The long decay time of this compound is similar to free **ZnPP** indicating that covalent attachment of PEG chains does not pertubate the electronic properties of the **ZnPP** macrocycle. The higher amplitude of the short process points out that a significant higher fraction of **PEG-ZnPP** molecules are aggregated in H_2O compared to **ZnPP** in ethanol. This finding supports the interpretation of steady-state absorption and fluorescence spectra that **PEG-ZnPP** forms higher molecular weight assemblies.

The quenching rate k_{nr} deactivating the first excited state of aggregated **PEG-ZnPP** can be determined from equation (7-1).

$$k_{nr} = \frac{1}{\tau_{Short}} - \frac{1}{\tau_{long}} \qquad (7\text{-}1)$$

For **PEG-ZnPP** a value of $k_q = 0.7\times10^{10}s^{-1}$ was obtained, similar results have been found for tetraphenylporphyrin aggregates in aqueous solvent mixtures.[Kha99]

7.2.4 Time-resolved singlet oxygen emission

In order to evaluate the potential of **PEG-ZnPP** for photodynamic therapy, the ability of **PEG-ZnPP** and free **ZnPP** to generate singlet oxygen under illumination was investigated. This was accomplished by time-resolved measurement of the weak 1270nm emission of singlet oxygen being generated by **PEG-ZnPP** and **ZnPP** relative to a known standard. (See Figure 29) Rose Bengal in D_2O (Φ_Δ=0.75) and in EtOH (Φ_Δ=0.86) was chosen as a reference because of its high singlet oxygen quantum yield and its high absorbance at the excitation wavelength (550nm). It was found that **ZnPP** in EtOH efficiently generates $^1O_2$ with a quantum yield of Φ_Δ=0.88. The lifetime of the singlet oxygen emission of **ZnPP** in ethanol was determined to 14µs. The measurement of singlet oxygen emission photosensitized by **PEG-ZnPP** was carried out in D_2O for the reason that the lifetime of $^1O_2$ in D_2O is

significantly higher than in H_2O in addition to the increased transmission of D_2O for 1270nm. [Oel99] **PEG-ZnPP** in D_2O generates singlet molecular oxygen with a quantum yield of Φ_Δ=0.17. The lifetime was determined to 61µs which matches the well-known lifetime of $^1O_2$ in D_2O of 60µs. [Gor78] The singlet oxygen quantum yield of **PEG-ZnPP** is more than 5 fold lower than value of **ZnPP** in EtOH. This is attributed to a decrease of the intersystem crossing quantum yield (Φ_{ISC}), a direct consequence of aggregation of **PEG-ZnPP** molecules in solution as indicated by steady state absorption and fluorescence spectroscopy.

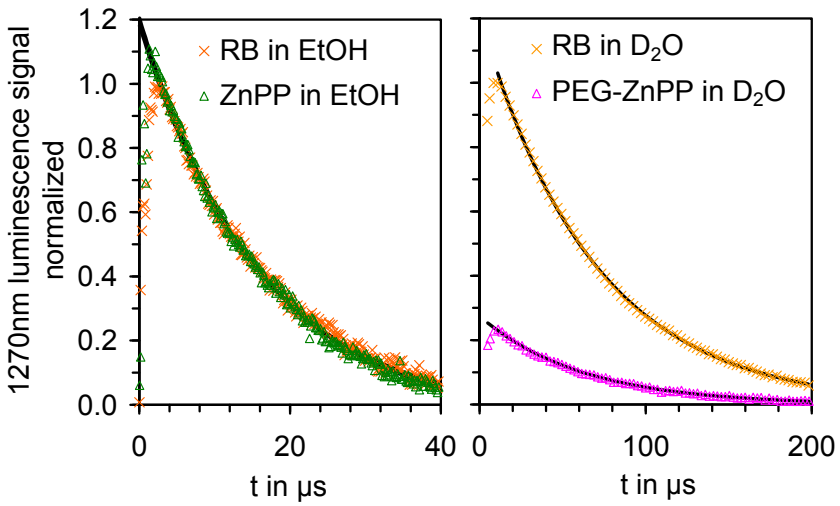

Figure 29. Time resolved singlet oxygen emission. Left: In EtOH photosensitized by **ZnPP**. Right: In D_2O photosensitized by **PEG-ZnPP**. Rose Bengal served as a known standard.

In a strict sense, according to equation (2-7), the reduction of Φ_Δ may also be caused by shortening of the triplet lifetime (τ_T) or a reduction of the energy transfer rate k_{EnT} to molecular oxygen. The latter is unlikely as there is no indication for a strong shift of the triplet energy level which would influence k_{EnT}. The following laser flash photolysis measurements answer this question and even more important, evaluate the potential of **PEG-ZnPP** to generate singlet oxygen within tumor cells.

7.3 Laser flash photolysis

The method of laser flash photolysis allows indirect determination of singlet oxygen formation via triplet lifetime measurement. (See section 2.2 and 4.1.5). The triplet lifetime can be obtained by monitoring the transient absorbance change ΔA after excitation probed at T_1-T_n transitions of the photosensitizer. For **ZnPP** the triplet-triplet absorption band is located

at 480nm. [Fei86] The samples were excited at the maximum of the Soret band of **ZnPP** at 420nm.

7.3.1 Measurements in solution

Figure 30 depicts the normalized transient absorbance change of **PEG-ZnPP** in H_2O. In the presence of oxygen the triplet lifetime was measured to $\tau_T(O_2)$=2.5µs whereas in an environment with low oxygen concentration (through 40min N_2 flushing of the sample) the triplet lifetime of this compound increased up to 406µs.

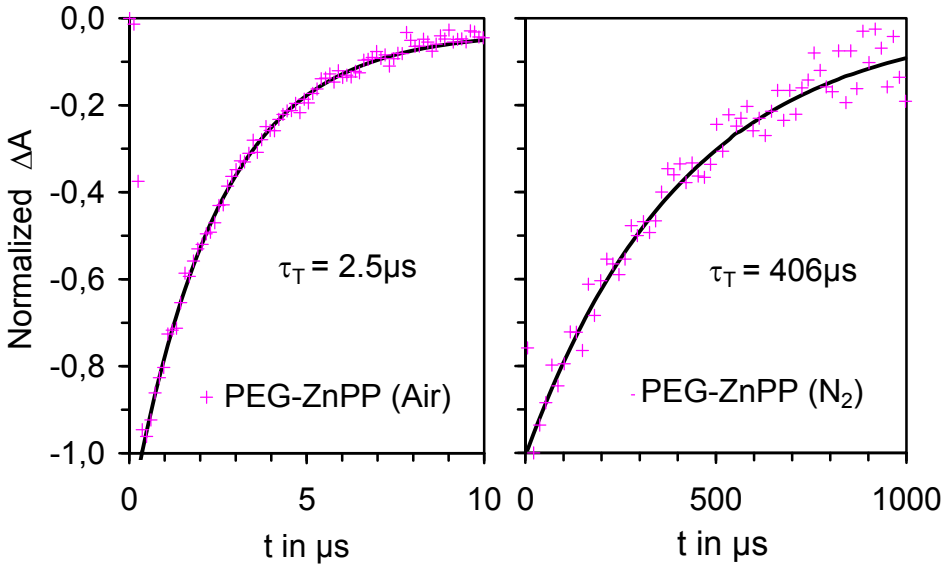

Figure 30. Laser flash photolysis of **PEG-ZnPP** in H_2O. Left: under normal air conditions. Right: after 40min N_2 flushing.

The strong decrease of the triplet lifetime in presence of oxygen shows that the triplet state is completely quenched by molecular oxygen in solution. In a deoxygenated environment the triplet lifetime of **PEG-ZnPP** in H_2O is higher than the value obtained for **ZnPP** in EtOH (τ_T=280µs). It was hypothesized that the nonionized COOH groups attached to the protoporphyrin interact with the aromatic ring causing a decrease in the triplet lifetime in case of **ZnPP**. [Fei86] Apart from this; the triplet lifetime of **ZnPP** is strongly dependent on the solvent and therefore highly sensitive for its surrounding microenvironment. The long lifetime of the triplet state in case of **PEG-ZnPP** in a deoxygenated environment shows that the reduction of the singlet oxygen quantum yield must be attributed to the decrease of the intersystem crossing quantum yield caused by aggregation of **PEG-ZnPP** molecules in H_2O. The triplet quenching rate constant can be obtained by

$$k_{EnT}[O_2] = \frac{1}{\tau(O_2)} - \frac{1}{\tau(N_2)}$$

Using the experimentally determined triplet lifetime under the presence and absence of O_2, a rate constant of $k_{EnT}[O_2] = 4.1\times10^5 s^{-1}$ was found. For estimation of the bimolecular quenching constant k_{EnT}, this value must be divided by the concentration of molecular oxygen $[O_2]$ in H_2O at room temperature. With $\sim3\times10^{-4}M$ at 293K [Haa86], the bimolecular quenching rate constant is calculated to $1.3\times10^9 M^{-1}s^{-1}$ which is in the range of values reported in the literature. [Sch03]

7.3.2 In vitro studies

The direct measurement of the faint 1270nm emission of $^1O_2$ in viable cells is hard to measure because of the usually low intracellular concentration of the photosensitizer. Thus, in vitro laser flash photolysis provides a suitable alternative because the singlet oxyen generation is related to the triplet lifetimes according to equation (4-17). Under normal aerobic conditions a triplet lifetime of $\tau_T(O_2)=27\mu s$ was measured for **PEG-ZnPP** in cells.

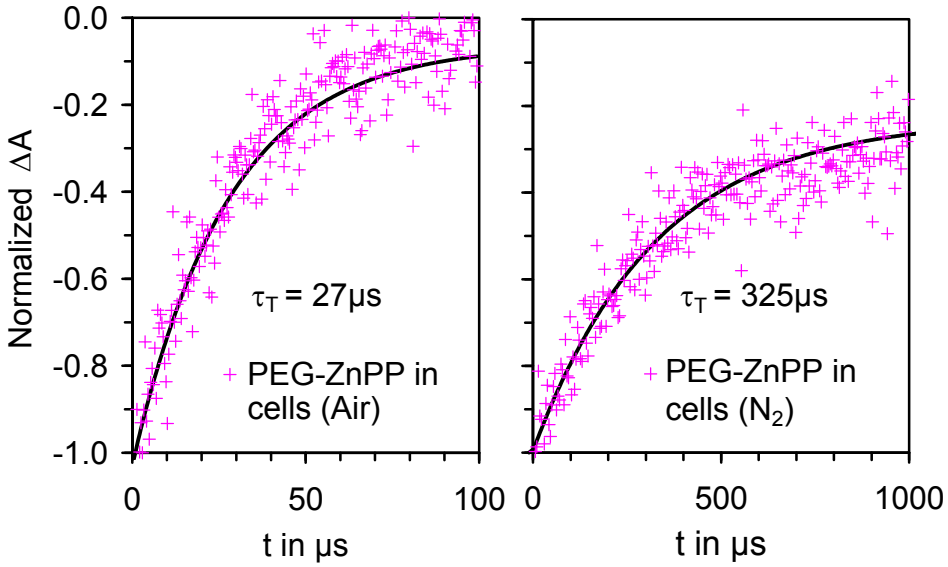

Figure 31. Laser flash photolysis of **PEG-ZnPP** in Jurkat leukaemia cells suspended in PBS. Left: under normal air conditions. Right: after 40min N_2 flushing.

This value is higher than the one obtained in H_2O and indicates accumulation in cellular compartments with lower oxygen concentration or a lowered diffusion rate of reactants in regions with higher viscosity although the latter possibility is more likely in this case. [Ave98a] For **PEG-ZnPP** in cells after 40min N_2-flushing a triplet lifetime of $\tau_T(N_2)=325\mu s$

was obtained, and a significant bleaching of the triplet state occurred.

The observed bleaching is evident from the induced absorbance change depicted in the left part of Figure 31 which does not approach the value before excitation. This can be treated as an indication for a chemical change of the photosensitizer. About 25% of the T_1-populated **PEG-ZnPP** molecules undergo this process after excitation assuming that the photoproduct does not contribute to the induced T_1-T_n absorbance. The origin of this bleaching process has been mentioned in section 7.1 already. From the populated T_1-state, energy is transferred to molecular oxygen, resulting in the generation of $^1O_2$ which subsequently reacts with the ground state **ZnPP** chemically. In solution no bleaching was observed which can be explained by the much lower singlet oxygen quantum yield due to aggregation of **PEG-ZnPP**.

Based on these findings it is suggested that the aggregated assemblies of **PEG-ZnPP** in H_2O disintegrate after cellular uptake and that **PEG-ZnPP** is preserved primarily in its monomeric water-soluble form in more lipophilic compartments of tumor cells. It generates singlet oxygen under illumination in tumor cells but with a lower quantum yield than monomeric **ZnPP** in EtOH. Using Φ_{ISC}=0.90 [Fei86] and the measured triplet lifetimes of $\tau_T(O_2)$=27µs and $\tau_T(N_2)$=325µs, an upper limit for the singlet oxygen quantum yield of Φ_Δ=0.83 was calculated for monomeric **PEG-ZnPP** in tumor cells based on equation (4-17). A part of the generated singlet oxygen molecules immediately react with **ZnPP** while others may oxidize vital compartments of tumor cells.

7.4 PDT relevant biological activity of PEG-ZnPP

Studies about the uptake of **PEG-ZnPP** by tumor cells and the generated phototoxicity under illumination have been carried out in cooperation with F. Rancan. For the purpose of a combined analysis, the photobiological activity of **PEG-ZnPP** is briefly reviewed in the following section.

The intracellular uptake of **ZnPP** and **PEG-ZnPP** increased with concentration of compounds in the incubation suspension. (See Table 5) The concentration of **PEG-ZnPP** within cells was higher compared to **ZnPP** at low incubation concentrations whereas at higher concentrations of 2.5µM and 5µM, a reverse behaviour was found. This shows that covalent attachment of hydrophilic PEG-chains does not support the uptake of **ZnPP** by Jurkat leukaemia cells.

Table 5. Cellular uptake of **PEG.-ZnPP** and **ZnPP** by Jurkat cells and phototoxicity against Jurkat cells of **ZnPP** and **PEG-ZnPP**.

Incubation conc. [μM]	Cellular Uptake Extract concentration [nM]		Phototoxicity Living cells in %	
	ZnPP	PEG-ZnPP	ZnPP	PEG-ZnPP
0.5	14 ± 1	30 ± 3	100 ± 5	96 ± 3
1.0	29 ± 1	38 ± 1	90 ± 12	98 ± 5
2.5	71 ± 20	60 ± 16	100 ± 1	97 ± 2
5	142 ± 17	86 ± 10	97 ± 2	60 ± 2

After irradiation, the administered free **ZnPP** generates no phototoxic effect. **PEG-ZnPP** exerted significant phototoxic activity only at a concentration of 5 μM as shown in Table 5. In the absence of light **PEG-ZnPP** and **ZnPP** do not cause any intracellular toxicity at the incubation concentrations studied. This result shows that HO-1 inhibition by **ZnPP** does not have an effect on cell survival of Jurkat cells in vitro, although more oxystressed systems may prove this possibility in vivo. Furthermore it was found that **PEG-ZnPP** is mainly inducing the apoptotic cell death pathway. [Reg07a]

7.5 Conclusions

Zinc protoporphyrin is a very interesting photosensitizer for photodynamic tumor therapy, mainly because of its high singlet oxygen quantum yield of Φ_Δ=0.88 (in EtOH) and the intrinsic secondary antitumor activity of **ZnPP** mentioned in section 2.4 which are also active in the absence of light. By covalent attachment of two PEG polymer chains the water solubility of **ZnPP** increased dramatically, making it possible to administer the resulting conjugate (**PEG-ZnPP**) into the blood stream of patients. The present photophysical characterization was performed to evaluate the potential of **PEG-ZnPP** for photodynamic therapy.

Analysis of steady-state absorption and fluorescence spectra showed that **PEG-ZnPP** forms aggregates in aqueous environments. The observed excitonic interactions among different **ZnPP** units prove that super molecular assembly of **PEG-ZnPP** is based on close assoziation between hydrophobic **ZnPP** core moieties. This understanding is equivalent to the formation of polymeric micelles in aqueous solutions by highly amphiphilic **PEG-ZnPP** molecules as

depicted in Figure 32.

The clustering of hydrophobic **ZnPP** molecules in aqueous surroundings is based on the "hydrophobic effect".[Cha05] The molecular size of the **PEG-ZnPP** polymer micelle in H_2O has been reported to achieve molecular weights of 70kDa [Sah02]. This corresponds to an average assembly of six **PEG-ZnPP** molecules. It has been found that for this reason selective tumor accumulation of **PEG-ZnPP** assemblies driven by the EPR-effect takes place in vivo. [Fan03]

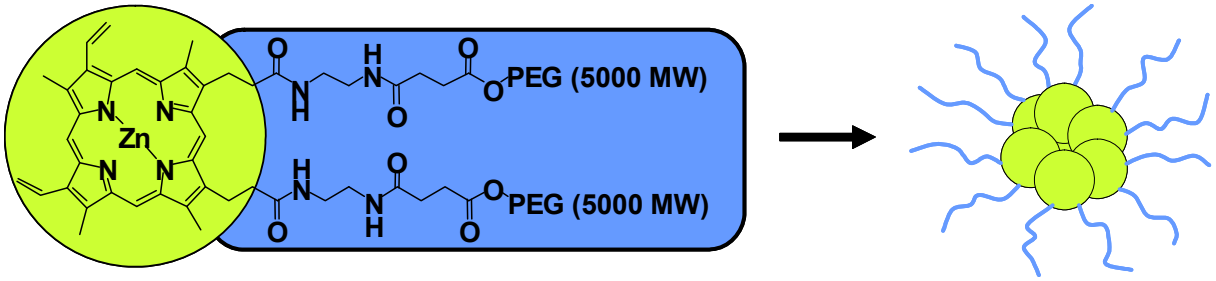

Figure 32. Formation of polymeric micelles by amphiphilic **PEG-ZnPP** molecules in aqueous solution.

Steady state absorption and fluorescence spectra further reveal that the aggregation state of **PEG-ZnPP** is heavily dependent on the polarity of the solvent. The equilibrium between monomeric and aggregated **PEG-ZnPP** is shifted towards the latter in case of more polar environments. Time-resolved fluorescence decay measurements showed that the particular covalent attachment of the PEG chain does not influence the electronic properties of the bound **ZnPP** moiety. Furthermore aggregation of **PEG-ZnPP** units leads to the appearance of non-radiative processes rapidly deactivating the first excited singlet state of **ZnPP**. This behaviour is typically for aggregated porphyrin systems. Due to the efficient S_1 deactivation process, the intersystem crossing quantum yield is reduced as well as the singlet oxygen quantum yield which was determined to Φ_Δ=0.17. This notion is evidenced by the relative fluorescence quantum yield (Φ_{Frel}) of **PEG-ZnPP** with respect to free **ZnPP** which is of similar size compared to the relative singlet oxygen quantum yield ($\Phi_{\Delta rel}$) shown in Table 6.
The suppression of singlet oxygen generation through association of **PEG-ZnPP** molecules into macromolecular assemblies is very desirable for the reason that as long as this compound is circulating in the blood stream of the patient, its potential phototoxicity is inhibited.
Despite the strongly reduced population of the first excited triplet state of **PEG-ZnPP** in H_2O

due to aggregation, laser photophotolysis measurements could show that the generation of singlet oxygen occurs by energy transfer from the T_1-state of **ZnPP**.

Table 6. Important photophysical properties of ZnPP and **PEG-ZnPP**. * JCS: Jurkat cell suspension.

Photophysical property	ZnPP		PEG-ZnPP	
Soret band maximum [nm]	417	EtOH	414	H_2O
Q(0,0) band maximum [nm]	584	EtOH	588	H_2O
fluorescence band maximum [nm]	589	EtOH	589	H_2O
Φ_{Frel}	1.0	EtOH	0.2	H_2O
$\Phi_{\Delta rel}$	1.0	EtOH	0.19	D_2O
τ_F [ns]	0.15 ns (11%) 2.09 ns (89%)	EtOH	0.13 ns (35%) 2.04 ns (65%)	H_2O
τ_T [µs] under normal air conditions		EtOH	2.5 ± 0.2 27 ± 3	H_2O in JCS*
τ_T [µs] after 40min N_2 flushing	280 ± 28	EtOH	406 ± 40 325 ± 30	H_2O in JCS*

In vitro laser flash photolysis proved that generation of singlet oxygen photosensitized by **PEG-ZnPP** within Jurkat tumor cells occurs after excitation. Results indicate decomposition of aggregates after cellular uptake. **PEG-ZnPP** is preserved primarily in its monomeric form in tumor cells whereas the upper singlet oxygen quantum yield was estimated to $\Phi_\Delta = 0.83$. Moreover it was found that a significant fraction of up to 25% of photosensitizing molecules immediately react with the generated singlet oxygen, resulting in a significant photobleaching of this compound in vitro. The internalization of macromolecular aggregates is known to occur by endocytosis. [Kal98] Experiments revealed that the intracellular concentration of **PEG-ZnPP** cells is not higher compared to free **ZnPP**. Thus, the PEG carrier does not enhance the uptake of the photosensitizer into Jurkat leukemia cells. As a consequence of the low intracellular concentration of ZnPP, the generated phototoxicity under illumination is also reduced. Only for the highest incubation concentration studied (5µM **ZnPP** equivalent), a significant phototoxicity for **PEG-ZnPP** was observed, about 40% of the tumor cells were killed. The desired suppression of singlet oxygen generation in solution or during delivery to the tumor is based on aggregation of hydrophobic **ZnPP** cores in aqueous surroundings. For

photosensitizers showing water solubility, for example Rose Bengal (RB), strong aggregation effects are not expected in aqueous solution. Indeed, it was reported that the photophysical properties of free Rose Bengal are not different to its pegylated form. The singlet oxygen quantum yield of the RB-polymer conjugate is not reduced compared to unbound Rose Bengal (Φ_Δ=0.75 in H_2O). [Now01] This leads to the perception that amphiphilicity of such PEG-photosensitizer conjugates is highly benefical for achieving macromolecular size and the mentioned reduction of singlet oxygen in aqueous solution. The main disadvantage of the PEG carrier belongs to its low payload capacity. Consequently, PEG chains cause undesirable high viscosity, even for moderate doses of **ZnPP**, thereby limiting its application as an injectable drug. [Iye07] An approach to overcome this limitation employs a styrene-maleic acid copolymer carrier system which has a much higher loading capacity. This potential carrier system for hydrophobic photosensitizers is investigated in the next chapter.

8 Block-copolymer micellar carriers: SMA-ZnPP

8.1 Introduction

Polymeric micelles have been emerging as a convenient carrier system for hydrophobic photosensitizers. [Zha03a, Gil04, Reg07a] They are formed in aqueous solutions from amphiphilic copolymers. The hydrophobic segments of the copolymer form the core of the micelle and the hydrophilic units form the corona. Polymeric micelles have a clear advantage over micelles assembled by low molecular weight surfactants. They have a higher stability reflected in a low critical micelle concentration (CMC). This means that polymer micelles are resistant to dilution effects upon administration into the blood stream. [Nos04]

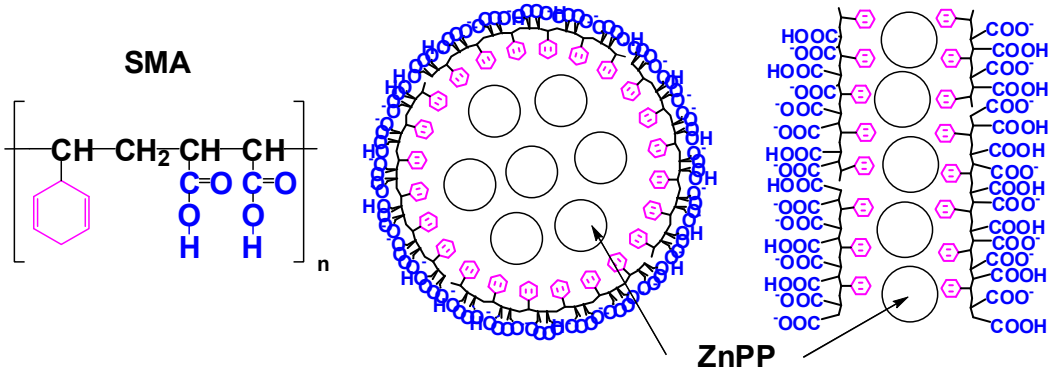

Figure 33. Chemical structure of styrene-maleic acid (SMA) and suggested micellar structures of **SMA-ZnPP** in H_2O.

Many polymers have been considered as micellar building blocks among them poly(lysine), poly(argine), polyacrylic acid and polysaccharides but the most promising results were obtained with styrene-maleic-acid (SMA) copolymer especially [Akh06]. The SMA monomer consists of a hydrophobic styrene moieties covalently coupled to a hydrophilic maleic acid unit. The molecular weight of the monomer is about 220 Dalton. [Gre05] (See Figure 33) The polymer used in this work has an average chain length of 6-7 repeating units of monomer [Mae85,Gre04] and forms micelles at a CMC of 4mg/ml. SMA was firstly synthesized in 1985 to improve the pharmacological properties of the anticancer protein neocarzinostatin (NCS). [Mae85] It was found that the copolymer-protein conjugate SMANCS showed exceptional higher antitumor activity against a variety of aggressive metastatic cancer types in humans [Mae01b] compared to NCS alone. The therapeutic advancement of the macromolecular SMA carrier is not only based on selective accumulation in the tumor tissue

due to the EPR-effect but also on other properties. The SMA shell can attach noncovalently to albumin, the most biocompatible macromolecule. The albumin serves as a secondary carrier which aids the EPR effect. Furthermore, it was shown that SMA potentiates the host immune response. [Gre04] It was reported that drug loading of the SMA shell can achieve values of up to 50% (MW drug / MW shell). In addition, the amphiphilic nature of SMA enables a range of formulation possibilities, including intravenous injection, interaarterial or oral administration.

For the aforementioned reasons the SMA copolymer is regarded also as a suitable carrier system for PDT. An example for such a photosensitizer-copolymer aggregate is **SMA-ZnPP** which is investigated throughout this chapter. It consists of SMA copolymer incorporating the hydrophobic photosensitizer ZnPP in a non-covalent manner.

Figure 33 depicts possible conformations of **SMA-ZnPP** in aqueous solution. Whether the SMA-shell assembles in a tubular or spherical structure is completely known. It is assumed that the styrene units of the SMA polymer noncovalently interact with hydrophobic segments of the host molecules whereas the hydrophilic maleic acid mojeties protonate water molecules and generate a local cationic charge of the surface of the SMA shell. The size of a single micelle depends on the incorporated compound and drug loading and ranges between 100-200nm [Mae06, Iye07]

8.2 Photophysical characterization

8.2.1 Steady-state absorption spectra

The absorption spectrum of **SMA-ZnPP** in H_2O composes of the absorption of the **ZnPP** photosensitizer and a contribution of the SMA copolymer. The Soret band of **ZnPP** is located at 391nm and its Q_x, Q_y transitions can be identified in the yellow region of the visible spectrum centered at 556nm and 588nm, respectively. In contrast to polyethylene glycol (PEG), the styrene-maleic acid copolymer has absorption bands above 200nm. The absorption of the pure, highly water-soluble SMA polymer is depicted in Figure 34 showing a steep increase at 225nm and a shoulder positioned at 259nm.

The origin of this UV band system can be identified by a closer look on the structure of the polymer. SMA consists of a hydrophobic styrene moiety and a hydrophilic maleic acid unit. The covalent coupling between both parts requires the cleavage of the double bond of styrene. As a result the hydrophobic unit of the SMA polymer is structurally similar to toluene. (See Figure 33) This methylated derivate of aromatic benzene, has its longest wavelength

absorption band at 262nm in cyclohexane (ε = 2864 $M^{-1}cm^{-1}$) and shows a steep increase in the absorbance at 225nm equal to the SMA copolymer. [Du98] From the absorption spectrum of the polymer it is apparent that an S_1-S_1 energy transfer from the excited **ZnPP** moiety to the polymer is impossible. The reason is the high lying first excited singlet state of toluol (4.7eV) which is much higher than the S_1 state of **ZnPP** (2.1eV) as estimated from absorption spectra. Transfer processes involving the first excited triplet state of the SMA polymer are also unlikely as the triplet state energy of toluene is about 3.5eV. [Haa73]

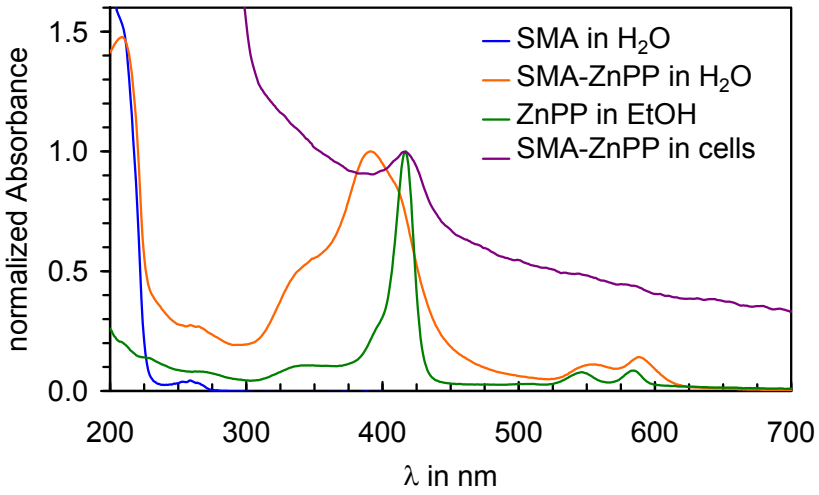

Figure 34. Normalized absorption spectra of **SMA-ZnPP** in H_2O and in Jurkat cell suspension. For comparison the spectrum of **ZnPP** in ethanol and the SMA polymer is also shown.

The Soret-band of **SMA-ZnPP** in H_2O shows a strong broadening and a large hypsochromic shift of about 26nm in comparison to **ZnPP** in EtOH. The Q-bands are heavily pertubed which is visible in the change of their relative amplitudes in addition to the observed redshift with respect to free **ZnPP**. These spectral features point out appreciable intermolecular interactions among aggregated **ZnPP** molecules within the SMA copolymer micelle. According to exciton theory a strong blueshift indicates a prevalent perpendicular alignment (head-to-head) of participating dipole moments. Such H-type aggregates have been observed for many other porphyrin systems in aqueous solution and micellar media too. [Tog04, Eic00,Kha99,Mai98]

The perturbation of electronic states observed for **SMA-ZnPP** is more pronounced than for **PEG-ZnPP**. Therefore it is supposed that the **ZnPP** molecules are packed more densely in the hydrophobic inner core of the SMA block copolymer micelle allowing stronger interactions compared to the self-assembled **PEG-ZnPP** molecules.

The uptake of **SMA-ZnPP** by Jurkat cells, a leukaemia cell line, is significantly higher than **PEG-ZnPP**. This result, discussed in section 8.4 in detail, allowed obtaining an absorption spectrum of **SMA-ZnPP** within tumor cells for the highest incubation concentration studied (5µM ZnPP equivalent). The absorption spectrum of **SMA-ZnPP** in cells is shown in Figure 34 and exhibits a strong scattering background caused by the cell suspension. Although the Q-bands attributed to zinc protoporphyrin cannot be clearly identified for **SMA-ZnPP** in cells owing to the low intracellular concentration in the nanomolar range, the peak wavelength of the Soret band can be estimated. The Soret band has its maximum at 418nm close to the value obtained for monomeric **ZnPP** in ethanol. From this observation, it can be assumed that the SMA micelle release free **ZnPP** molecules from their inner cores after being uptaken by Jurkat cells.

8.2.2 Steady-state fluorescence

The fluorescence of **SMA-ZnPP** and reference compounds were measured by excitation of the samples at 550nm, the optical density was adjusted to 0.2 at this wavelength. The fluorescence of this compound is strongly quenched compared to free **ZnPP** in ethanol. The fluorescence quantum yield of **SMA-ZnPP** was determined to Φ_F=0.003. For **ZnPP** in EtOH and **PEG-ZnPP** values of Φ_F=0.040 and Φ_F=0.008 have been determined in that order. The fluorescence of **SMA-ZnPP** is quenched to 7% of the value obtained for **ZnPP** in EtOH. As a consequence the signal was very weak which is visible in the much higher noise level associated with the measurement of the fluorescence spectrum.

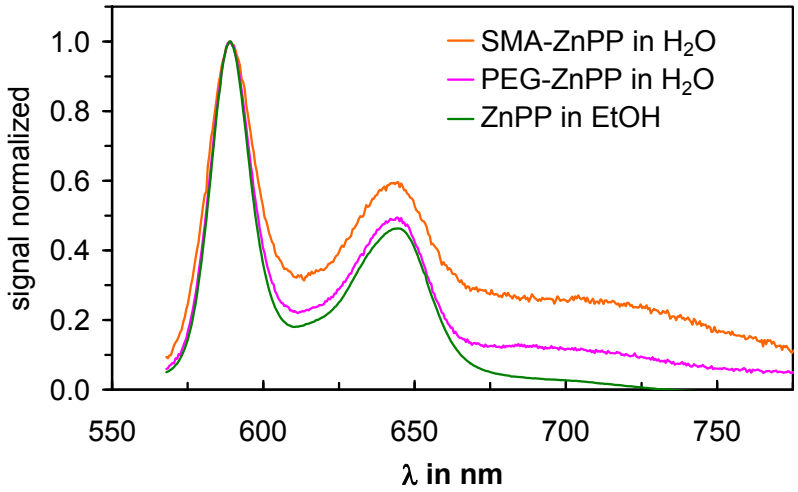

Figure 35. Normalized fluorescence spectrum of **SMA-ZnPP** in H_2O. For comparison the spectrum of **PEG-ZnPP** in H_2O and **ZnPP** in ethanol are also shown.

Besides the low Φ_F of **SMA-ZnPP**, the spectrum is extensively broadened compared to free **ZnPP** in EtOH and even **PEG-ZnPP** in H_2O. Futhermore the relative intensity of the fluorescence band at 644nm increases whereas the position of the fluorescence band maxima remains unchanged. The observed spectral features are attributed to tight aggregation of **ZnPP** molecules within the inner core of the SMA micelle as already indicated by absorption spectra.

8.2.3 Time-resolved fluorescence

The fluorescence lifetimes of **SMA-ZnPP** in H_2O and reference compound **ZnPP** in EtOH were determined by time-correlated single photon counting technique (TCSPC). The samples were excited at 400nm using the frequency doubled pulses of a Ti:Sa laser. For reduction of the aforementioned photobleaching of **ZnPP** by singlet oxygen, the samples were flushed with N_2 for 40min prior to measurement. The fluorescence was detected at the intensity maximum of the fluorescence band at 589nm.

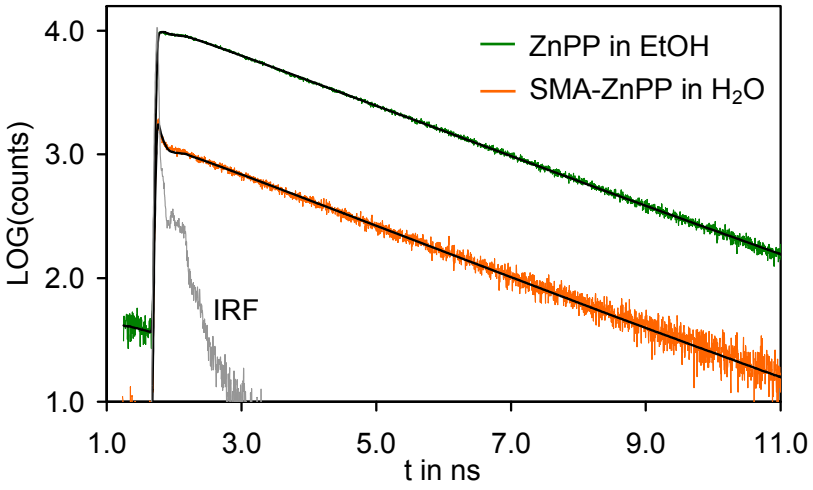

Figure 36. Time-resolved fluorescence emission decay curves of **ZnPP** in EtOH and **SMA-ZnPP** in H_2O. The FWHM of the instrument response function was determined to 80ps.

The measured fluorescence decay of **SMA-ZnPP** in H_2O was fitted by a two-exponential function which yielded a good chi-square value of 1.3. The fit exhibits a fast process with a decay time of τ_{Short}=0.06ns and a dominant amplitude of 63% in addition to a long component of τ_{long}=2.04ns with a lower amplitude of 37%. For **ZnPP** in EtOH the measurement showed two components with τ_{Short}=0.15ns (11%) and τ_{long}=2.09ns (89%) as aforementioned in

section 7.2.3. The long fluorescence lifetime component of **ZnPP** is attributed to monomeric **ZnPP** whereas the short component refers to the aggregated species. The similar long lifetime of **ZnPP** in EtOH and **ZnPP** enclosed in the polymeric SMA micelle in H_2O shows that the first excited state of **ZnPP** is not influenced by the environment to great extent. This notion is supported also by the unchanged peak position of the fluorescence emission band for the compounds under study. The amplitude of the short fluorescence decay time of **SMA-ZnPP** in H_2O is much higher than observed for **ZnPP** in EtOH and **PEG-ZnPP** in H_2O pointing out the strongly confined aggregation state of **ZnPP** within the SMA polymer micelle. This result is also reflected in the short fluorescence lifetime itself which decreases from 0.15ns to 0.13ns and 0.06ns for **ZnPP** in EtOH, **PEG-ZnPP** in H_2O and **SMA-ZnPP** in H_2O, respectively. The strong reduction of the fluorescence lifetime is caused by the enhanced non-radiative processes of aggregated **ZnPP** molecules quickly depopulating the first excited singlet state. The non-radiative quenching rate k_{nr} deactivating the first excited state of aggregated **ZnPP** within the SMA micelle was calculated from equation (7-1). A value of $k_{nr} = 1.6\times10^{10}s^{-1}$ was found which is more than two times higher than that obtained for **PEG-ZnPP**.

8.2.4 Time-resolved singlet oxygen emission

Measurement of the time-resolved singlet oxygen emission in D_2O was performed to investigate the ability of **SMA-ZnPP** to generate singlet oxygen in solution under illumination.

The optical density of the samples was adjusted to 0.2 at the excitation wavelength of 550nm. Rose Bengal in D_2O served as reference standard (Φ_Δ=0.75). Figure 37 depicts the decay of the $^1O_2$ luminescence photosensitized by **SMA-ZnPP** in D_2O. The data for **PEG-ZnPP** are shown for comparison and have been discussed in section 7.2.4.

In contrast to **PEG-ZnPP**, the singlet oxygen generation in case of **SMA-ZnPP** is very low, and the emission decay shows a two-exponential behaviour. A fit yielded two lifetimes of 8µs and 50µs with amplitudes of 51% and 49%, respectively. The longer component of the emission is attributed to singlet oxygen, which diffused out of the micelle into the D_2O environment. The observed 50µs are comparable to the lifetime of 60µs reported in the literature for a D_2O environment.[Gor78] The shorter lifetime corresponds to singlet oxygen, which is quenched by the densely packed photosensitizer molecules within the micelle and/or the micelle-building polymer. The quantum yield of singlet oxygen generation for **SMA-ZnPP** was determined to Φ_Δ=0.05 or 5%. This is more than a factor of 17 lower than the

value obtained for free **ZnPP** in EtOH (Φ_Δ=0.88). The strong suppression of Φ_Δ may be caused by an efficient S_1 deactivation channel or by a reduction of the triplet lifetime as discussed in section 7.2.4. The laser flash photolysis measurements presented in following address this issue and more important, assess the potential of **SMA-ZnPP** to generate singlet oxygen within tumor cells.

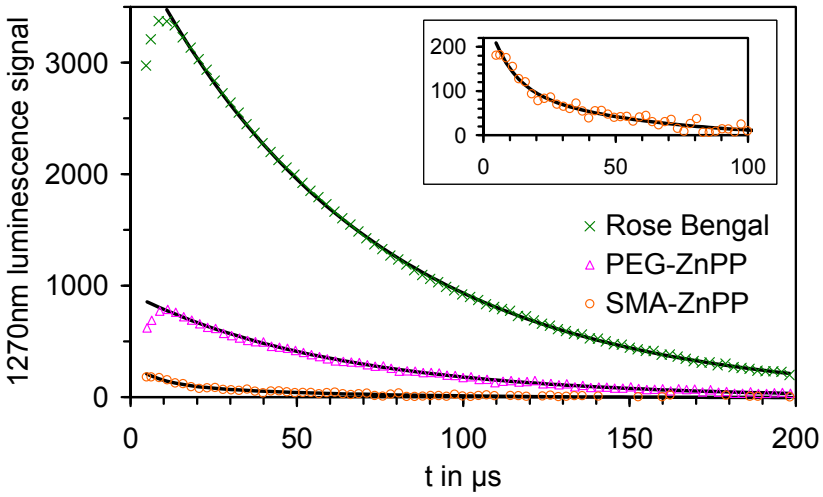

Figure 37. Time resolved singlet oxygen emission in D_2O photosensitized by **SMA-ZnPP** and **PEG-ZnPP**. Rose Bengal served as a reference standard. Inset: Magnification of the two-exponential kinetics of the singlet oxygen emission photosensitized by **SMA-ZnPP**.

8.3 Laser-flash photolysis

The method of laser flash photolysis allows indirect determination of singlet oxygen formation via triplet lifetime measurement. (See section 2.2 and 4.1.5). For **ZnPP** the triplet-triplet absorption band is located at 480nm. [Fei86]. The samples were excited at the maximum of the Soret band of ZnPP at 420nm.

8.3.1 Measurements in solution

The normalized transient absorbance change of **SMA-ZnPP** in H_2O after excitation is shown in Figure 38. In the presence of oxygen the triplet lifetime was measured to $\tau_T(O_2)$=1.4µs whereas in an environment with low oxygen concentration (through 40min N_2 flushing of the sample) the triplet lifetime of **SMA-ZnPP** dissolved in H_2O increased up to $\tau_T(N_2)$=484µs.

The strong decrease of the triplet lifetime in the presence of oxygen shows that the triplet state of **ZnPP** incorporated in the SMA polymer is quenched by molecular oxygen in solution. It further reveals that the observed reduction of the singlet oxygen quantum yield must be

attributed to a decrease of the intersystem crossing quantum yield caused by aggregation of **ZnPP** moieties within the SMA micelle.

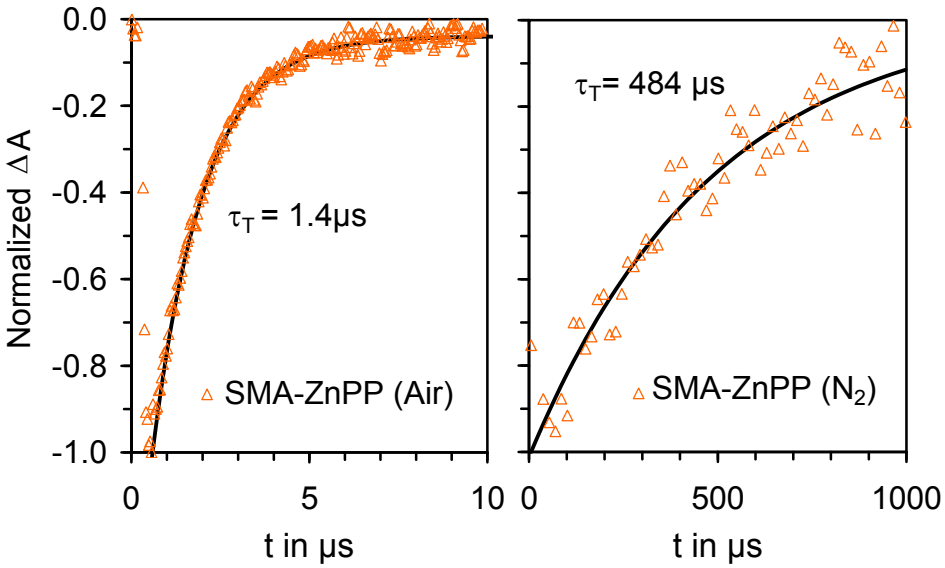

Figure 38. Laser flash photolysis of **SMA-ZnPP** in H_2O. Left: under normal air conditions. Right: after 40min N_2 flushing.

The triplet quenching rate constant $k_{EnT}[O_2]$ and the bimolecular quenching rate k_{EnT} was estimated in analogy to the calculation performed for **PEG-ZnPP** in H_2O described in section 7.3.1. Using the experimentally determined triplet lifetimes under the presence and absence of O_2, a rate constant of $k_{EnT}[O_2]= 7.1\times10^5 s^{-1}$ was found. For the bimolecular quenching rate a value of $2.4\times10^9 M^{-1}s^{-1}$ was computed which is in the range of values reported in the literature. [Sch03]

8.3.2 In vitro studies

In vitro studies on a Jurkat cells (human acute leukaemia T-cell line) were performed to question whether **SMA-ZnPP** generates singlet oxygen in tumor cells. Furthermore the influence of cellular compartments on the photosensitizing potential of **SMA-ZnPP** was investigated.

Under normal aerobic conditions a triplet lifetime of $\tau_T(O_2)$=2.4µs was measured for **SMA-ZnPP** as shown in Table 8. This value is comparable to those found for **SMA-ZnPP** in H_2O.

For **SMA-ZnPP** after 40min N_2 bubbling, a two-exponential triplet decay was observed. This finding is different compared to the one exponential decay observed for **PEG-ZnPP** as

depicted in Figure 39.

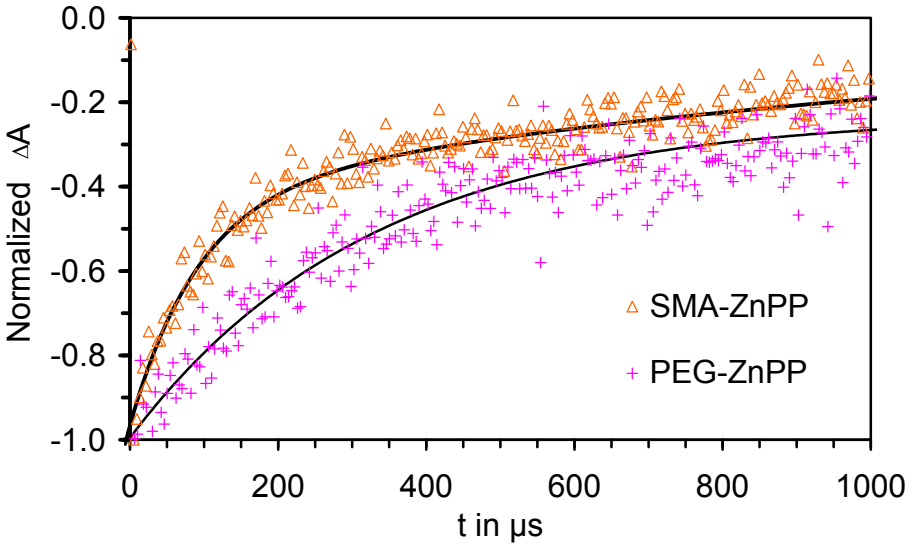

Figure 39. Laser flash photolysis of **SMA-ZnPP** in Jurkat leukaemia cells suspended in PBS after 40min N_2 flushing. The data of **PEG-ZnPP** is shown for comparison.

The short component with 127µs is significantly lower than the lifetime in H_2O under reduced oxygen concentrations. Such a strong reduction of the triplet lifetime may result from close assoziation of released **ZnPP** molecules. This type of situation occurs in hydrophobic environments like the lipid bilayer of cell membranes. Similar findings were reported by Aveline *et al* who correlated laser flash photolysis results with cellular phototoxicity data obtained under the same experimental conditions. [Ave98a, Ave98b] The observed behaviour has been attributed to weak interactions at high local concentrations of the photosensitizer and has to be distinguished from the aggregation of **ZnPP** in the core of SMA micelles. The longer component of the triplet decay with 1.2ms is attributed to a bleaching process probably resulting in the formation of long-lived radicals. For **SMA-ZnPP** in cells, either a singlet oxygen mediated phototoxicity (type II) or a free radical destruction mechanism (type I) under low oxygen concentration may occur. See section 2.2 for an overview of type I and type II photosensitization.

8.4 Cellular uptake and Phototoxicity on Jurkat leukemia cells

The cellular uptake of **SMA-ZnPP** by tumor cells and the generated phototoxicity of this compound have been studied by F. Rancan. The photobiological activity of **SMA-ZnPP** in comparison to **PEG-ZnPP** is briefly reviewed for the purpose of a combined analysis.

The intracellular uptake of **SMA-ZnPP** was studied by incubation of Jurkat cells in a growth medium containing four different **ZnPP** equivalent concentrations. The amount of photosensitizer uptaken after 24h was quantified by fluorescence measurement of the cell extract.

A more detailed description of experimental procedures underlying this investigation can be found in section 7.4 of this thesis and in reference [Reg07a].

Incubation conc. [μM]	Cellular Uptake Extract concentration [nM]		Phototoxicity Living cells in %	
	PEG-ZnPP	SMA-ZnPP	PEG-ZnPP	SMA-ZnPP
0.5	30 ± 3	6 ± 3	96 ± 3	88 ± 5
1.0	38 ± 1	33 ± 5	98 ± 5	80 ± 12
2.5	60 ± 16	149 ± 14	97 ± 2	55 ± 1
5	86 ± 10	459 ± 50	60 ± 2	2 ± 2

Table 7. Cellular uptake of **SMA-ZnPP** and **PEG-ZnPP** by Jurkat cells and generated phototoxicity under illumination.

The intracellular uptake of **SMA-ZnPP** increased with the concentration of this compound in the incubation cell suspension. It reached higher intracellular concentrations than **PEG-ZnPP** and free **ZnPP** (in terms of **ZnPP** equivalents). At an incubation concentration of 5μM, the uptake of **SMA-ZnPP** was approximately 5.4 times compared to **PEG-ZnPP**. This data can be explained by the higher **ZnPP** loading of the SMA micelle (>40% by weight) in contrast to **PEG-ZnPP** in which only 5% of the molecular weight is due to **ZnPP**. The higher uptake is also supported by the cationic surface charge of the SMA micelle mentioned in section 8.1. It has been shown previously that a negative charge of the macromolecular carrier enhances uptake by tumor cells. [Kra03]

For investigation of the phototoxicity of **SMA-ZnPP**, Jurkat cells were incubated for 24h with different concentrations of the compound. Table 7 shows the cell survival after

irradiation of the cells with a dose of 0.3J/cm^2 of UVA. Before the data is discussed it is noteworthy that less than 5% of the cells without studied compounds lost their viability after UVA expose and no cyctotoxic activity by **ZnPP** without UVA exposure was observed. [Reg07a]

Significant enhanced phototoxicity was observed for **SMA-ZnPP** at incubation concentrations higher than 1µM. The phototoxicity generated by **SMA-ZnPP** under illumination was much stronger compared to **PEG-ZnPP** which is based on the higher intracellular concentration of this compound. At the highest incubation concentration studied nearly all tumor cells were killed demonstrating the high potential of **SMA-ZnPP** for photodynamic therapy.

8.5 Conclusions

The amphiphilic styrene-maleic acid (SMA) copolymer efficiently forms micelles solubilizing the hydrophobic photosensitizer zinc protoporphyrin (**ZnPP**). The system has a remarkable high water solubility of 150mg/ml but it is insoluble in organic solvents like EtOH or DMSO. The polymeric micelles assemble with a narrow size distribution in water (mean diameter: 176.5 nm) and a molecular size of 144kDa. [Iye07] The large size is a prerequisite for EPR-effect driven tumor accumulation. For SMA micelles having similar sizes but containing conventional chemotherapeutics, e.g. doxorubicin, pirarubicin and neocarzinostatin, an EPR-effect has been observed in vivo already. [Mae01b,Gre04,Gre05]

The present photophysical characterisation was undertaken to evaluate the potential of **SMA-ZnPP** for photodynamic therapy.

Steady state absorption and fluorescence spectra demonstrate strong perturbations of the electronic system of **ZnPP** moieties enclosed in the SMA-micelle. These alterations are attributed to strong excitonic interactions among aggregated **ZnPP** molecules. Spectral analysis reveals that incorporated **ZnPP** units form H-aggregates in which the transition dipole moments of neighboring porphyrin molecules are aligned perpendicular to each other. About 40% of the molecular weight of **SMA-ZnPP** is attributed to **ZnPP** (MW: 626.03 Da) which corresponds to an average number of 92 **ZnPP** moieties per SMA-micelle. This number shows that formation of large, densily packed aggregates driven by the “hydrophobic effect” is likely to occur within the block-copolymer shell. [Cha05] The properties of such supermolecular aggregates have been investigated extensively and showed, among other things, the presence of efficient non-radiative processes, quickly depopulating the first excited singlet state resulting in reduced fluorescence quantum yield and a shortening of the

fluorescence lifetime. [Lin06, Tog04, Eic00] Indeed, time-resolved fluorescence measurements could resolve a fast process deactivating the S_1-state of the aggregated **ZnPP** moieties. The amplitude of this process is significantly higher compared to the value obtained for **PEG-ZnPP** which provides additional evidence for the higher aggregation state of the small **ZnPP** molecules in the block-copolymer micelle. The fast depopulation of the S_1-state should reduce the intersystem crossing quantum yield and the singlet oxygen quantum yield of **SMA-ZnPP**. Time-resolved singlet oxygen measurements confirmed this expectation, a very low value of Φ_Δ=0.05 in H_2O was obtained. Additional evidence for this notion is provided by the relative fluorescence quantum yield Φ_{Frel} of **SMA-ZnPP** with respect to free ZnPP. It is of similar size compared to the relative singlet oxygen quantum yield $\Phi_{\Delta rel}$ as shown in Table 8. The observation of two different singlet oxygen lifetimes points out partial quenching of singlet oxygen by the SMA polymer or by **ZnPP** molecules. There is no indication that energy- or electron transfer processes occur between **ZnPP** and aromatic styrene residues of the SMA polymer which is also unlikely from a theoretical point of view.

As it was aforementioned in section 7.5, the suppression of singlet oxygen generation is highly desirable up to the point when **SMA-ZnPP** gets internalized by tumor cells. The absorption spectrum of **SMA-ZnPP** within Jurkat leukaemia cells proved the release of **ZnPP** molecules from the micellar core after cellular uptake. The way the SMA micelle is decomposed within the cell is not completely understood. Cellular uptake is assumed to take place by endozytosis leading to enrichment of **SMA-ZnPP** in intracellular vesicles of tumor cells. It was reported that the SMA polymer is gradually liberated under mild acidic conditions. [Mae01b, Gre04] After internalization of the micelles by the cell, they are incorporated in cellular vesicles exhibiting an acidic environment. Under these conditions the decomposition of the SMA micelle may be initiated.

Laser flash measurements in solution showed that the quenching of the first excited triplet state of **SMA-ZnPP** is due to generation of singlet oxygen and that the triplet lifetime is not reduced by additional T_1 deactivation processes compared to free ZnPP. In vitro laser flash photolysis studies on Jurkat leukaemia cells containing **SMA-ZnPP** proved the intracellular generation of singlet oxygen under illumination in tumor cells. The phototoxicity is based primarily on singlet oxygen, but probably long-lived radicals are formed additionally, especially in the case of lowered oxygen concentration, such as the lipid peroxiradical ($ROO^{\cdot}$) that can cause DNA breakage or other damage.

SMA-ZnPP exhibited a five times higher cellular uptake compared to the pegylated form of

ZnPP which is attributed to higher loading and the negative charge of the surface of the SMA micelle. The phototoxicity generated by **SMA-ZnPP** is significantly higher than **PEG-ZnPP**. **SMA-ZnPP** showed a 30 fold higher phototoxicity at the highest incubation concentration studied demonstrating the advantage of the block-copolymer formulation over **PEG-ZnPP** for photodynamic therapy.

Table 8. Important photophysical properties of ZnPP and SMA-ZnPP.* JCS: Jurkat cell suspension.

Photophysical property	**ZnPP**		**SMA-ZnPP**	
Soret band maximum [nm]	417	EtOH	391 418	H_2O in JCS
Q(0,0) band maximum [nm]	584	EtOH	588	H_2O
fluorescence band maximum [nm]	589	EtOH	589	H_2O
Φ_{Frel}	1.0	EtOH	0.07	H_2O
$\Phi_{\Delta rel}$	1.0	EtOH	0.06	D_2O
τ_F [ns]	0.15 ns (11%) 2.09 ns (89%)	EtOH	0.06 ns (63%) 2.04 ns (37%)	H_2O
τ_T [µs] under normal air conditions		EtOH	1.4 ± 0.2 2.4 ± 0.2	H_2O in JCS*
τ_T [µs] after 40min N_2 flushing	280 ± 28	EtOH	484 ± 40 92 ± 11, 1200 ± 100	H_2O in JCS*

In general the SMA block-copolymer can be regarded as a very interesting delivery system for PDT. It satisfies all of the carrier related demands mentioned in Table 1. It can be used to solubilize hydrophobic photosensitizers masking their properties during delivery to tumor cells, thus reducing side effects. The micelle forming property of SMA directs macromolecularity of the assembly, a requirement for selective tumor accumulation driven by the EPR-effect. The micelle is cleaved after tumor cell uptake, releasing the photosensitizer which can display its singlet oxygen generating potential under illumination of visible light. The high payload capacity and low synthetic effort makes the carrier system especially attractive.

9. Summary

The main objective of the present thesis was the photophysical investigation of three different photosensitizer-carrier systems concerning the applicability of these macromolecules for photodynamic therapy. For this purpose steady-state and time-resolved spectroscopic measurements in the UV/VIS/NIR range had been performed on these conjugates. Experimental data, theoretical analysis and molecular-mechanical simulations allowed studying different types of intramolecular energy and electron transfer processes. In addition the generation of singlet oxygen generated by the complexes after photoexcitation had been studied in solution and *in vitro*.

Emphasis has been placed on the investigation of hexapyropheophorbide a-fullerene [C_{60}] molecular systems as representatives of modular carrier systems (MCS) excluding the addressing unit. The flexibility of the dendron system connecting the six pyropheophorbide *a* molecules among one another (**P6**) and coupling it by a malonate unit to a fullerene core (**FHP6**, **FP6**) allows a huge variety of possible conformations. This characterstic has been confirmed by molecular modelling simulations in vacuo. Because of the variety of conformations complex intramolecular interactions within these macromolecules after photoexcitations are allowed which could be identified spectroscopically. The presence of two different types of dimer energy traps (Trap I, Trap II) formed by excitonic interactions among neighboring pyropheo chromophores were observed in addition to the existance of a non-radiative deactivation channel (Trap III). In agreement with theoretical calculations, a cascade of Förster resonance energy transfers (FRET) on a picosecond time scale occurs after excitation from the initially excited chromophore. The energy is transferred from unit to unit until the energy vanishes in one of the traps or may be deactivated by fluorescence or intersystem crossing to the T_1 state of pyropheo. The trapping of excitation energy results in a reduction of the singlet oxygen quantum yield of **FHP6** and **P6** compared to free pyropheo by 2.5 fold and 4 fold, respectively, thereby limiting the potential phototoxicity of these compounds.

On the basis of a mathematical model proposed in this thesis, it was estimated that the energy from the initially excited pyropheo molecule is transferred with a probability of 54% (**FHP6**) to trap II and with a lower chance of 16% to trap I. These values are referenced to the sum of all possible trapping processes. The model further revealed that non-radiative transitions (trap III) are strongly enhanced in **P6** because of the denser folding of the macromolecule

compared to **FHP6.** These results demonstrate the influence of C_{60} on the conformation of the molecular systems and associated changes in the strength of deactivation and transfer processes. Despite the indirect influence of the fullerene, it can directly alter the photophysical properties of the attached dye molecules as well and take part in the transfer processes of the whole complex. This is best seen in compound **FP6** which contains, in contrast to **FHP6**, an electron accepting unsubstituted C_{60} fullerene core. This opens up an efficient electron transfer channel from the photoexcited pyropheo unit to the fullerene core. Electron transfer in the **FP6** molecule occurs with a probability of 67% with respect to all other trapping processes and its rate constant was determined to $k_q = 8.9\times10^9\ s^{-1}$ which is in very good agreement to value calculated by Marcus theory. The pronounced electron transfer process strongly reduces the singlet oxygen quantum yield of this compound ($\Phi_\Delta = 0.06$ in DMF), therefore **FP6** is not suitable for PDT. Instead, **FP6** can be considered as a combination of a light-harvesting system and a charge separating center. The self-assembly of sub divisions embedding different functions in the **FP6** molecule may provide new ideas for the design of artifical complexes of photosynthesis.

Among the hexapyropheophorbide a-fullerene [C_{60}] molecular systems investigated, **FHP6** is the most promising compound for PDT. In vitro studies on a Jurkat leukaemia cell line showed that **FHP6** is uptaken by tumor cells and generates sufficient phototoxicity under illumination. The water insolubility of **FHP6** may be removed through coupling of an antibody; a similar imunoconjugate exhibiting this quality has recently been investigated. [Ran07b]

Further work should be directed towards incorporation of enzyme- or pH- cleavable bonds in the MCS. In this way the photosensitizer will be released from the carrier after cellular uptake with the result that reduction of the singlet oxygen quantum yield associated with formation of energy traps can be avoided. Moreover the number of loaded dye molecules can be increased without the loss of phototoxicity, a problem observed for a MCS carrying 12 pyropheo units. [Hel05]

The water-soluble polyethylene glycol (PEG) and block-copolymer carrier systems utilize a completely different approach to enrich its payload, the photosensitizer zinc protoporphyrin (ZnPP), in the tumor tissue. Because of their molecular size being larger than 40-50kDa, they passively accumulate in the tumor due to the EPR-effect. The investigated conjugate **PEG-ZnPP** forms micelles in aqueous surroundings whereas the hydrophobic ZnPP cores loosely

aggregate in the interior of the micelle. Excitonic interactions among the dye molecules lead to the appearance of efficient S_1 deactivation channels, thus lowering the intersystem crossing and singlet oxygen quantum yield (Φ_Δ=0.17 in D_2O) of **PEG-ZnPP**. Results indicate that after tumor cell uptake, the micelle disintegrates and **PEG-ZnPP** is preserved in its monomeric form. Singlet oxygen is generated by **PEG-ZnPP** within Jurkat leukemia cells at high yields but it was found that the generated phototoxicity under illumination is only moderate. The explanation is given mainly by the low intracellular concentration of ZnPP which is based on the low transport capacity of the PEG carrier; only 5% of the molecular weight of **PEG-ZnPP** is attributed to ZnPP.

For this reason an alternative polymer carrier system for ZnPP has been investigated in this work basing on the amphiphilic styrene-maleic acid (SMA) block-copolymer. Among other advantages, **SMA-ZnPP** has a much higher loading of ZnPP (40% w/w) compared to the PEG carrier. The non-covalently incorporated ZnPP moieties form large H-aggregates within the SMA shell. As a consequence of the dense aggregation state, the singlet oxygen quantum yield of this compound (Φ_Δ=0.06 in D_2O) is reduced stronger than the suppression observed for **PEG-ZnPP** assemblies. After tumor cell uptake of **SMA-ZnPP**, the polymeric micelle is liberated and the photosensitizer is released as evidenced by absorption spectroscopy. Under illumination **SMA-ZnPP** mainly generates singlet oxygen inside cells but laser flash-photolysis measurements indicated the formation of long-lived radicals additionally (Type I mechanism), especially in the case of lowered oxygen concentration.

The tumor cell uptake of **SMA-ZnPP** is five times higher and the generated phototoxicity is 30 fold elevated with respect to **PEG-ZnPP** demonstrating the advantage of **SMA-ZnPP** over **PEG-ZnPP** for photodynamic therapy.

The investigation of the polymer carriers suggests a concept which may allow reducing skin-sensitivity and irritations of current PDT therapies. Trap formation in the hexapyropheophorbide a-fullerene [C_{60}] molecular systems as well as dense aggregation of hydrophobic photosensitizers in polymeric micelles inhibit the singlet oxygen generating potential of the attached or enclosed dye molecules. This is highly desirable as long as the complexes circulate in the blood stream of the patient and are not delivered to tumor cells. After uptake, photosensitizers will be released by their transporters and display their full photodynamic activity.

Both the modular carrier system and the polymeric micellar transporters have their specific advantages. The MCS is able to actively target single tumor cells or groups of malignant cells but it requires a higher synthetic effort compared to the micellar carriers. The latter enrich passively only in solid tumors through the EPR-effect. In general, it can be stated that polymer carrier-photosensitizer complexes will allow the development of more efficient PDT treatments under the precondition that the intramolecular transfer processes among photosensitizing molecules are selectively manipulated through the carrier system and therefore beneficially utilized.

Zusammenfassung:

Der Gegenstand der vorliegenden Arbeit ist die photophysikalische Untersuchung von drei unterschiedlichen Photosensibilisator-Transportsystemen hinsichtlich ihrer Eignung für die photodynamische Therapie. Für diese Aufgabe wurden die Komplexe mittels stationärer und zeitaufgelöster spektroskopischer Methoden im UV/VIS/NIR Spektralbereich studiert. Durch die Auswertung der experimentell gewonnenen Daten, theoretischen Rechnungen und molekül-mechanischen Simulationen konnten verschiedene Typen von intramolekularen Energie- und Elektronentransferprozessen in diesen Makromolekülen identifiziert und quantifiziert werden. Darüber hinaus wurde die Generierung von Singulettsauerstoff durch die Komplexe nach Lichtanregung sowohl in Lösung als auch *in vitro* untersucht.

Der Schwerpunkt lag auf der Untersuchung der Fulleren-Pyropheophorbid-a-Konjugate, als Repräsentanten eines Modular Carrier System (MCS) ohne Adressator. Die Flexibilität der dendritischen Gruppe, welches die 6 Pyropheophorbid-a (Pyropheo) Photosensibilisatoren untereinander verknüpft (**P6**) und über eine Malonat-Einheit an ein C_{60}-Fulleren koppelt (**FHP6**, **FP6**), erlaubt eine Vielfalt von möglichen Konformationen. Dies konnte durch molekül-mechanische Simulationen der Komplexe im Vakuum bestätigt werden. Durch die Variabilität der Konformation sind unterschiedliche photophysikalische Interaktionen nach Lichtanregung möglich, die spektroskopisch nachgewiesen werden konnten. Dazu gehören zwei verschiedene Typen von Dimer Energiesenken (Falle I, Falle II), gebildet durch exzitonische Wechselwirkungen zwischen zwei benachbarten Pyropheo Chromophoren sowie die Präsenz eines zusätzlichen nicht-strahlenden Desaktiverungskanals (Falle III). In Übereinstimmung mit theoretischen Rechnungen erfolgt nach Lichtanregung der Komplexe eine Kaskade von intramolekularen Förster-Resonanz-Energietransfers (FRET) auf der ps-

Zeitskala. Die Anregungsenergie springt von Pyropheo zu Pyropheo Chromophor bis die Anregungsenergie zufällig in einer der Fallen gefangen wird. Mit geringerer Wahrscheinlichkeit erfolgt eine Desaktivierung durch Fluoreszenz oder Intersystem Crossing (ISC) zum langlebigen T_1 Zustand von Pyropheo. Das Einfangen der Anregungsenergie durch die Dimere führt zu einer Reduktion der Singulett-Sauerstoff Quantenausbeute von **FHP6** und **P6** um das 2.5fache bzw. 4fache im Vergleich zu freiem Pyropheophorbid-a und limitiert so die Phototoxizität der Komplexe.

Auf Basis des entwickelten Modells für die Transportprozesse konnte die Effizienz der Fallen bezüglich der Desaktivierung der Anregungsenergie bestimmt werden. Vom initial angeregten Chromophor wird die Energie mit einer Wahrscheinlichkeit von 54% (**FHP6**) zur Falle II und mit einer geringeren Chance von 16% zur Falle I transportiert. (Im Vergleich zu allen möglichen Transportprozessen.) Das Modell konnte weiterhin aufzeigen, dass nichtstrahlende Übergänge (Falle III) im Molekül **P6** eine größere Rolle spielen als bei **FHP6**, verursacht durch die räumlich dichtere Konformation von **P6** im Vergleich zu **FHP6**. Diese Resultate demonstrieren den Einfluß des Fullerens auf die Konformation der Komplexe und damit verbundenen Änderungen in der Stärke der Desaktivierungs- und Transferprozesse. Abgesehen von der indirekten Einflußnahme, verändert das Fulleren auch direkt die photophysikalischen Eigenschaften der kovalent gebundenen Pyropheo Substituenten und nimmt an den Transferprozessen des Gesamtkomplexes teil. Dies ist am besten zu beobachten am Molekül **FP6**, welches im Gegensatz zu **FHP6** ein unsubstitutiertes C_{60} enthält. Das Fulleren ist ein hervorragender Elektronenakzeptor und eröffnet so einen effizienten Elektrontransfer Desaktivierungskanal vom angeregten Pyropheo zum C_{60}. Der Elektronentransfer im Molekül **FP6** erfolgt mit einer Wahrscheinlichkeit von 67% im Vergleich zu allen anderen Desaktivierungsprozessen und mit einer Ratenkonstante von $k_q = 8.9\times10^9\ s^{-1}$. Dieser Wert ist in sehr guter Überstimmung zu der theoretisch berechneten Rate auf Basis der Marcus Theorie. Der dominante Elektronentransfer bewirkt eine starke Reduktion der Singulettsauerstoffquantenausbeute ($\Phi_\Delta = 0.06$ in DMF), daher ist **FP6** nicht für die photodynamische Therapie geeignet. Stattdessen kann das Makromolekül **FP6** aufgefaßt werden, als eine Kombination aus Lichtsammelkomplex und ladungsseparierendem Zentrum. Die Selbstassoziation von molekularen Einheiten mit unterschiedlichen Funktionen im Molekül **FP6** könnte neue Ideen für das Design von künstlichen Photosynthesekomplexen liefern.

Von den untersuchten Fulleren-Pyropheophorbid-a-Konjugaten ist **FHP6** das am besten

geeignete Photosensibilisator-Carrier System für die PDT. In vitro Studien an einer Jurkat Leukämie Zelllinie konnten zeigen, das **FHP6** von Tumorzellen aufgenommen wird und eine hinreichende Phototoxizität unter Lichtanregung erzeugt. Die notwendige Löslichkeit von **FHP6** in wässigeren Umgebungen kann durch die Ankopplung eines Antikörpers erreicht werden, ein derartiges Immunokonjugat wurde kürzlich untersucht. [Ran07b]
Für weitere Arbeiten empfiehlt sich die Inkorporation von Enzym- oder pH-instabilen Bindungen in das Konzept des MCS. Durch diesen Ansatz wird der Photosensibilisator nach Aufnahme in die Tumorzelle vom Träger getrennt. Die Reduktion der Singulettsauerstoffquantenausbeute durch Energiefallen aus assoziierten Sensibilisatoren wird somit verhindert. Darüber hinaus kann die Beladung des Trägers mit Photosensibilisatoren erhöht werden, ohne dass eine Minderung der Phototoxizität zu erwarten ist. Ein solches Verhalten wurde beobachtet für ein MCS mit 12 Pyropheophorbid-a Einheiten. [Hel05]

Mit den wasserlöslichen Polyethylenglykol (PEG) und Blockcopolymer Trägersystemen wird ein anderer Weg genutzt, um den Photosensibilisator, in dieser Arbeit Zink-Protoporphyrin (ZnPP), im Tumor anzureichern. Aufgrund des hohen Molekulargewichtes von über 40-50kDa, akkumulieren diese Systeme im Tumorgewebe durch den EPR-Effekt. Das untersuchte Konjugat **PEG-ZnPP** bildet Mizellen in wässiger Umgebung, wobei die hydrophoben ZnPP Kopfgruppen im Interior der Mizelle aggregieren. Exzitonische Wechselwirkungen zwischen den ZnPP Farbstoffmolekülen führen zu effizienten S_1-Desaktivierungskanälen, die die Intersystem-Crossing- und Singulettsauerstoffquanten-ausbeute ($\Phi_\Delta = 0.17$ in D_2O) reduzieren. Die Ergebnisse weisen darauf hin, dass die Aggregate nach Aufnahme in die Tumorzelle ihre Integrität verlieren und **PEG-ZnPP** vorwiegend monomer vorliegt. In Konsequenz wird Singulettsauerstoff unter Lichteinwirkung effizient von **PEG-ZnPP** in der Tumorzelle generiert, jedoch ist die beobachtete Phototoxizität gering. Die Erklärung liegt in der niedrigen intrazellulären Konzentration von ZnPP, eine Folge der geringen Transportkapazität des PEG Carriers. Nur etwa 5% des Molekulargewichts von **PEG-ZnPP** entfallen auf den Photosensibilisator. Um diesen Nachteil zu umgehen, wurde ein alternatives Transportsystem auf Basis eines Styren-Maleinsäure (SMA) Copolymers in Betracht gezogen. Neben anderen Vorteilen, erlaubt das Copolymer eine wesentliche höhere Beladung mit ZnPP, so entfallen 40% des Molekulargewichts auf den Photosensibilisator im Falle von **SMA-ZnPP**. In wässriger Umgebung sind die ZnPP Sensibilisatoren nichtkovalent in der SMA Mizelle eingeschlossen.

Durch die hydrophobe Wechselwirkung lagern sich die ZnPP Einheiten zusammen und bilden große Aggregate innerhalb der SMA Hülle. Durch den hohen Aggregationszustand ist die Singulettsauerstoffquantenausbeute ($\Phi_\Delta = 0.06$ in D_2O) von **SMA-ZnPP** stärker reduziert im Vergleich zu **PEG-ZnPP**. Absorptionsexperimente zeigten, das nach Aufnahme von **SMA-ZnPP** in die Tumorzelle, die mizellare Struktur zerstört und der Photosensibilisator in monomerer Form freigesetzt wird. Somit wird nach Lichtanregung effizient Singulettsauerstoff generiert. Die Laserflashphotolyse Messungen deuten darauf hin, das auch langlebige Radikale entstehen, insbesondere unter Bedingungen reduzierter Sauerstoffkonzentrationen. Die Aufnahme von **SMA-ZnPP** in die Tumorzelle ist 5-fach höher und die erzeugte Phototoxizität unter Lichteinwirkung ist 30-fach höher im Vergleich zu **PEG-ZnPP**. Aus den bisherigen Betrachtungen folgt, dass **SMA-ZnPP** für den Einsatz in der photodynamischen Therapie wesentlich besser geeignet ist als **PEG-ZnPP**.

Die Untersuchung der verschiedenen Photosensibilisator-Transportsysteme weist auf ein Konzept hin, welches geeignet scheint, Nebenwirkungen derzeitiger PDT-Konzepte zu reduzieren. Die Bildung von Energiefallen in den Fulleren-Pyropheophorbid-a-Konjugaten wie auch die starke Aggregation hydrophober Photosensibilisatoren in den Blockcopolymer Mizellen unterdrückt das Potential der Komplexe Singulettsauerstoff zu generieren. Dieses Verhalten ist wünschenswert so lange die Makromoleküle im Blut des Patienten zirkulieren und noch nicht im Tumor lokalisiert sind. Erst nach der Aufnahme in die Tumorzellen werden die Photosensibilisatoren freigesetzt und können nach Lichtanregung photodynamische Aktivität entwickeln.

Sowohl das Modulare Carrier System (MCS) als auch die hier untersuchten mizellaren Transportsysteme besitzen ihre spezifischen Vorteile. Das MCS ist durch aktives Targeting befähigt, Photosensibilisatoren auch in vereinzelten Tumorzellgruppen (Metastasen) anzureichern. Dafür ist der synthetische Aufwand höher als bei den vorgestellten polymeren Trägern. Diese erlauben die passive Anreicherung der Sensibilisatoren im Tumor durch den EPR-Effekt, welcher nur in größeren Tumoren wirksam ist.
In der Zusammenfassung erlauben Photosensibilisator-Carrier Transportsysteme die Entwicklung effizienter photodynamischer Therapien unter der Voraussetzung, das die intramolekularen Transferprozesse zwischen den Photosensibilisatoren durch geeignete Wahl des Transportsystems gezielt beeinflußt und somit genutzt werden können.

10. References

[Aav84] Aaviksoo J., Freiberg A., Savikhin S., Stelmakh G. F., Tsvirko M.P., Picosecond fluorescence study of the lifetimes of metalloporphyrin S_1 and S_2 states, Chemical Physics letters, 111, 1984, 275-278

[Akh06] Akhtar S., Non-viral cancer gene therapy: Beyond delivery, Gene Therapy, 13, 2006, 739–740

[All04] Allison, R. R., Downie G. H., Cuenca R., Hu X. H., Childs C. J. H., Sibata C. H., Photosensitizers in clinical PDT, Photodiagnosis and Photodynamic Therapy 1, 2004, 27-42

[And02] Andersen L. K., Gao Z., Ogilby P. R., Poulsen L., Zebger I., A Singlet Oxygen Image with 2.5µm Resolution, Journal of Physical Chemistry A 106, 2002, 8488-8490

[Aub95] Aubry J. M., Mandard-Cazin B., Rougee M., Bensasson R. V., Kinetic Studies of Singlet Oxygen [4+2]-Cycloadditions with Cyclic 1,3-Dienes in 28 Solvents, Journal of the American Chemical Society 117, 1995, 9159-9164

[Ave98] Aveline, B., Sattler, R., Redmond, R., Environmental effects on cellular photosensitization: Correlation of Phototoxicity Mechanism with Transient Absorption Spectroscopy Measurements. Photochemistry and Photobiology, 68, 1998, 51-62

[Ave98a] Aveline B., Sattler R., Redmond R., Environmental effects on cellular photosensitization: correlation of phototoxicity mechanism with transient absorption spectroscopy measurements. Photochemistry and Photobiology 68, 1998, 51-62

[Ave98b] Aveline B., Redmond B., Can cellular phototoxicity be accurately predicted on the basis of sensitizer photophysics?, Photochemistry and Photobiology 69, 1998, 306-316.

[Avo77] Avouris P., Gelbart W. M., El-Sayed, Nonradiative Electronic Relaxation under Collision-Free Conditions, Chemical Reviews 77, 1977, 793-831

[Bak92] Baker, A., Kanofsky J. R., Quenching of singlet oxygen by biomolecules from L1210 leukemia cells. Photochemistry and Photobiology 55, 1992, 523–528

[Bar84] Barboy N., Feitelson J., Excited-State Electron-Transfer Reactions of Zinc Octaethylporphyrin, Journal of Physical Chemistry 88, 1984, 1065-1068

[Bat01] Battah S. H., Chee C.-E., Nakanishi H., Gerscher S., MacRobert A. J., Edwards C., Synthesis and Biological Studies of 5-Aminolevulinic Acid-Containing Dendrimers for Photodynamic Therapy, Bioconjugate Chemistry 12, 2001, 980-988

[Bel06] Bellnier D. A., Greco W. R., Nava H., Loewen G. M., Oseroff A. R., Dougherty T. J., Mild skin photosensitivity in cancer patients following injection of Photochlor (2-[1-hexyloxyethyl]-2-devinyl pyropheophorbide-a; HPPH) for photodynamic therapy, Cancer Chemotherapy and Pharmacology 57, 2006, 40-45

[Ber05] Berg K., Selbo P. K., Weyergang A., Dietze A., Prasmickaite L., Bonsted A., Engesaeter B., Angell-Petersen E., Warloe T., Frandsen N. , Hogset A., Porphyrin-related photosensitizers for cancer imaging and therapeutic applications, Journal of Microscopy 218, 2005, 133–147

[Bir70] Birks J. B., Photophysics of Aromatic Molecules, John Wiley & Sons, 1970

[Bis99] Bisland S. K., Singh D., Garie J., Potentiation of Chlorin e6 Photodynamic Activity in Vitro with Peptide-Based Intracellular Vehicles, Journal of Bioconjugate Chemistry 10, 1999, 982-992

[Bon95] Bonnett R., Photosensitizers of the Porphyrin and Phthalocyanine Series for Photodynamic Therapy, Chemistry Society Reviews 24, 1995, 19 – 33

[Bou95] Boudon C., Gisselbrecht J.-P., Gross M., Isaacs L., Anderson H. L., Faust R., Diederich F., Electrochemistry of Mono- through Hexakis-adducts of C_{60}, Helvetica Chimica Acta 78, 1995, 1334-1344

[Cap03] Capella, M. A. M., Capella L. S., Light in Multidrug Resistance: Photodynamic Treatment of Multidrug-Resistant Tumors, Journal of Biomedical Science 10, 2003, 361–366

[Car01] Carcenac M., Dorvillius M., Garambois V., Glaussel F., Larroque Ch., Langlois R., Hynes N. E., van Lier J. E., Pèlegrin A., Internalisation enhances photo-induced cytotoxicity of monoclonal antibody-phthalocyanine conjugates, British Journal of Cancer 85, 2001, 1787-1793

[Cha05] Chandler D., Interfaces and the driving force of hydrophobic assembly, Nature 437, 2005, 640-647

[Chi81] Chibisov, A. Electron Transfer in Photochemical Reactions, Russian Chemistry Reviews 50, 1981, 615-629

[Con84] O'Connor D., Philips D., Time-corelated Single Photon Counting, Academic Press, London, 1984

[Cox82] Cox G. S., Whitten D. G., Mechanisms for the Photooxidation of Protoporphyrin IX in Solution, Journal of the American Chemical Society, 104, 1982, 516-521

[Dav62] Davydov A. S., Theory of Molecular Excitons, McGraw Hill Book Company, New York, 1962

[De98] De A. K., Sinha S., Nandy S. K., Ganguly T. , Effects of protic and aprotic solvents on quenching mechanisms involving dimethyl-substituted donors and tetracyanoquinodimethane (TCNQ), Journal of the Chemical Society Faraday Transactions 94, 1998, 1695-1700

[Der04] Derycke A. S. , Kamuhabwa A., Gijsens A., Roskams T., De Vos D., Kasran A., Huwyler J., Missiaen L., de Witte P. A., Transferrin-conjugated liposome targeting of photosensitizer AlPcS[4] to rat bladder carcinoma cells, Journal of the National Cancer Institute 96, 2004, 1620-1630.

[Dic05] Dichtel W. R., Hecht S., Fréchet J. M. J., Functionally Layered Dendrimers: A New Building Block and its Application to the Synthesis of Multichromophoric Light Harvesting Systems, Organics Letters 7, 2005, 4451-4454.

[Dol02] Dolmans D. E., Kadambi A., Hill J. S., Waters C. A., Robinson B. C., Walker J. P., Fukumura D., Jain R. K.,Vascular accumulation of a novel photosensitizer, MV6401, causes selective thrombosis in tumor vessels after photodynamic therapy., Cancer Research 62, 2002, 2151-2156.

[Dol03] Dolmans D. E. J. G. J., Fukumura D., Jain R. K., Photodynamic therapy for cancer, Nature Reviews Cancer 3, 2003, 380-387

[Don04] van Dongen G. A. M. S., Visser G. W. M.,Vrouenraets M. B., Photosensitizer-antibody conjugates for detection and therapy of cancer, Advanced Drug Delivery Reviews 56, 2004, 31-52

[Dou98] Dougherty T. J., Gomer C. J., Henderson B. W., Jori G., Kessel D., Korbelik M., Moan J., Peng Q., Photodynamic Therapy, Journal of the National Cancer Institute 90, 1998, 889-905

[Du98] Du H., Fuh R. A., Li J., Corkan A., Lindsey J. S., PhotochemCAD: A computer-aided design and research tool in photochemistry, Photochemistry and Photobiology, 68, 1998, 141-142

[Dun06] Duncan R., Polymer conjugates as anticancer nanomedicines, Nature Reviews Cancer 6, 2006, 688-701

[Eat88] Eaton D. F., Reference Materials for Fluorescence Measurement, Pure & Applied Chemistry 60, 1988, 1107-1114

[Eic00] Eichwurzel I., Stiel H., Röder B., Photophysical studies of pheophorbide a dimers, Journal of Photochemistry and Photobiology B 54, 2000,124-200.

[Erm04a] Ermilov E. A., Al-Omari S., Helmreich M., Jux N., Hirsch A., Röder B., Photophysical properties of fullerene-dendronpyropheophorbide supramolecules, Chemical Physics 301, 2004, 27-31

[Erm04b] Ermilov E. A., Al-Omari S., Helmreich M., Jux N., Hirsch A., Röder B., Steady-state and time-resolved studies on the photophysical properties of fullerene-pyropheophorbide a complexes in polar and nonpolar solvents, Optics Communications 234, 2004, 245-252

[Erm05] Ermilov E. A., Hackbarth S., Al-Omari S., Helmreich M., Jux N., Hirsch A., Röder B., Trap formation and energy transfer in the hexapyropheophorbide a – fullerene C_{60} hexaadduct molecular system, Optics Communication 250, 2005, 95-104

[Erm06] Ermilov E. A., Tannert S., Werncke T., Choi M. T. M., Ng D. K. P., Röder B., Photoinduced electron and energy transfer in a new porphyrin–phthalocyanine triad, Chemical Physics 328, 2006, 428–437

[Erm07] Ermilov E.A., Helmreich M., Jux N., Röder B., Novel Pyropheophorbide Fullerene conjugates as part of Modular Carrier Systems in PDT and as promising units in Artificial Photosynthesis, Chemical Physics Research Trends Horizons in World Physics, B.V. Arnold (Ed.), Nova Science Publishers, Vol. 252, 2007, 215-246

[Fan03] Fang J., Sawa T., Akaike T., Akuta T., Sahoo S.K., Greish K., Hamada A., Maeda H., In Vivo Antitumor Activity of Pegylated Zinc Protoporphyrin: Targeted Inhibition of Heme Oxygenase in Solid Tumor., Cancer Research, 63, 2003, 3567-3574

[Fan04] Fang J., Sawa T., Akaike T., Greish K., Maeda H., Enhancement of Chemotherapeutic Response of tumor cells by a heme oxygenase inhibitor, pegylated zinc protoporphyrin. Internal Journal of Cancer 109, 2004, 1-8

[Fei82] Feitelson J., Mauzerall D., Reactions of Triplet States of a Porphyrin Measured by Delayed Fluorescence, Journal of Physical Chemistry, 86, 1982, 1623-1628

[Fei86] Feitelson J., Barboy N., Triplet-State Reactions of Zinc Protoporphyrins, Journal of Physical Chemistry, 90, 1986, 271-274

[Fer07] Ferlay J., Autier P., Boniol M., Heanue M., Colombet M., Boyle P., Estimates of the cancer incidence and mortality in Europe in 2006, Annals of Oncology, 2007, doi:10.1093, published online

[Fle76] Fleming G. R., Morris J. M., Robinson G. W., Direct Observation of the Rotational Diffusion by Picosecond Spectroscopy, Chemical Physics, 17, 1976, 91-100

[Fle77] Fleming G. R., Knight A. W. E., Morris J. M., Morrison R. J. S., Robinson G. W. , Picosecond Fluorescence Studies of Xanthene Dyes, Journal of the American Chemical Society, 99, 1977, 4306-4311

[Foo91] Foote, C. S., Definition of Type I and Type II photosensitized oxidation, Photochemistry and Photobiology 54, 1991, 659

[För48] Förster T., Zwischenmolekulare Energiewanderung und Fluoreszenz, Annalen der Physik 2, 1948, 55-75

[Gag80] Gagne R. R., Koval C. A., Lisensky G. C., Ferrocene as an internal standard for electrochemical measurements, Inorganic Chemistry 19, 1980, 2854-2855

[Gan83] Gandin E., Lion Y., Van de Vorst A., Quantum yield of singlet oxygen production by xanthene derivatives., Photochemistry and Photobiology, 37, 1983, 271

[Gil04] Gillies E. R., Fréchet J. M. J., Development of acid-sensitive copolymer micelles for drug delivery, Pure and Applied Chemistry 76, 2004, 1295–1307

[Gol04] Gollnick S. O., Kabingu E., Kousis P. C., Henderson B. W., Stimulation of the host immune response by photodynamic therapy (PDT), Proceedings of SPIE 5319, 2004, 60-70

[Gor78] Gorman, A., Rodgers, M., Lifetime and reactivity of singlet oxygen in an aqueous micellar system: A pulsed nitrogen laser study., Chemical Physics Letters, 55, 1978, 52-54

[Gou90] Gould I. R., Ege D., Moser J. E., Farid S., Efficiencies of photoinduced electron-transfer reactions: role of the Marcus inverted region in return electron transfer within geminate radical-ion pairs, Journal of the American Chemical Society 1990, 112, 4290-4301

[Gou91] Gould I. R., Young R. H., Moody R. E., Farid S., Contact and solvent-separated geminate radical ion pairs in electron-transfer photochemistry, Journal of Physical Chemistry 95, 1991, 2068-2080

[Gra05] Gray H. B., Winkler J. R., Long-range electron transfer, Proceedings of the National Academy of Sciences 102, 2005, 3534-3539

[Gra98] W. B. Gratzer, Medical Research Council Labs, Holly Hill, London

[Gre03] Greish K., Fang J., Inutsuka T., Nagamitsu A, Maeda H., Macromolecular therapeutics: Advantages and prospects with special emphasis on solid tumour targeting, Clinical pharmacokinetics 42, 2003, 1089-1105

[Gre04] Greish K., Sawa T., Fang J., Akaike T., Maeda H., SMA–doxorubicin, a new polymeric micellar drug for effective targeting to solid tumours, Journal of Controlled Release, 97, 2004, 219– 230

[Gre05] Greish K., Nagamitsu A., Fang J., Maeda H.,Copoly(styrene-maleic acid)-Pirarubicin Micelles: High Tumor-Targeting Efficiency with Little Toxicity, Bioconjugate Chemistry, 16, 2005, 230-236

[Gua93] Guarr T. F., Meier M. S., Vance V. K., Clayton M., Electrochemistry of the $C_{60}H_2$ fullerene, Journal of the American Chemical Society 115, 1993, 9862-9863

[Haa06] Haag R., Kratz F., Polymer Therapeutics:Concepts and Applications, Angewandte Chemie International Edition 45, 2006, 1198-1215

[Haa73] Haaland D. M., Nieman G. C., Toluene: Phosphorescence spectrum and distortion in the triplet state, Journal of Chemical Physics, 59, 1973, 4435-4457

[Haa86] Haag W. R., Hoigne J., Singlet Oxygen in Surface Waters. 3. Photochemical Formation and Steady-State Concentrations in Various Types of Waters, Environmental Science & Technology 20, 1986, 341-348

[Hac05] Hackbarth S., Ermilov E. A., Röder B., Interaction of Pheophorbide a molecules covalently linked to DAB dendrimers, Optics Communications, 248, 2005, 295-306

[Hal00] van Hal P. A., Knol J., Langeveld-Voss B. M. W., Meskers S. C. J., Hummelen J. C., Janssen R. A. J., Photoinduced Energy and Electron Transfer in Fullerene-Oligothiophene-Fullerene Triads, Journal of Physical Chemistry A 104, 2000, 5974-5988

[Hal73] Hale G. M., Querry M. R., Optical constants of water in the 200nm to 200µm wavelength region, Applied Optics 12, 1973, 555-563

[Ham01] Hamblin M. R., Miller J. L., Rizvi I., Ortel B., Maytin E. V., Hasan T., Pegylation of a $Chlorin_{e6}$ Polymer Conjugate Increases Tumor Targeting of Photosensitizer, Cancer Research 61, 2001, 7155–7162

[Ham03] Hamblin M. R., Miller J.L., Rizvi I., Loew H.G., Hasan T., Pegylation of charged polymer-photosensitiser conjugates: effects on photodynamic efficacy, British Journal of Cancer 89, 2003, 937 – 943

[Has89] Haseloff R., Ebert B., Röder B., Generation of free radicals by photoactivation of pheophorbide a, HP and PP, Journal of Photochemistry and Photobiology B: Biology 3, 1989, 593-602

[Hel04] Helmreich M., Ermilov E., Rancan F., Böhm F., Röder B., Hirsch A., Jux N., Synthesis and photophysics of fullerene-dendrimer-pyropheophorbide-conjugates, Journal of Porphyrins and Phthalocyanines 8, 2004, 689

[Hel05] Helmreich M., Ermilov E. A., Meyer M., Jux N., Hirsch A., Röder B., Dissipation of Electronic Excitation Energy within a C60 [6:0]-Hexaadduct Carrying 12 Pyropheophorbide a Moieties, Journal of the American Chemical Society 127, 2005, 8376-8385

[Hel06] Helmreich M., Crown Ether-Metalloporphyrins as Ditopic Receptors and Pyropheophorbide-a Conjugates for the Photodynamic Therapy of Tumors, Dissertation, Erlangen, 2006

[Hel97] Helenius V., Monshouwer R., van Grondelle R., Temperature-Dependent Lifetimes and Quantum Yield of the Singlet and Triplet States of the B820 Subunit of LHI Antenna Complex of Purple Bacterium *Rhodospirillum* rubrum, Journal of Physical Chemistry B 101, 1997, 10554-10559

[Her34] Herzberg, G., Polarography of the infrared color spectrum to wavelength 12,900Å , Nature (London) 133, 1934, 759

[Hir99] Hirth A., Michelsen U., Wöhrle D., Photodynamische Tumortherapie, Chemie in unserer Zeit 2, 1999, 84-94

[Hol03] Holland J. F., Frei E., Kufe D. W., Cancer Medicine 6, Decker (Bc), 2003

[Iye07] Iyer A. K., Greish K., Fang J., Murakami R., Maeda H., High-loading nanosized micelles of copoly(styrene–maleic acid)–zinc protoporphyrin for targeted delivery of a potent heme oxygenase inhibitor, Biomaterials 28, 2007, 1871-1881

[Jem07] Jemal A., Siegel R., Ward E., Murray T., Xu J., Thun M. J., Cancer Statistics 2007, A Cancer Journal for Clinicians 57, 2007, 43–66

[Jia98] Jiang F., Lilge L., Grenier J., Li Y., Wilson M. D., Chopp M., Photodynamic therapy of U87 human glioma in nude rat using liposome-delivered photofrin, Lasers in Surgery and Medicine 22, 1998, 74 – 80

[Jos79] Joshi N. B., Gangola P., Pant, D.D., Internal heavy atom effect on the radiative and non-radiative rate constants in xanthene dyes., Journal of Luminescence, 21, 1979, 111

[Jux06] Jux N., Helmreich M., Hirsch A., Röder B., Ermilov E., Novel oligo-pyropheophorbide fullerene conjugates, Journal of Porphyrins and Phthalocyanines 10, 2006, 465

[Kal98] Kalant H., Drug solubility, absorption, and movement across body membranes, in: Kalant H., Roschlau W. H. E. (Eds.), General principles of Pharmacology, sixth ed., Oxford University Press, New York, 1998, 14-24

[Kas50] Kasha, M., Characterization of electronic transitions in complex molecules, Discussion Faraday Society. 9, 1950**,** 14-19

[Kas52] Kasha, M., Collisional Perturbation of Spin-Orbital Coupling and the Mechanism of Fluorescence Quenching. A Visual Demonstration of the Perturbation., Journal of Chemical Physics 20, 1952, 71-74

[Kas63] Kasha M., Energy Transfer Mechanisms and the Molecular Exciton Model for Molecular Aggregates, Radiation Research 20, 1963, 55-71

[Kas65] Kasha M., Rawls H.R., Ashraf El-Bayoumi M., The exciton model in molecular spectroscopy, Pure and Applied Chemistry 11, 1965, 371-392

[Kav93] Kavarnos, G. J., Fundamentals of photoinduced electron transfer, VCH Publishers Inc., USA, 1993

[Kha99] Khairutdinov R. F., Serpone N., Photoluminescence and Transient Spectroscopy of Free Base Porphyrin Aggregates, Journal of Physical Chemistry B, 103, 1999, 761-769

[Kle00] Kleima F. J., Hofmann E., Gobets B., van Stokkum I. H. M., van Grondelle R., Diederichs K., van Amerongen H., Förster Excitation Energy Transfer in Peridinin-Chlorophyll-a-Protein, Biophysical Journal 78, 2000, 344-353

[Koc96] Kochevar I. E., Lambert C. R., Lynch M. C. , Tedesco A. C., Comparison of photosensitized plasma membrane damage caused by singlet oxygen and free radicals. Biochimica et Biophysica Acta 1280, 1996, 223-230

[Kor98] Korth O., Hanke T., Röder B., Photophysical investigations of pheophorbide-a embedded in Langmuir-Blodgett mono- and multilayers, Thin solid films 320, 1998, 305-315

[Kra03] Krasnici S., Werner A., Eichhorn M. E., Schmitt-Sody M., Pahernik S. A., Sauer B., Schulze B., Teifel M., Michaelis U., Naujoks K., Dellian M., Effect of the surface charge of liposomes on their uptake by angiogenic tumor vessels, Internal Journal of Cancer 105, 2003, 561-567

[Kra76] Krasnovsky A. A., Photosensitized luminescence of singlet oxygen in solution. Biofizica 21, 1976, 748

[Lak99] Lakowicz J. R., Principles of Fluorescence Spectroscopy., 2nd ed., Kluwer Academic/Plenum, 1999

[Lin06] Lin J. S., Chen Y. C., Chen C. C., Diau E. W. G., Liu T.-F., Aggregation of Zinc Protoporphyrin in Anodized Aluminum Oxide (AAO) Nanoporous Environments, Journal of the Chinese Chemical Society, 53, 2006, 201-208

[Lin71] Lin S. H., Isotope effect, energy gap law and temperature effect in resonance energy transfer, Molecular Physics 21, 1971, 853-863

[Lin93] Lin S. H., Xiao W. Z., Generalized Förster Dexter Theory of photoinduced intramolecular energy transfer, Physical Review E 47, 1993, 3698-3706

[Liu69] Liu K. J., Parsons J. L., Solvent Effects on the Preferred Conformation of Poly (ethylene glycols), Macromolecules, 5, 1969, 529-533

[Lo03] Lo P., Wang S., Zeug A., Meyer M., Röder B., Ng D. K. P., Preparation and Photophysical Properties of Halogenated Silicon(IV) Phthalocyanines Substituted Axially with Poly(ethylene glycol) Chains., Tetrahedron Letters 44, 2003, 1967-1970.

[Mae00] Maeda H., Wua J., Sawa T., Matsumura Y. , Hori K., Tumor vascular permeability and the EPR effect in macromolecular therapeutics: a review, Journal of Controlled Release 65, 2000, 271-284

[Mae01a] Maeda H., The Enhanced Permeability and Retention (EPR) effect in tumor vasculature: The key role of tumor-selective macromolecular drug targeting. Advances in Enzyme Regulation 41, 2001, 189-207

[Mae01b] Maeda H., Sawa T., Konno T., Mechanism of tumor-targeted delivery of macromolecular drugs, including the EPR-effect in solid tumors and clinical overview of the prototype polymeric drug SMANCS, Journal of Controlled Release 74, 2001, 47-61

[Mae02] Maeda H., Enhanced Permeability and retention (EPR) effect: Basis for drug targeting to tumor, in Biomedical Aspect of Drug Targeting, Kluwer Publishers, 2002, 221-228

[Mae06] Maeda H., Cancer Targeting with Macromolecular Drugs Based on Unique Tumor Vascular and, SMA-Zn Protoporphyrin, presentation, Berlin, 2006

[Mae85] Maeda H., Ueda M., Morinaga T., Matsumoto T., Conjugation of Poly(styrene-co -maleic acid) Derivatives to the Antitumor Protein - Neocarzinostatin: Pronounced Improvements in Pharmacological Properties, Journal of Medicinal Chemistry 28, 1985, 455-461

[Mai98] Maiti N. C., Mazumdar S., Periasamy N., J- and H-Aggregates of Porphyrins with Surfactants, Fluorescence, Stopped Flow and Electron Microscopy Studies, Journal of Porphyrins and Phthalocyanines, 2, 1998, 369-376

[Mak06] Makarov S., Litwinski Ch., Ermilov E. A., Suvorova O., Röder B., Wöhrle D., Synthesis and Photophysical Properties of Annulated Dinuclear and Trinuclear Phthalocyanines, Chemistry – A European Journal 12, 2006,1468-1474

[Maple] Maple, Version 8, Maplesoft Inc., Ontario, Canada

[Mar84] Marcus R. A., Nonadiabatic processes involving quantum-like and classical-like coordinates with applications to non-adiabatic electron transfers, Journal of Chemical Physics 81, 1984, 4494-4500

[Mar85] Marcus R., Sutin N., Electron transfer in chemistry and biology, Biochimica et Biophysica Acta 811, 1985, 265-322

[Mat86] Matsumura Y., Maeda H. A new concept for macromolecular therapeutics in cancer chemotherapy: mechanism of tumoritropic accumulation of proteins and the antitumor agent smancs. Cancer Research 46, 1986, 6387–6392

[MatSt] Material Studio, Packages: Discover and Forcite, Version 4.0, Accelrys, Inc: San Diego, USA

[May04] Mayerhofer M., Florian S., Krauth M.T., Aichberger K.J., Bilban M., Marculescu R., Printz D., Fritsch G., Wagner O., Selzer E., Sperr W. R., Valent P., Sillaber C., Identification of heme oxygenase-1 as a novel BCR/ABL-dependent survival factor in chronic myeloid leukemia, Cancer Research, 64, 2004, 3148-54

[McR64] McRae E.G., Kasha M., Physical Processes in Radiation Biology, p. 23, Academic Press, New York, 1964

[Moa81] Moan J., Boye E., Photodynamic effect on DNA and cell survival of human cells sensitized by hematoporphyrin, Photobiochemistry and Photobiophysics 2, 1981, 301-307

[Moa90] Moan J., On the diffusion length of singlet oxygen in cells and tissues, Journal of Photochemistry and Photobiology B: Biology, 6, 1990, 343-347

[Mul32] Mullikan, R, The Interpretation of Band Spectra Part III. Electron Quantum Numbers and States of Molecules and Their Atoms, Review of Modern Physics 4, 1932, 1-86

[Mur94] Murata S., Nishimura M., Matsuzaki S. Y., Tachiya M., Transient effect in fluorescence quenching induced by electron transfer. I. Analysis by the Collins-Kimball model of diffusion-controlled reactions, Chemical Physics Letters 219, 1994, 200-206

[Nie02] Niedre M., Patterson M. S., Wilson B.C., Direct near-infrared luminescence detection of singlet oxygen generated by photodynamic therapy in cells *in vitro* and tissues *in vivo*, Photochemistry and Photobiology 4, 2002, 382–391¶

[Nis03] Nishiyama N., Stapert H. R., Zhang G.-D., Takasu D., Jiang D.-L., Nagano T., Aida T., Kataoka K., Light-Harvesting Ionic Dendrimer Porphyrins as New Photosensitizers for Photodynamic Therapy, Bioconjugate Chemistry 14, 2003, 58-66

[Nos04] van Nostrum C. F., Polymeric micelles to deliver photosensitizers for photodynamic therapy, Advanced Drug Delivery Reviews 56, 2004, 9-16

[Now01] Nowakowska M., Kepczynski M., Szczubialka K., New polymeric photosensitizers, Internal Union of Pure and Applied Chemistry 73, 2001, 491–495

[Nym04] Nyman E. S., Hynninen P. H., Research Advances in the use of tetrapyrolic photosensitizers for photodynamic therapy, Journal of Photochemistry and Photobiology B: Biology 73, 2004, 1-28

[Oel94] Oelckers S., Hanke T., Moser J., Röder B., Time-resolved detection of singlet oxygen luminescence in red cell ghosts generated by photosensitizers via excitation in the far red, SPIE 2325, 1994, 116-120

[Oel97] Oelckers S., Sczepan M., Hanke T., Röder B., Time-resolved detection of singlet oxygen luminescence in red ghost cell suspensions, Journal of Photochemistry and Photobiology B: Biology 39, 1997, 219-223

[Oel99] Oelckers S., Ziegler T., Michler I., Röder B., Time-resolved detection of singlet oxygen luminescence in red-cell ghost suspensions: concerning a signal component that can be attributed to $^1O_2$ luminescence from the inside of a native membrane, Journal of Photochemistry and Photobiology B 53, 1999, 121–127

[Ogu05] Ogura S., Yazaki K., Yamaguchi K., Kamachi T., Okura I., Localization of poly-l-lysine—photosensitizer conjugate in nucleus, Journal of Controlled Release 103, 2005, 1-6

[Oma04] Omari S., Ermilov E. A., Helmreich M., Jux N., Hirsch A., Röder B., Transient absorption spectroscopy of a monofullerene C_{60}-bis-(pyropheophorbide a) molecular system in polar and nonpolar environments, Applied Physics B 79, 2004, 617-622

[Osu96] Osuka A., Wada Y., Shinoda S., Covalently Linked Pyropheophorbide Dimers As Models of the Special Pair in the Photosynthetic Reaction Center, Tetrahedron 52, 1996, 4311-4326

[Par60] Parker C. A., Rees W. T., Correction of fluorescence spectra and measurement of fluorescence quantum efficiency, Analyst 85, 1960, 587-600

[Pat94] Patterson M. S., Wilson B. C., Theoretical study of the influence of sensitizer photobleaching on depth of necrosis in photodynamic therapy, Proceedings of SPIE 2133, 1994, 208-219

[Patent00] Röder B., Hackbarth S., Wöhlecke G., Dendrimer-photsensitizer complexes for medical application, US-Patent, NDN 172-0037-2622-7

[Pau02] Paul A., Mölich A., Oelckers S., Seifert M., Röder B., Alkyl-substituted magnesium-phthalocyanine: III, Phototoxicity after excitation of higher electronic states in cells in vitro. Journal of Porphyrins and Phthalocyanines 6, 2002, 340-346.

[Pau03] Paul A.,Hackbarth S., Mölich A., Luban C., Oelckers S., Böhm F., Röder B., Comparative Study on the Photosensitization of Jurkat Cells in vitro by Pheophorbide-a and a Pheophorbide-a Diaminobutane poly-propylene-imine Dendrimer Complex., Laser phys. 13, 2003, 22-29.

[Pau04] Paul A., Hackbarth S., Vogt R. D., Röder B., Burnison B. K., Steinberg C. E. W., Photogeneration of singlet oxygen by humic substances: comparison of humic substances of aquatic and terrestrial origin, Photochemical and Photobiological Sciences 3, 2004, 273

[Pet06] Pettersson K., Wiberg J., Ljungdahl T., Mårtensson J., Albinsson B. J., Interplay between Barrier Width and Height in Electron Tunneling: Photoinduced Electron Transfer in Porphyrin-Based Donor-Bridge-Acceptor Systems, Journal of Physical Chemistry A 110, 2006, 319-326

[Pol02] Polo, L., Valduga, G., Jori, G., Reddi, E. Low-density lipoprotein receptors in the uptake of tumour photosensitizers by human and rat transformed fibroblasts. The International Journal of Biochemistry & Cell Biology 34, 2002, 10-23.

[Ran05a] Rancan F., Helmreich M., Mölich A., Jux N., Hirsch A., Röder B., Witt C., Böhm F., Fullerene-pyropheophorbide a complexes as sensitizer for photodynamic therapy: Uptake and photo-induced cytotoxicity on Jurkat cells., Journal of Photochemistry and Photobiology B: Biology 80, 2005, 1-8

[Ran05b] Rancan F., Wiehe A., Nöbel M., Senge M., Omari S. Al., Böhm F., John M., Röder B. ,Influence of substitutions on asymmetric dihydroxychlorins with regard to intracellular uptake, subcellular localization and photosensitization of Jurkat cells, Journal of Photochemistry and Photobiology B: Biology 78, 2005, 17–28

[Ran07a] Rancan F., Helmreich M., Mölich A., Jux N., Hirsch A., Röder B., Böhm F., Intracellular uptake and phototoxicity of pyropheophorbide-a-fullerene hexa-adducts, Journal of Photochemistry and Photobiology, 2007, submitted

[Ran07b] Rancan F., Helmreich M., Mölich A., Ermilov E. A., Jux N., Röder B., Hirsch A., Böhm F., Synthesis and in Vitro Testing of a Pyropheophorbide-a-Fullerene Hexakis Adduct Immunoconjugate for Photodynamic Therapy, Bioconjugate Chemistry, available online

[Ran78] Rånby, B., Rabek J.F., Singlet Oxygen Reactions with Organic Compounds and Polymers, Wiley, N.Y., 1978

[Rav04] Ravanat J. L., Sauvaigo S., Caillat S., Martinez G. R., Medeiros M. H. G.., Mascio P. D., Favier A., Cadet J., Singlet oxygen-mediated damage to cellular DNA determined by the comet assay associated with DNA repair enzymes, Journal of Biological Chemistry 385, 2004, 17-20

[Reg07a] Regehly M., Greish K., Rancan F., Maeda H., Böhm F., Röder B., Water-soluble polymer conjugates of ZnPP for photodynamic tumor therapy, Bioconjugate Chemistry 18, 2007, 494-499

[Reg07b] Regehly M., Ermilov E. A., Helmreich M., Hirsch A., Jux N., Röder B., Photoinduced Energy and Electron Transfer Processes in Hexapyropheophorbide a- Fullerene [C60] Molecular Systems, Journal of Physical Chemistry B 111, 2007, 998-1006

[Reh69] Rehm D., Weller A., Kinetik und Mechanismus der Elektronenübertragung bei der Fluoreszenzlöschung in Acetonitril, Berichte der Bunsengesellschaft für Physikalische Chemie 73, 1969, 834-839

[Reh70] Rehm D., Weller A., Kinetics of fluorescence quenching by electron and H-atom transfer, Israel Journal of Chemistry 8, 1970, 259-271

[Rin75] Ringsdorf, H., Structure and properties of pharmacologically active polymers. Journal of Polymer Science / Polymer Symposia, 51, 1975, 135-153

[Rob06] Roby A., Erdogan S., Torchilin V. P., Solubilization of poorly soluble PDT agent, meso-tetraphenylporphin, in plain or immunotargeted PEG-PE micelles results in dramatically improved cancer cell killing in vitro, European Journal of Pharmaceutics and Biopharmaceutics 62, 2006, 235-240

[Rob62] Robinson G. W., Frosch R. P., Theory of Electronic Energy Relaxation in the solid phase, Journal of Physical Chemistry 37, 1962, 1962-1973

[Röd00a] Röder, B., Photodynamic therapy, Encyclopedia of Analytical Chemistry., MeyersRA (ed), Wiley&Sons Ltd. Chichester, 2000, 302-322

[Röd00b] Röder B., Hanke Th., Oelckers St., Hackbarth St., Symietz Ch., Photophysical properties of pheophorbide a in solution and in model membrane systems., Journal of Porphyrins and Phthalocyanines 4, 2000, 37-44.

[Röd04] Röder B., Tetrapyrroles. Photophysical properties and light induced transfer processes, Humboldt-Spektrum 11, 2004, 78-81

[Röd06a] Röder B., Ermilov E., Regehly M., Helmreich M., Jux N., Rancan F., Böhm F., Pheophorbide a - fullerene C60 hexadduct molecular systems as part of modular carrier systems for PDT, Journal of Porphyrins and Phthalocyanines 10, 2006, 499

[Röd06b] Röder B., Ermilov E.A., Hackbarth S., Helmreich M., Jux N., Trap formation and energy transfer in pheophorbide a-DAB-dendrimers and pyropheophorbide a-fullerene C60 hexaadduct molecular systems. SPIE 6192, 2006, 495-507

[Rod81] Rodgers M., Picosecond Fluorescence Studies of Xanthene Dyes in Anonic Micelles in Water and Reverse Micelles in Heptane, Journal of Physical Chemistry, 85, 1981, 3372-3374

[Röd90a] Röder, B., Tetrapyrroles: A Chemical class of Potent Photosensitizers for Photodynamic Therapy, Lasers in Medical Science 5, 1990, 99-106

[Röd90b] Röder B., Näther D., Lewald T., Braune M., Freyer W., Nowak Ch., Photophysical properties and photodynamic activity in vivo of some tetrapyrroles, Biophysical Chemistry 35, 1990, 303-312.

[Röd98] Röder B., chapter 2: Phorbides - Individual Data, Quantitative Data of 2nd and 3rd generation photosensitizers for PDT, ed.: J.G. Moser, 35 - 42, Gordon and Breach Science Publ. LTD, 1998

[Röd99] Röder B., Einführung in die molekulare Photobiophysik, B. G. Teubner Stuttgart, 1999

[Roy03] Roy I., Ohulchansky T. Y., Pudavar H. E., Bergey E. J., Oseroff A. R. , Morgan J., Dougherty T. J., Prasad P. N., Ceramic-based nanoparticles entrapping water-insoluble photosensitizing anticancer drugs: A novel drug-carrier system for photodynamic therapy, Journal of the American Chemical Society 125, 2003, 7860-7865

[Rüc97] Rückmann I., Zeug A., Herter R., Röder B., On the Influence of Higher Excited States on the ISC Quantum Yield of Octa-a-alkyloxy–substituted Zn-Phthalocyanine Molecules Studied by Nonlinear Absorption, Journal of Photochemistry and Photobiology 66, 1997, 576-584

[Rue99] Ruebner A., Yang Z., Leung D., Breslow R., A cyclodextrin dimer with a photocleavable linker as a possible carrier for the photosensitizer in photodynamic tumor therapy, Proceedings of the National Academy of Sciences 96, 1999, 14692–14693

[Sah02] Sahoo S. K., Sawa T., Fang J., Tanaka S., Miyamoto Y., Akaike T., Maeda H., Pegylated Zinc Protoporphyrin: A Water-Soluble Heme Oxygenase Inhibitor with Tumor-Targeting Capacity. Bioconjugate Chemistry, 13, 2002, 1031-1038

[Sai04] Saik V. O., Goun A. A., Nanda J., Shirota K., Tavernier H. L., Fayer M. D., Photoinduced Intermolecular Electron Transfer in Liquid Solutions, Journal of Physical Chemistry A 108, 2004, 6696-6703

[Sak97] Sakata Y., Imahori H., Tsue H., Higashida S., Akiyama T., Yoshizawa E., Aoki M., Yamada K., Hagiwara K., Taniguchi S., Okada T., Control of electron transfer and its utilization, Pure & Applied Chemistry 69, 1997, 1951-1956

[Sav03] Savellano M.D, Tayyaba H., Targeting cells that overexpress the epidermal growth factor receptor with polyethylene glycolated BPD verteporfin photosensitizer immunoconjugates, Photochemistry and Photobiology 77, 2003, 431–439

[Sav05] Savellano M. D., Hasan T., Photochemical Targeting of Epidermal Growth Factor Receptor: A Mechanistic Study, Clinical Cancer Research 11, 2005, 1658–1668

[Sch03] Schweitzer C., Schmidt R., Physical Mechanisms of Generation and Deactivation of Singlet Oxygen, Chemistry Reviews 103, 2003, 1685-1757

[Sch05] Schmidt-Erfurth U., Michels S., Indorf L., Eggers R., Birngruber R., Mechanism of Photodynamic Occlusion Using Liposomal Zn(II)-Phtalocyanine, Current Eye Research 30, 2005, 601 – 612

[Sch92] Schmidt R., Afshari E., Collisional Deactivation of $O_2(^1\Delta_g)$ by Solvent Molecules. Comparative Experiments with $^{16}O_2$ and $^{18}O_2$, Berichte der Bunsen-Gesellschaft für Physikalische Chemie 96, 1992, 788-794

[Sch95] Schneckenburger, H., Sailer R., Gschwend M. H., Kunzi-Rapp K., Rueck A. C., Strauss W. S. L., Comparative in vitro and in vivo measurements of hydrophilic and hydrophobic porphyrins, Proceedings of SPIE 2325, 1995, 106-115.

[Sie67] Siebrand W., Radiationless transitions in polyatomic molecules: I. Calculation of Frank-Condon-factors, Journal of Chemical Physics 46, 1967, 440-447

[Sim57] Simpson W. T., Peterson D. L., Coupling Strength for Resonance Force Transfer of Electronic Energy in Van der Waals Solids, Journal of Chemical Physics 26, 1957, 588-593

[Sko05] Skovsen E., Snyder J. W., Lambert J. D. C., Ogilby P. R., Lifetime and Diffusion of Singlet Oxygen in a Cell, Journal of Physical Chemistry B. 109, 2005, 8570-8573

[Smi05] Smith D. K., Hirst A. R., Love C. S., Hardy J. G.., Brignell S. V., Huang B., Self-assembly using dendritic building blocks—towards controllable nanomaterials, Progress in Polymer Science 30, 2005, 220–293

[Sny04] Snyder J. W., Zebger I., Gao, Z., Poulsen L., Frederiksen P. K., Skovsen E., McIlroy S. P., Klinger M., Andersen L. K., Ogilby P. R., Singlet Oxygen Microscope: From Phase-Separated Polymers to Single Biological Cells, Accounts of Chemical Research 37, 2004, 894-901

[Sny05] Snyder J. W., Skovsen E., Lambert J. D. C., Ogilby P. R., Subcellular, Time-Resolved Studies of Singlet Oxygen in Single Cells, Journal of the American Chemical Society 127, 2005,14558-14559

[Sol05] Solovyov K. N., Borisevich E. A., Intramolecular heavy-atom effect in the photophysics of organic molecules., Physics-Uspekhi, 48, 2005, 231-253

[Sou02] D'Souza F., Deviprasad G. R., Zandler M. E., Hoang V. T., Klykov A., VanStipdonk M., Perera A., El-Khouly M. E., Fujitsuka M., Ito O., Spectroscopic, Electrochemical, and Photochemical Studies of Self-Assembled via Axial Coordination Zinc Porphyrin-Fulleropyrrolidine Dyads, Journal of Physical Chemistry A 106, 2002, 3243-3252

[Spe96] Speiser S., Photophysics and Mechanisms of Intramolecular Electronic Energy Transfer in Bichromophoric Systems: Solution and Supersonic Jet Studies, Chemical Reviews 96, 1996, 1953-1976

[Spi98] Spiller W., Kliesch H., Wöhrle D., Hackbarth St., Röder B., Singlet oxygen quantum yields of different photosensitizers in polar solvents and micellar solutions, Journal of Porphyrins and Phthalocyanines 2, 1998, 145-158.

[Sri95] Srivastava A., Doraiswamy S., Rotational diffusion of Rose Bengal, Journal of Chemical Physics, 103, 1995, 6197

[Ste06] Stefflova K., Chen J., Marotta D., Li H., Zheng G.,Photodynamic Therapy Agent with a Built-In Apoptosis Sensor for Evaluating Its Own Therapeutic Outcome in Situ, Journal of Medical Chemistry 49, 2006, 3850-3856

[Sti93] Stiel H., Marlow I., Röder B., Photophysical properties of the photosensitizer pheophorbide a studied at high photon flux densities, Journal of Photochemistry and Photobiology B 17, 1993,181-186

[Sun00] Sun Y.-P., Guduru R., Lawson G. E., Mullins J. E., Guo Z., Quinlan J., Bunker C. E., Gord J. R., Photophysical and Electron-Transfer Properties of Mono- and Multiple-Functionalized Fullerene Derivatives, Journal of Physical Chemistry B 104, 2000, 4625-4632

[Tar03] Taroni P., Pifferi A., Torricelli A., Comelli D., Cubeddu R., In vivo absorption and scattering spectroscopy of biological tissues, Photochemistry Photochemical and Photobiological Sciences 2, 2003, 124–129

[Tav00] Tavernier H. L., Kalashnikov M. M., Fayer M. D., Photoinduced intermolecular electron transfer in complex liquids: Experiment and theory, Journal of Chemical Physics 113, 2000, 10191-10201

[Taw06] Tawakol A., Castano A. P. , Anatelli F., Bashian G. , Stern J., Zahra T. , Gad F., Chirico S., Ahmadi A., Fischman A. J., Muller J. E., Hamblin M. R., Photosensitizer delivery to vulnerable atherosclerotic plaque: comparison of macrophage-targeted conjugate versus free chlorin(e6). Journal of Biomedical Optics 11, 2006, 021008.

[Tog04] Togashi D. M., Costa S. M. B., Sobral A. J. F. N., Gonsalves A. M. d'A. R., Self-Aggregation of Lipophilic Porphyrins in Reverse Micelles of Aerosol OT, Journal of Physical Chemistry B, 108, 2004, 11344-11356

[Van00] van Veen R.L.P., Sterenborg H.J.C.M., Pifferi A., Torricelli A., Cubeddu R., Determination of VIS- NIR absorption coefficients of mammalian fat, with time-and spatially resolved diffuse reflectance and transmission spectroscopy, Proceedings of Biomedical Topical Meetings, 2000

[Ven98] Venturoli G., Drepper F., Williams J. C., Allen J. P., Lin X., Mathis P., Effects of Temperature and $\Delta G°$ on Electron Transfer from Cytochrome c_2 to the Photosynthetic Reaction Center of the Purple Bacterium *Rhodobacter sphaeroides*, Biophysical Journal 74, 1998, 3226

[Vro99] Vrouenraets M. B., Visser G. W. M., Stewart F. A., Stigter M., Oppelaar H., Postmus P. E., Snow G. B., van Dongen G. A. M. S., Development of meta-Tetrahydroxyphenylchlorin-Monoclonal Antibody Conjugates for Photoimmunotherapy, Cancer Research 59, 1999, 1505-1513

[Wan04] Wang S., Gao R., Zhou F., Selke M., Nanomaterials and singlet oxygen photosensitizers: potential applications in photodynamic therapy, Journal of Materials Chemistry 14, 2004, 487–493

[Wei04] Weiss E. A., Sinks L. E., Lukas A. S., Chernick E. T., Ratner M. A., Wasielewski M. R., Influence of Energetics and Electronic Coupling on Through-Bond and Through-Space Electron Transfer within U-Shaped Donor-Bridge-Acceptor Arrays, Journal of Physical Chemistry B 108, 2004, 10309-10316

[Wie01a] Wiehe A., Simonenko E. J., Senge M.O., Röder B., Hydrophilicity vs. hydrophobicity - varying the amphiphilic structure of porphyrins related to the photosensitizer m-THPC., Journal of Porphyrins and Phthalocyanines 5, 2001, 758-761.

[Wie01b] Wiehe A., Stollberg H., Runge S., Paul A., Senge M. O., Röder B., PDT-Related Photophysical Properties of Conformationally Distorted Palladium(II) Porphyrins., Journal of Porphyrins and Phthalocyanines 5, 2001, 853-860

[Wie01c] Wiehe A., Senge M. O., Schäfer A., Speck M., Tannert S., Kurreck H., Röder B., Electron Donor-Acceptor Compounds. Exploiting the Triptycene Geometry for the Synthesis of Porphyrin-Quinone Diads, Triads, and a Tetrad., Tetrahedron 57, 2001, 10089-10110

[Wig26] Wigner, E., Über nicht kombinierende Terme in der neueren Quantentheorie, Erster Teil, Zeitschrift der Physik 40, 1926, 492

[Wig27a] Wigner, E., Über nicht kombinierende Terme in der neueren Quantentheorie, Zweiter Teil, Zeitschrift der Physik 40, 1927, 883

[Wig27b] Wigner, E., Einige Folgerungen aus der Schrödingerschen Theorie für die Termstrukturen, Zeitschrift der Physik 43, 1927, 624

[Wil85] Wilson B. C., Jeeves W. P., Lowe D. M., In vivo and post mortem measurements of the attenuation spectra of light in mammalian tissue., Photochemistry and Photobiology 42, 1985, 153-162

[Wöh06] Wöhrle D., Makarov S., Röder B., Litwinski Ch., Ermilov E., Suvorova O., Novel NIR-absorbing annulated multinuclear phthalocyanines, Journal of Porphyrins and Phthalocyanines 10, 2006, 421

[Woo92] Woodburn K., Stylli S., Hill J. S., Kaye A. H., Reiss J. A., Phillips D. R., Evaluation of tumour and tissue distribution of porphyrins for use in photodynamic therapy. British Journal of Cancer 65, 1992, 321-328.

[Yok05] Yokoyama M., Drug targeting with nano-sized carrier systems, Journal of Artificial Organs 8, 2005, 77–84

[Zeb03] Zebger I., Poulsen L., Gao Z., Andersen L. K., Ogilby P. R., Singlet oxygen images of heterogeneous samples: examining the effect of singlet oxygen diffusion across the interfacial boundary in phase separated liquids and polymers. Langmuir 19, 2003, 8927–8933.

[Zeb04] Zebger I., Snyder J. W., Andersen L. K., Poulsen L., Gao Z., Lambert J. D. C., Kristiansen U., Ogilby P. R., Direct Optical Detection of Singlet Oxygen from a Single Cell, Photochemistry and Photobiology 79, 2004, 319–322

[Zeu01] Zeug A., Rückmann I., Röder B., Picosecond transient dichroism and birefringence spectroscopy on pheophorbide-a molecules in solution, Journal of Optics B 3, 2001, S251-S258

[Zeu02a] Zeug A., Zimmermann J., Röder B., Lagorio MG., San Román E., Microcrystalline cellulose as a carrier for hydrophobic photosensitizers in water., Photochemical & Photobiological Sciences 1, 2002, 198-203.

[Zeu02b] Zeug A., Beiträge zur Weiterentwicklung der Transienten Absorptionsspektroskopie zur experimentellen Untersuchung ausgewählter Tetrapyrrole, Dissertation, 2002

[Zha03a] Zhang G.-D., Harada A., Nishiyama N., Jiang D.-L., Koyamad H., Aidac T., Kataoka K., Polyion complex micelles entrapping cationic dendrimer porphyrin: effective photosensitizer for photodynamic therapy of cancer, Journal of Controlled Release 93, 2003, 141– 150

[Zha03b] Zhang M., Zhang Z., Blessington D., Li H., Busch T. M., Madrak V., Miles J., Chance B., Glickson J. D., Zheng G., Pyropheophorbide 2-Deoxyglucosamide: A New Photosensitizer Targeting Glucose Transporters, Journal of Bioconjugate Chemistry 14, 2003, 709-714

11. Publications

Regehly M., Ermilov E. A., Helmreich M., Hirsch A., Jux N., Röder B.
Photoinduced Energy and Electron Transfer Processes in Hexapyropheophorbide a-Fullerene [C60] Molecular Systems
Journal of Physical Chemistry B 111, 2007, 998

Regehly M., Greish K., Rancan F., Maeda H., Böhm F., Röder B.
Water-soluble polymer conjugates of ZnPP for photodynamic tumor therapy
Bioconjugate Chemistry 18, 2007, 494

Röder B., Ermilov E., Regehly M., Helmreich M., Jux N., Rancan F., Böhm F.
Pheophorbide a - fullerene C60 hexadduct molecular systems as part of modular carrier systems for PDT
Journal of Porphyrins and Phthalocyanines 10, 2006, 499

Borgia S. L., Regehly M., Sivaramakrishnan R., Mehnert W., Korting H.C., Danker K., Röder B., Kramer K.D., Schäfer-Korting M.
Lipid Nanoparticles for skin penetration enhancement – correlation to drug localization within the particle matrix as determined by fluorescence and parelectric spectroscopy
Journal of Controlled Release 110, 2005, 151

Conference contributions:

Talk: **Polymeric carrier systems for photodynamic therapy**
International Symposium on Polymer Therapeutics (ISPT), Berlin, 02/2007

Poster: E. Ermilov, M. Regehly, M. Helmreich, N. Jux, A. Hirsch, B. Röder
Excitonic Interactions, Electron and Energy Transfer in Novel Fullerene-Dendron-Pyropheophorbide a Supramolecules

International Conference on Methods and Applications of Fluorescence, 07/05

Poster: M. Bauer, T. Salesch, M. Regehly, B. Röder
Auf Polymeren immobilisierte Photoaktive Nanopartikel
Dechema, Frankfurt, 07/2004

12. Acknowledgements

I would like to gratefully acknowledge the supervision of Prof. Dr. Beate Röder during this work and for being a good advisor and mentor of my PhD. In addition to her professional guidance I appreciate her keen sense for things beyond the academic life.

I thank Dr. Eugeny Ermilov, Dr. Steffen Hackbarth, Dipl.-Phys. Christian Litwinsky and Dipl.-Phys. Sebastian Tannert for their assistance with adjusting experimental set-ups, carrying out spectroscopic measurements and performing data analysis. In particular I would like to acknowledge the help of Dr. Hackbarth for numerous stimulating discussions and Dr. Ermilov for his support concerning publication of the obtained results. Dr. Fiorenza Rancan and Prof. Fritz Böhm are thanked for her help with all types of *in vitro* cell experiments and for enjoyable cooperative work. I am grateful also for the support from the laboratory assistants Anneliese Powitz and Gisela Wöhlicke.

I appreciate the collaboration with Dr. Norbert Jux and Dr. Matthias Helmreich from the University of Erlangen, Germany. They had synthesized the hexapyropheophorbide a-fullerene [C_{60}] molecules and reference compounds which I was allowed to investigate primarily during this work. Furthermore I am grateful to the group of Prof. Hiroshi Maeda from Kumamoto University, Japan. Dr. Khaled Greish and Arun K. Iyer supplied compounds like PEG-ZnPP and SMA-ZnPP that were interesting macromolecules to study. Members of both groups also participated in proof-reading of publication manuscripts. Many thanks also to Prof. Monika Schäfer-Korting and Prof. Klaus Kramer from Free University of Berlin, for the lively cooperation regarding the lipid nanoparticles. I appreciate the support of Dr. Ullrich Siggel concerning the investigation of the Oligothiophen bridged Bisporphyrins.

I am grateful to all my friends from DLR for being a second family during the many years we know each other. Thanks to Karsten, Addi, David, Dennis, Anko, Martin for enjoying holidays, evenings @103, relay marathons and many other activities. I particularly appreciate the support and advice from Prof. Dr. Ralf Reulke and Dr. Martin Scheele.
Finally, I am forever grateful to my parents, my sister and Maren for their understanding, endless patience and encouragement when it was most required.

13. Curriculum vitae

Mein Lebenslauf wird aus Datenschutzgründen in der elektronischen Version meiner Arbeit nicht mit veröffentlicht.